

Frequency Noise Control of Heterogeneous Si/III-V Lasers

Thesis by
Dongwan Kim

In Partial Fulfillment of the Requirements
for the degree of
Doctor of Philosophy

The Caltech logo, featuring the word "Caltech" in a bold, orange, sans-serif font, centered within a light yellow rectangular background.

California Institute of Technology
Pasadena, California

2018
(Defended October 17, 2017)

© 2018

Dongwan Kim

ORCID: 0000-0002-5661-2503

All rights reserved except where otherwise noted

ACKNOWLEDGEMENTS

First and foremost, I would like to thank my advisor, Prof. Amnon Yariv. He provided me the opportunity to encounter and gain expertise in the field of optics and photonics. His sincere passion towards many things, not just science deeply inspired me. I feel very thankful to have been able to interact with him during the most important years of my life, and I deeply appreciate his existence as a human being. I am sure that in every corner of my life, he will provide me inspiration.

I appreciate my thesis committee members, Prof. Oskar Painter, Andrei Faraon, and Keith Schwab. I feel privileged to have them on my committee. I also would like to show my gratitude to Prof. Bruno Crosignani.

Without a few individuals, I could never have gotten through the hard time of graduate student life successfully. In that sense, I must thank Mark Harfouche first. From the first day that I joined the group, Mark has been an invaluable person to me, both on and off campus. He has never hesitated to provide and share scientific knowledge and explanations, and has been a key person in various research projects in the group. I feel fortunate to have been able to meet and interact with him in my life, and can never sufficiently express how deeply I am indebted to him.

I also would like to thank Dr. Huolei Wang, who has been another key person in the project. He has not only endured my foul temper with his earnest mind, but also made a great contribution to the project. I will never forget his warm heart and sincere attitude towards people.

I also would like to express my thanks to Dr. Christos Santis, who has been my one and only friend, science mentor, and office mate. I hope that the friendship that we have developed over the years will last a lifetime.

I owe much acknowledgement to Dr. Naresh Satyan and Dr. George Rakuljic. They have not only brought funding to the project, they have also been invaluable scientific counselors.

In recent years, I enjoyed the company of Zhewei Zhang and Hetuo Chen. I believe that they both possess great scientific potential, and wish them the best of luck as scientists.

I have also received much help from the previous graduate students in the group. Scott Steger, Yasha Vilenchik, Jacob Sendowski, who are all exceptionally talented individuals in their own ways, taught me the skills and knowledge that I need to continue the projects. Also, I would like to thank Paula Popescu, with whom I worked together during my early years in the group. I enjoyed

interacting with Reginald Lee, Arseny Vasilyev, Sinan Zhao, Yu Xien Lim, and Marilena Dimotsantou during my time at Caltech.

I am thankful to the Kavli Nanoscience Institute staff members, Guy DeRose and Melissa Melendes. I would also like to express my gratitude to Connie Rodriguez, Christy Jenstad, and Mabel Chik for their support.

I also got much help from and had fun with people outside the group, including Myoung-Gyun Suh, Nick White, Byung-Kuk Yoo, Chun Sik Chae, Roarke Horstmeyer, Kyo Lee, Seung Hoon Lee, Ki Youl Yang, Dong Yoon Oh, Hansuek Lee, Kiwook Hwang, Hyoung Jun Ahn, Max Jones, Samantha Johnson, and Kevin Fiedler.

I would like to acknowledge the financial support from DARPA, ARO, and NSF for the projects described in this thesis.

Lastly, I would like to thank my parents, without whom I could never have been who I am today. Their unconditional love and support made me who I am today. Thank you.

ABSTRACT

Narrow-linewidth lasers have many applications including optical telecommunication, laser spectroscopy, atomic clocks, and light detection and ranging. Conventionally, narrow linewidth lasers have been realized in the form of fiber-based or solid-state lasers. These lasers are bulky and relatively expensive, limiting their usage as bench-top systems in laboratory environments. Historically, semiconductor lasers, also known as laser diodes, have served applications where size and cost are important factors, including fiber optic communications. The linewidth of the semiconductor lasers, however, has been limited to the MHz-level, due to high loss in laser cavities and small size.

Recently, reduction of the frequency fluctuations in the semiconductor lasers has been achieved, obtaining tens of kHz linewidth, using the heterogeneous Silicon/III-V platform with a new design strategy. In this design, the majority of the optical energy is stored in the low-loss high-Q silicon resonator away from the high-loss III-V active region, requiring the minimal gain from the active region to overcome the reduced modal loss.

This work explores the new design strategy further, and demonstrates theoretically and experimentally that the strategy eliminates the frequency fluctuations arising from the amplitude-phase coupling by placing a relaxation resonance frequency at frequencies of a few hundred MHz. Consequently, it becomes possible to obtain a semiconductor laser device possessing sub-kHz quantum-limited linewidths at frequencies of a few GHz (the frequencies of interest in optical telecommunication).

In addition to the frequency noise reduction, the strategy turns out to have the additional benefit of accomplishing a coherent and stable lasing operation, even under external reflections. Thus, the new design strategy has the potential to replace the costly, but currently indispensable external optical isolators, which have been traditionally used to maintain the consistent performance of semiconductor lasers in the presence of external reflection.

This work paves the way for the design of narrow-linewidth and stable semiconductor lasers that can function without the use of the bulky and costly external components, such as external cavities or optical isolators.

PUBLISHED CONTENT

[1] D. Kim, M. Harfouche, H. Wang, N. Satyan, G. Rakuljic, and A. Yariv, “Suppression of Linewidth Enhancement Factor in High-coherence Heterogeneously Integrated Silicon/III-V Lasers,” in Conference on Lasers and Electro-Optics, Optical Society of America, 2017, SW4C.8. doi: 10.1364/CLEO_SI.2017.SW4C.8. [Online]. Available:

https://www.osapublishing.org/abstract.cfm?uri=CLEO_SI-2017-SW4C.8

D.K. participated in the preparing the device sample, realizing the experimental setup, the data analysis, and in the writing of the manuscript.

[2] W. Huolei, D. Kim, M. Harfouche, N. Satyan, G. Rakuljic, and A. Yariv, “Narrow-Linewidth Oxide-Confined Heterogeneously Integrated Si/III-V Semiconductor Laser,” in Conference on Lasers and Electro-Optics, Optical Society of America, 2017, AM2B.2. doi: 10.1364/CLEO_AT.2017.AM2B.2. [Online]. Available:

https://www.osapublishing.org/abstract.cfm?uri=CLEO_AT-2017-AM2B.2

D.K. participated in the preparing the device sample, realizing the experimental setup, the data analysis, and in the writing of the manuscript.

[3] M. Harfouche, D. Kim, H. Wang, N. Satyan, G. Rakuljic, and A. Yariv, “Optical Feedback Sensitivity of Heterogeneously Integrated Silicon/III-V Lasers,” in Conference on Lasers and Electro-Optics, Optical Society of America, 2017, SW4C.7. doi: 10.1364/CLEO_SI.2017.SW4C.7. [Online]. Available:

https://www.osapublishing.org/abstract.cfm?uri=CLEO_SI-2017-SW4C.7

D.K. participated in the preparing the device sample, realizing the experimental setup, the data analysis, and in the writing of the manuscript.

[4] D. Kim, P. Popescu, M. Harfouche, J. Sendowski, M.-E. Dimotsantou, R. C. Flagan, and A. Yariv, “On-chip integrated differential optical microring refractive index sensing platform based on a laminar flow scheme,” *Opt. Lett.*, vol. 40, no. 17, pp. 4106–4109, Sep. 2015. doi: 10.1364/OL.40.004106. [Online]. Available:

<https://www.osapublishing.org/ol/abstract.cfm?uri=ol-40-17-4106>

D.K. prepared the device sample, conducting the experiments, analyzing the data, and writing the manuscript.

[5] D. Kim, P. Popescu, M. Harfouche, J. Sendowski, M.-E. Dimotsantou, R. C. Flagan, and A. Yariv, “On-chip Integrated Differential Optical Microring Biosensing Platform Based on a Dual Laminar Flow Scheme,” in Conference on Lasers and Electro-Optics, Optical Society of America, 2015, STu4K.7. doi: 10.1364/CLEO_SI.2015.STu4K.7. [Online]. Available:

https://www.osapublishing.org/abstract.cfm?uri=cleo_si-2015-STu4K.7

D.K. prepared the device sample, conducting the experiments, analyzing the data, and writing the manuscript.

TABLE OF CONTENTS

Acknowledgements	iii
Abstract	v
Published Content	vi
Table of contents	viii
List of illustrations	xi
List of Tables	xviii
<i>Chapter 1</i> Introduction	1
1.1 Narrow-linewidth semiconductor lasers for optical communication	1
1.2 Silicon photonics and heterogeneously integrated Si/III-V lasers	4
1.3 Thesis organization	5
<i>Chapter 2</i> Phase Noise in Heterogeneously Si/III-V Lasers	7
2.1 Laser physics	7
2.1.1 Carrier generation and recombination in active regions	7
2.1.2 Gain and loss in laser cavities	9
2.1.3 Spontaneous emission rate	12
2.1.4 Rate equations	13
2.2 Phase noise in semiconductor lasers	14
2.2.1 Phase drift due to spontaneous emission (Schawlow-Townes linewidth)	15
2.2.2 Linewidth enhancement factor	17
2.3 Phase noise reduction in heterogeneous Si/III-V lasers	18
2.3.1 Limitation of conventional semiconductor lasers	18
2.3.2 Phase noise reduction through modal engineering in heterogeneous lasers	19
2.4 Conclusions	21
<i>Chapter 3</i> Phase Noise Reduction in Heterogeneous Si/III-V Lasers	22
3.1 High-Q Silicon resonator for high-coherence heterogeneous lasers	22
3.1.1 Si resonator design	22
3.1.2 Si resonator passive measurement	27
3.2 Laser measurements	31
3.2.1 LIV and OSA measurement	31

3.2.2 Temperature dependence	32
3.3 Frequency noise measurements	35
3.3.1 Measurement setup	35
3.3.2 Experimental results.....	39
3.4 Discussions and conclusions.....	45
<i>Chapter 4</i> Dynamic Response.....	46
4.1 Differential analysis of the rate equations.....	46
4.2 The linewidth enhancement factor revisited	51
4.3 Suppression of the influence of the linewidth enhancement factor in QNCL	52
4.4 Intensity modulation response of the heterogeneous laser.....	54
4.4.1 Measurement setup	54
4.4.2 Experimental results.....	55
4.5 Frequency modulation response and linewidth enhancement factor	60
4.5.1 Measurement setup	60
4.5.2 Experimental results.....	62
4.6 Frequency noise above relaxation resonance frequency	65
4.7 Discussion and conclusions	70
<i>Chapter 5</i> Feedback Sensitivity	72
5.1 Feedback sensitivity of lasers	72
5.2 Feedback sensitivity of QNCL.....	76
5.3 MZI fringe visibility measurement	78
5.3.1 Measurement setup	78
5.3.2 Experimental results.....	81
5.4 Relative intensity noise (RIN) measurement	86
5.4.1 Measurement setup	86
5.4.2 Experimental results.....	86
5.5 Optical spectrum measurement.....	91
5.6 Discussions and conclusions	91
<i>Appendix A</i> Fabrication	93
A.1 Si resonator fabrication	93
A.2 III-V fabrication	99

A.2.1 Mesa formation using ion implantation	100
A.2.2 Mesa formation using oxide-confinement	102
<i>Appendix B</i> Biosensing.....	105
B.1 Biosensing using optical microresonators	105
B.2 Differential sensing based on a laminar flow scheme	106
B.3 Implementation of the platform.....	108
B.4 NaCl bulk sensing experiments	110
B.5 Conclusion.....	113
Bibliography.....	114

LIST OF ILLUSTRATIONS

Figure 1.1 Increasing the transmission capacity through wavelength-division-multiplexing. (Left) A 100 Gbps transmission requiring 100 GHz electronics is not feasible using the current electronics. With 100 GHz modulation, the carrier will experience larger fiber impairments. (Right) 100 GHz modulation can also be achieved by transmitting 10 channels with 10 GHz modulation each. 10 GHz electronics are readily available.....	1
Figure 1.2 IQ diagrams of the coherent modulation schemes.	2
Figure 1.3 Schematic of optical coherent communication.....	2
Figure 1.4 Diagram of heterogeneously integrated Si/III-V laser platform.....	4
Figure 2.1 (Left) The phasor model for the laser field phase. It shows the effect of a single spontaneous emission event on the laser field. The laser field rotating at a radian frequency of ω_0 has a length of N_p . The phase θ represents phase fluctuation caused by lasing frequency noise due to one spontaneous emission event. Spontaneous emission introduces direct phase noise (blue line) and amplitude noise (green line). Spontaneous emission creates photons whose phases are uncorrelated with that of the lasing field, making the angle ϕ a random variable uniformly distributed between $[0, 2\pi]$. (Right) The additional photons created by spontaneous emission induce carrier density fluctuations through stimulated emission. This coupling between photons and carriers is called a relaxation resonance and will be discussed in Section 4.2. The phase fluctuation caused by the refractive index change due to carrier density fluctuation is characterized by a parameter called a “linewidth enhancement factor” (α in Equation (2.33)).	16
Figure 2.2 Transverse mode profile $Elra2$ in conventional III-V laser and in a heterogeneous Si/III-V laser. (Left) In the conventional semiconductor laser made with III-V, the electric field of the laser mode is maximum at the active region (large $Elra2$), resulting in large spontaneous emission rate ($R_{sp}(l)$). Also, the large confinement in the lossy III-V material leads to high loss and small number of photons (N_p) in the laser. For these reasons, the linewidth of the III-V lasers is limited to the MHz range. (Right) In our heterogeneous lasers with two different Si/III-V materials, most of the light is confined in low-loss Si instead of lossy III-V. Due to low electric field at the active medium (small $Elra2$), we effectively reduce the spontaneous emission rate ($R_{sp}(l)$). Also, due to the small confinement factor in	

the III-V, a greater number of photons in the laser cavity (N_p) can be achieved. Reduction in gain due to reduced stimulated emission is balanced with reduction in loss, resulting in a constant threshold current density despite the drastic change of electric field distribution in the active region.....	19
Figure 2.3 SiO ₂ layer, which we call the “quantum noise control layer (QNCL)”, is introduced in between Si and III-V to further push the mode into the Si layer and reduce the confinement factor in the active region (QWs). (Top figures) The peak of the transverse mode profile stays further away from III-V (i.e., reduced $Elra2$), and the confinement factor in the QWs decreases with thicker QNCL thickness. (Bottom figures) COMSOL simulation showing the transverse mode profile with varying QNCL thickness. The reduction of the QW confinement factor with increasing QNCL thickness is evident.	20
Figure 3.1 Optical field intensity distribution of TE ₀ mode in the 2D Si/III-V laser simulation.	23
Figure 3.2 Grating unit cell model for 3D periodic grating simulation.	25
Figure 3.3 Schematic of the acceptor-type defect mode resonator and its optical band structure.	26
Figure 3.4 Schematic of donor-type defect mode resonator and its optical band structure.	26
Figure 3.5 Transmission spectrum of high-Q Si resonators (Top figure: donor-type mode, $N_{\text{defect}} = 299$, $N_{\text{mirror}} = 800$, $V = 200$ GHz, bottom figure: donor-type mode, $N_{\text{defect}} = 299$, $N_{\text{mirror}} = 2000$, $V = 200$ GHz).	28
Figure 3.6 Transmission spectrum of passive Si resonators with donor-type (in red) and acceptor-type (in blue) mode (Donor-mode: $N_{\text{defect}} = 499$, $N_{\text{mirror}} = 1200$, $V = 150$ GHz, acceptor-mode: $N_{\text{defect}} = 299$, $N_{\text{mirror}} = 2000$, $V = 150$ GHz).	29
Figure 3.7 Grating period vs. resonance wavelength of the Si resonator. Resonance wavelength can be coarsely tuned by varying the grating period. Grating period difference of 2.5 nm leads to resonance wavelength difference of ~15 nm. In all wavelength, Q-factor larger than 10^5 is achieved.	29
Figure 3.8 Grating period vs. resonance wavelength of the Si resonator. Resonance wavelength can be coarsely tuned by varying the grating period. Grating period difference of 2.5 ~nm leads to resonance wavelength difference of ~15 nm. In all wavelength, Q-factor larger than 10^5 is achieved.	30

Figure 3.9 Light-current and current-voltage characteristics of the fabricated lasers with 50 nm (device ID: hQsp6 ch01 slot2 bar6 dev5) and 90 nm (hQsp7 ch9 slot1 bar4 dev9) QNCL lasers.	32
Figure 3.10 Light-current and current-voltage characteristics of the 50 nm QNCL laser at different stage temperatures (device ID: hQsp6 ch01 slot2 bar06 dev05).	33
Figure 3.11 Optical emission spectrum of the 50 nm and 90 nm QNCL laser at 160 mA and 190 mA, respectively (device ID: hQsp6 ch01 slot2 bar6 dev5, hQsp7 ch09 slot1 bar04 dev09).	34
Figure 3.12 Optical emission spectrum of the 50 nm QNCL laser at different currents (device ID: hQsp6 ch01 slot2 bar06 dev05).	34
Figure 3.13 Optical emission spectrum of the three different 90 nm QNCL lasers. Each device has a different grating period.	35
Figure 3.14 Frequency noise measurement setup (DUT: device under test, PD: photodetector, MZI: Mach–Zehnder interferometer, RFSA: RF spectrum analyzer).....	36
Figure 3.15 Frequency noise power spectral density of the 50 nm QNCL laser (device ID: hQsp6 ch01 slot2 bar06 dev05).....	39
Figure 3.16 Frequency noise power spectral density of the 90 nm QNCL laser (device ID: hQsp7 ch9 slot1 bar4 dev9).....	41
Figure 3.17 Frequency noise PSD of the 50, 90 nm QNCL lasers. The commercial laser from Fitel is plotted for comparison.	42
Figure 3.18 Linewidth as a function injection current above the threshold current for the 50 nm (device ID: hQsp6 ch01 slot2 bar06 dev05) and 90 nm (device ID: hQsp7 ch9 slot1 bar4 dev9) QNCL lasers.	43
Figure 3.19 Linewidth at the maximum pumping current as a function of the QNCL thickness.	44
Figure 3.20 Linewidth at the maximum pumping current as a function of the lasing wavelength.	44
Figure 4.1 Laser small-signal model.....	47
Figure 4.2 Illustration of the intensity and frequency modulation depth of a semiconductor laser as a function of modulation frequency. For the FM depth, both temperature and carrier effects are included.	51

Figure 4.3 Expected frequency noise PSD of QNCL laser and conventional III-V laser. In our high-coherence Si/III-V lasers, due to reduction of the confinement factor in the active region, decrease in the relaxation resonance frequency compared to III-V only laser is expected. Due to suppression of the effect of the linewidth enhancement factor above the relaxation resonance frequency, we expect to see even further reduced noise frequency at the frequency range of a few GHz (i.e., optical telecommunication frequency).	53
Figure 4.4 Intensity modulation measurement setup.	54
Figure 4.5 IM response of the 50 nm QNCL laser at different bias currents (device ID: hQsp6 ch01 slot2 bar6 dev5).....	57
Figure 4.6 IM response of the 90 nm QNCL laser at different bias currents (device ID: hQsp7 ch09 slot1 bar4 dev9).....	58
Figure 4.7 IM response of the 50, 90, and 130 nm QNCL lasers at the similar bias current above each threshold.	58
Figure 4.8 Relaxation resonance frequencies of the 50 nm and 90 nm QNCL lasers as a function of $I - I_{th}$	59
Figure 4.9 Dependence of damping factor of the Si/III-V lasers on the relaxation resonance frequency.....	59
Figure 4.10 Frequency modulation measurement setup.	60
Figure 4.11 The IM and FM response of the 50 nm QNCL laser at the bias current of 130 mA ($I_{th} = 55$ mA, device ID: hQsp6 ch01 slot2 bar6 dev5).	64
Figure 4.12 Linewidth enhancement factor calculation for the 50 nm QNCL laser.....	64
Figure 4.13 The IM and FM response of the 90 nm QNCL laser at the bias current of 130 mA ($I_{th} = 65$ mA, device ID: hQsp7 ch09 slot1 bar4 dev9).	65
Figure 4.14 Linewidth enhancement factor calculation for the 90 nm QNCL laser.....	65
Figure 4.15 Frequency noise PSD for the 50 nm QNCL laser ($I_{th} = 55$ mA, $\lambda_0 = 1577$ nm, $\alpha = 5.8$, device ID: hQsp6 ch01 slot2 bar6 dev5). The extrapolated line for $\Delta\nu_{ST1} + \alpha 2H\omega 2$ is overlaid.....	67
Figure 4.16 Comparison of the relaxation resonance frequencies of the 50 nm QNCL laser at various bias currents, measured from two different measurements: the frequency noise and intensity modulation measurement.	67

- Figure 4.17 Frequency noise PSD of the 90 nm QNCL laser ($I_{th} = 65$ mA, $\lambda_0 = 1556$ nm, $\alpha = 3.0$, device ID: hQsp7 ch9 slot1 bar4 dev9). The extrapolated line for $\Delta v_{ST1} + \alpha^2 H\omega^2$ is overlaid. 69
- Figure 4.18 Comparison of the relaxation resonance frequencies of the 90 nm QNCL laser at various bias currents, measured from two different measurements: the frequency noise and intensity modulation measurement. 69
- Figure 5.1 (Left) A model of a compound cavity consisting of a laser diode and an external optical reflection. (Right) A diagram for the effective laser cavity mirror reflection. Δr represents a perturbation by the external optical feedback to the reflection coefficient of the laser cavity mirror. 73
- Figure 5.2 The round trip phase change $\Delta\phi_L$, as a function of the optical frequency ν at different levels of external optical feedback. ν_{th} represents the lasing frequency when there is no feedback ($\Delta r = 0$). The resonant phase condition of the compound cavity is satisfied when $\Delta\phi_L = 0$ 74
- Figure 5.3 Q-factor of the heterogeneous laser and the effective isolation, compared to the conventional III-V laser, as a function of the confinement factor in the III-V layer (Assumption: $Q_{Si} = 10^6$ and $Q_{III-V} = 10^4$). 78
- Figure 5.4 . The measurement setup used to quantify the MZI fringe visibility. The top path allows for the precise control of the magnitude of the external optical feedback. A variable attenuator is used to vary the amount of the external optical reflection going back into the laser. A booster optical amplifier (BOA) is used to enable the reflectivity to approach unity even in the presence of losses included in the fiber network. The bottom path measures the fringe visibility of the laser output as it passes through a MZI. Two isolators are used to prevent reflection from the measurement loop from going back into the laser. A piezo-actuator is controlled by a function generator, and is used to provide a small length variation to display interference fringes. 80
- Figure 5.5 The MZI fringe visibility of the commercial HR/AR coated DFB laser ($I = 30$ mA, $I_{th} = 5$ mA), as a function of time. (Left) The fringe visibility of 1 is maintained under weak feedback condition ($R_{ext} = -60$ dB). (Middle) As the feedback increases to $R_{ext} = -27$ dB, the fringe visibility starts to drop as the laser goes into the coherence collapse. (Bottom) The

fringe visibility becomes 0, i.e., in our case $\tau c \ll 1/\text{FSR}$, the laser completely loses coherence under strong feedback ($R_{\text{ext}} = -17$ dB).	81
Figure 5.6 The MZI fringe visibility measurement of the commercial DFB laser (QPhotonics, $I = 30$ mA, $I_{\text{th}} = 5$ mA) using two different setups (Figure 5.4), as a function of the external reflectivity R_{ext} . The two different setups, one using a gold fiber mirror and the other using an amplifier and a circulator, yield nearly the same result. The setup using an amplifier can create a maximum external reflectivity up to approximately 0 dB. The emitted power and the reflected power going into the laser are shown on the right axis of the plot.	83
Figure 5.7 The MZI fringe visibility measurement of the commercial DFB laser (QPhotonics, $I = 15$ mA, $I_{\text{th}} = 5$ mA) as a function of the external reflectivity R_{ext} . As a control experiment, the fringe visibility measurement is performed on the same laser after placing an isolator at the output of the laser.	84
Figure 5.8 MZI fringe visibility of the commercial laser (QPhotonics, $I = 15$ mA, $I_{\text{th}} = 5$ mA), 50 nm (device ID: hQsp7 ch8 slot1 bar7 dev10, $I = 200$ mA, $I_{\text{th}} = 100$ mA), and 90 nm (device ID: hQsp7 ch09 slot1 bar4 dev05, $I = 160$ mA, $I_{\text{th}} = 80$ mA) QNCL lasers.	85
Figure 5.9 The setup to measure the relative intensity noise (RIN) of the laser in the presence of the external reflection. The laser light is directly fed into a photodetector; the RF spectral density of the intensity noise is measured using an RF spectrum analyzer.	86
Figure 5.10 The RF RIN spectrum of the commercial AR/HR coated DFB laser (QPhotonics, $I = 20$ mA, $I_{\text{th}} = 5$ mA).	88
Figure 5.11 The RF RIN spectrum of the 50 nm QNCL Si/III-V laser (device ID: hQsp7 ch08 slot1 bar7 dev10, $I = 200$ mA, $I_{\text{th}} = 100$ mA).	89
Figure 5.12 The RF RIN spectrum of the 90 nm QNCL Si/III-V (device ID: hQsp7 ch09 slot1 bar4 dev05, $I = 150$ mA, $I_{\text{th}} = 80$ mA).	90
Figure 5.13 The optical spectrum under different levels of external feedback: (a) commercial laser (QPhotonics, $I = 40$ mA, $I_{\text{th}} = 5$ mA), (b) 50 nm QNCL laser (device ID: hQsp7 ch8 slot 1 bar7 dev10, $I = 180$ mA, $I_{\text{th}} = 100$ mA), and (c) 90 nm QNCL laser (device ID: hQsp7 ch09 slot1 bar4 dev05, $I = 200$ mA, $I_{\text{th}} = 80$ mA).	91
Figure A.1 A fabrication procedure for high-Q modegap grating Si resonator.	94

Figure A.2 Aspect ratio dependent etching causes etch lag in the grating region, when etched with the 400 nm e-beam resist. This etch lag in the high aspect ratio region can be avoided by using the thin 20 nm Cr hard mask.....	95
Figure A.5 SEM image of the fabricated grating in-plane Si resonator.	98
Figure A.6 An image showing the laser chip after bonding step and subsequent substrate removal step.	100
Figure A.9 SEM image of the fabricated laser using ion implantation.	102
Figure A.10 Schematic diagram of heterogeneous Si/III-V lasers where III-V mesa structure is made using oxide-confinement method.	102
Figure A.11 III-V mesa fabrication procedure using oxide-confinement.....	103
Figure A.12 SEM image of the fabricated laser using oxide-confinement method.....	104
Figure B.1 (a) Schematic view of the proposed platform. (b) Layout of the waveguide-resonator chip shown together with two-layer microfluidic structures. (c) Photograph of (left) the fabricated device where the Si_3N_4 waveguide-integrated microring resonator chip is bonded to the PDMS microfluidic device, (right) a dime shown for scale. (d) Photograph showing the laminar flow of the two different dye solutions flowing onto three pairs of resonators, with no disruption between two fluid layers.	106
Figure B.2 (a) Transmission spectrum of two high-Q microring resonators in water measured at 1064 nm (blue), the Lorentzian fits are shown in red. (b) sensing, reference, and differential frequency shift versus time from a 40 mM NaCl solution at constant stage temperature of 26°C. (c) differential shift versus time at various NaCl concentrations. (d) Differential shift versus NaCl concentrations at 26°C.....	109
Figure B.3 Sensing, reference, and differential frequency shifts versus time while continuously flowing DI water from two inlets to the sensing and reference resonator as the temperature of stage is adjusted from 22 to 30°C, 2 GHz of offset is applied to the reference shift to distinguish it from the sensing shift. (inset) monitored stage temperature.	110
Figure B.4 (a) Sensing, reference, and differential frequency shift versus time from a 40 mM NaCl solution at stage temperature from 22 to 30°C; (b) differential shift from all temperatures at each concentration.	112

LIST OF TABLES

Table 3.1. 2D Si waveguide design parameters.....	23
Table 3.2 Confinement factors in Si, III-V, and QW layer for various QNCL thickness.	24
Table 3.3 3D grating unit cell simulation parameters.....	25
Table 3.4 External Q-factor as a function of number of grating holes in the mirror section (For the reflectivity calculation, the laser cavity round time τ_L of 6 ps was used).	27
Table A.1 The structure of the III-V epi-wafer used in this thesis.	99

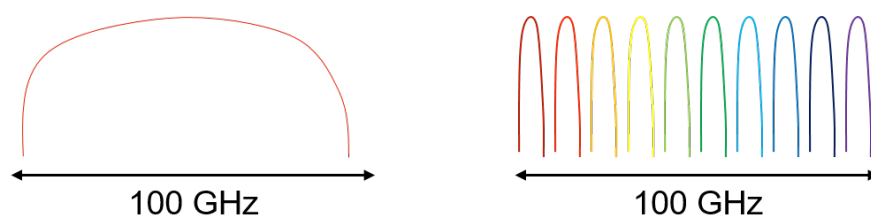
Chapter 1

INTRODUCTION

Since their invention in 1962, semiconductor lasers have become indispensable in modern technology serving as the primary light source powering modern high-data links, especially long-distance fiber-optic communication, thanks to their low cost and compactness, ease of electrical pumping, wide range of wavelengths of operation, and compatibility with Si-based electronics. Despite these advantages, semiconductor lasers suffer from low coherence properties. A narrow-linewidth and stable semiconductor laser would find many applications including optical telecommunication, laser spectroscopy, atomic clocks, and light detection and ranging.

1.1 Narrow-linewidth semiconductor lasers for optical communication

In conventional optical communication, a simple and effective modulation method has been used for decades. The modulation scheme is called on-off keying (OOK) or intensity-modulated/direct-detection (IMDD) systems. An IMDD system encodes a single bit (1 or 0) in each symbol. The binary digital signals are sent using a stream of light pulses, in which information is encoded in the light intensity and recovered using a photodetector.



- Need 1 laser and 100 GHz electronics - Need 10 laser and 10 GHz electronics

Figure 1.1 Increasing the transmission capacity through wavelength-division-multiplexing. (Left)

A 100 Gbps transmission requiring 100 GHz electronics is not feasible using the current electronics. With 100 GHz modulation, the carrier will experience larger fiber impairments. (Right) 100 GHz modulation can also be achieved by transmitting 10 channels with 10 GHz modulation each. 10 GHz electronics are readily available.

The transmission capacity in the OOK system can be expanded by either transmitting more modulation symbols per second or encoding more bits into a modulation symbol.

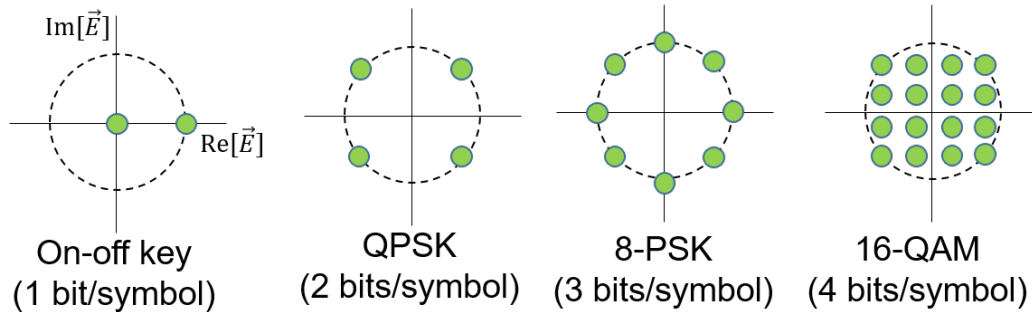


Figure 1.2 IQ diagrams of the coherent modulation schemes.

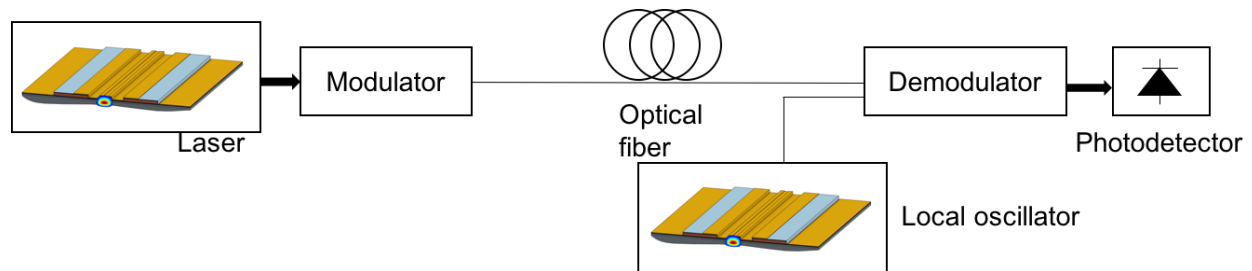


Figure 1.3 Schematic of optical coherent communication

With an increasing internet demand for data rates for 100 Gb/s and beyond from new and emerging services (e.g. 3D-TV [1], virtual-reality [2]), coherent phase communication schemes are emerging as promising key technologies to further increase the transmission capacity. These have been already realized in cutting-edge fiber-optic communication systems [3]. In these communication systems, the phase of the optical field is used to transmit information [4], making it possible to improve spectral efficiency by encoding more bits per symbol. For example, as shown in Figure 1.2, quadrature phase shift keying (QPSK) is a four-level modulation format, where the carrier phase is modulated to one of four possible phase states ($\pi/4$, $3\pi/4$, $5\pi/4$, $7\pi/4$). Using this format, we can send twice the amount of information with the same number of symbols as on-off keying.

Figure 1.3 illustrates that, for coherent communication, semiconductor lasers are used in conjunction with external modulators, which can be external to the laser chip or integrated on the same chip. Unlike direct modulation formats, these external modulators can be readily designed to have desirable properties such as chirp-free operation [5], and combined to independently modulate both the amplitude and phase of the laser (i.e. quadrature amplitude modulation (QAM)). This further improves spectral efficiency [6].

External modulations can also take advantage of a larger range of materials which operate at low voltages and currents making them desirable for low power applications [7]. A coherent receiver is then used to detect both the phase and amplitude of the transmitted wave, either by interfering the received pulse with a delayed version of itself, or with a local oscillator [8]. Throughout the operation, both the transmitting laser and the local oscillator typically operate in the continuous-wave (CW) regime, and their phase noise directly affects the signal to noise ratio of the received signal. For example, to operate at 40 Gb/s for 16 PSK and square 16 QAM, the laser linewidth in the range of 240 kHz and 120 kHz respectively is required [9]. In particular, the frequency noise near modulation sidebands (typically a few GHz to achieve high data rates) is especially crucial, since it will directly increase the bit error rate of the communication link.

Beyond this, a number of diverse applications that require the determination of high sensitivity or resolution, such as laser spectroscopy [10], optical frequency metrology [11, 12], atomic clocks [13, 14, 15], and light detection and ranging (LIDAR), require ultra-narrow linewidth lasers.

Conventionally, the narrow linewidth lasers have been realized in the form of fiber-based or solid-state lasers. These lasers are bulky and relatively expensive, limiting their usage as bench-top systems in the laboratory environments.

Historically, semiconductor lasers, also known as laser diodes, have served applications where size and cost are important factors, including fiber optic communications. In optical communication, phase-shifted distributed feedback (DFB) semiconductor lasers or DFB lasers with antireflection coated on one side of the cavity and high-reflection coated on the other side (AR/HR) have played a key role.

The linewidth of the semiconductor lasers has been limited to the MHz-level, due to high loss in laser cavities and small size. Linewidth narrowing of the semiconductor lasers has been achieved by extending the laser cavity using an external cavity or by locking the laser to an atomic transition.

The use of those external components, however, removes the benefits of small size and low cost of semiconductor lasers.

1.2 Silicon photonics and heterogeneously integrated Si/III-V lasers

Semiconductor lasers and semiconductor optical amplifiers (SOAs) have been available in various III/V material systems (e.g. InP and GaAs) and are the main candidate for future efficient and low-cost optoelectronic integrated platform.

Silicon (Si) photonics as an integration platform has recently become a focus in optoelectronics research. This is due to the fact that they can be fabricated with CMOS-based technology, enabling the integration of electronic devices on a silicon-on-insulator (SOI) wafer containing photonic devices. However, the indirect bandgap of Si has been an obstacle in the realization of electrically driven Si-based light sources. Although Si-based Raman lasers [16, 17] or Germanium(Ge)-on-Si lasers [18] have been demonstrated, electrically pumped all-Si lasers have yet to be realized.

An alternative to electrically pumped all-Si lasers is heterogeneous integration of III-V materials, such as InP, and SOI waveguides that enable light generation on Si (Figure 1.4). Heterogeneously integrated Si/III-V lasers have previously been demonstrated by several groups, but have historically failed to achieve a linewidth better than that of their all III-V counterparts [19, 20, 21].

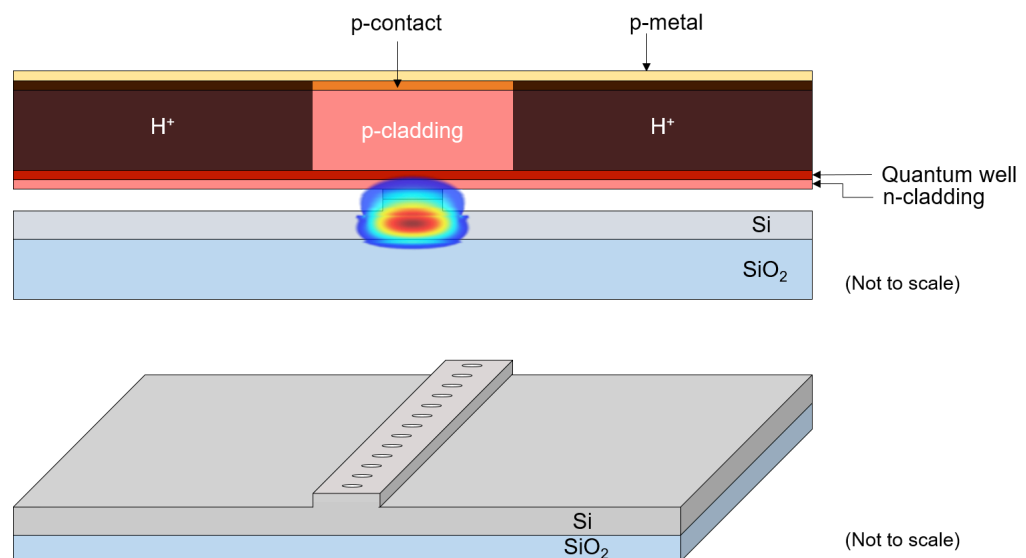


Figure 1.4 Diagram of heterogeneously integrated Si/III-V laser platform.

In this thesis, we show how to reduce the linewidth of the semiconductor lasers by orders of magnitude by making best use of the heterogeneous platform, which combines the lossy III-V active material and the low-loss passive Si material. Furthermore, we demonstrate that the strategy that we use for the reduction of the frequency fluctuation makes it possible for the laser to achieve even further reduction of the frequency noise, corresponding to a sub-kHz linewidth, at telecommunication relevant frequencies (i.e., a few GHz).

In fact, noise reduction is not the only benefit of our new design. So far, the consistent performance of semiconductor lasers, even in the presence of external reflection, has been achieved by the use of costly, but indispensable optical isolators. It turns out that our strategy to reduce the frequency noise has the additional benefit of enabling us to accomplish a coherent and stable operation, even under external reflections.

Our simple approach paves the path for the design of narrow-linewidth and stable semiconductor lasers that can function without the use of the bulky and costly components, such as external cavities or optical isolators.

1.3 Thesis organization

This thesis is organized as follows. Chapter 2 introduces the basic concepts of the laser physics and design, with emphasis on the effect of spontaneous emission on the frequency noise of a laser. We will also discuss the modal engineering in our Si/III-V laser as a way to achieve a narrow-linewidth semiconductor laser.

Chapter 3 presents the design and measurement of the grating-based defect-mode optical high-Q resonators. In the later part of Chapter 3, the experimental demonstrations of the reduction in the frequency noise of the lasers are presented.

Chapter 4 discusses the effect of the modal engineering on modulation response, especially in terms of the relaxation resonance frequency. The measurement of the intensity and frequency modulation response, and the linewidth enhancement factor of the lasers are described. Furthermore, we revisit the frequency noise measurement discussed in Chapter 3, and describe further reduction of the frequency noise at a few GHz range, revealing the intrinsic, quantum-limited Schawlow-Townes noise floor of the lasers.

In Chapter 5, we derive the theoretical background regarding the sensitivity of a laser against external reflections, and experimentally demonstrate orders of magnitude reduced sensitivity to external reflections.

Appendix A describes the procedures for the fabrication of the passive Si resonators as well as for the heterogeneous integration of Si and III-V.

Appendix B presents the work, carried out during my early years in the group, on refractive index sensing based on on-chip integrated differential optical microring platform, which leverages laminar flow conditions.

Chapter 2

PHASE NOISE IN HETEROGENEOUSLY SI/III-V LASERS

A laser emits light through a process called *stimulated emission*, which provides the gain to overcome the loss in the optical resonator. However, stimulated emission is inevitably accompanied by spontaneous emission, which introduces phase as well as amplitude noise into the laser mode and sets the fundamental limit to the laser coherence. In this chapter, we will describe the basic physics and derive the effect of spontaneous emission on the phase noise of a laser field. It enables us to obtain insights that can be exploited to reduce the quantum-limited phase noise in a semiconductor laser.

2.1 Laser physics

A laser oscillator consists of a gain medium to amplify light, and an optical cavity to provide optical feedback and optical mode selection. Careful design of both the gain medium and the optical cavity is necessary to achieve a high degree of coherence in a laser.

2.1.1 Carrier generation and recombination in active regions

Carrier generation

A semiconductor laser is basically a PIN diode. The active region of the semiconductor laser resides in the intrinsic layer. The electrons and holes (i.e., the carriers) are injected into the active region from the n- and p-region, respectively. The modal field in the optical resonator stimulates the injected electron-hole pairs to recombine in the process of amplifying the field coherently. However, not all of the injected carriers reach the active region, leading to an increase in the leakage current in the laser. The fraction of the pump current that generates carriers – which will recombine both radiatively and non-radiatively – in the active region is characterized by the injection efficiency η_i . The temporal generation rate of the total number of the injected electron-hole pairs N due to pump current I into the active region can be written as,

$$\frac{dN}{dt} = \eta_i \frac{I}{q}, \quad (2.1)$$

where q is an electron charge.

The overall injection efficiency is composed of both the structural current injection efficiency and the current injection efficiency in the active region [22].

The lateral current diffusion from the metal contact region, and the carrier loss due to poor interfaces in the cladding layers are the primary factors accounting for the structural injection efficiency. Our lasers, due to the heterogeneous nature of the structure with III-V material placed on top of Si, utilize the lateral-electrode structure, where both p- and n-metal are deposited in the same direction. Subsequently, they generate a large lateral current diffusion in the direction parallel to the active layer, thus increasing the total leakage current.

Carrier escape through thermionic emission over the cladding layers causes degradation of the current injection efficiency in the active region, and hence degrades the total injection efficiency.

Carrier recombination

The injected carriers recombine via a number of mechanisms:

- 1) The first mechanism is stimulated emission, where an incident photon stimulates the electron and hole to recombine, generating a copy of the photon in the same quantum state. This is the gain mechanism by which lasers amplify the light. This stimulated emission process allows the optical mode to build up coherently. The stimulated emission rate R_{st} represents the number of stimulated emission events per unit time.
- 2) The second mechanism is similar to 1) except that the rate is independent of the optical intensity in the cavity, hence the name “spontaneous emission”. The photons, generated by spontaneous emission, have no correlation with the coherent laser field created through stimulated emission, and thus modulate the phase of the laser mode. Spontaneous emission events cannot be completely removed, and this implies that it is impossible to achieve perfect coherence (i.e., perfect sinusoidal wave) in a laser.
- 3) The third mechanism is non-radiative recombination, which involves monomolecular recombination through surface defects in the active region of the laser. The non-radiative transition also can happen through Auger recombination, where energy from the electron-hole recombination is transferred to another electron or hole. In these transitions, instead of

generating photons, the energy is dissipated as heat.

The recombination through the spontaneous emission and the non-radiative transition, which does not require the existence of photons, is called a “natural decay process”, and is characterized by a carrier lifetime τ . Then, the temporal decay rate of the total number of the carriers N by a natural decay process can be written as

$$\frac{dN}{dt} = -\frac{N}{\tau}. \quad (2.2)$$

2.1.2 Gain and loss in laser cavities

Gain

For a laser to function as an optical oscillator, an optical cavity is needed to provide optical feedback. The electric field distribution of the standing wave in a cavity is usually referred to as the *mode*.

As discussed in the previous section, light is amplified through a stimulated emission process in the gain medium. The *modal gain*, g (s^{-1}) is defined as the fractional temporal growth in the number of photons in the mode N_p [23],

$$g = \frac{1}{N_p} \frac{dN_p}{dt} = \frac{R_{st}}{N_p}. \quad (2.3)$$

This relation follows from quantized field theory and is of key importance in all that follows. The modal gain g can be expressed using the induced transition rate per electron due to one photon A' and the total number of the injected electrons N ,

$$g = A'(N - N_{tr}), \quad (2.4)$$

where N_{tr} is the carrier number at transparency, at which point the stimulated emission rate is equal to the stimulated absorption.

Using the quantized electro-magnetic field and by applying the Fermi's Golden Rule to the dipole interaction between atomic systems and electro-magnetic radiation, the induced transition

rate into the laser mode (l) per electron due to one vacuum-field photon (i.e., the spontaneous emission transition rate of the electron into the laser mode) can be derived as [23, p. 155],

$$A' = W_{\text{sp}}^{(l)} = \frac{2\pi^2\mu^2\nu_0}{h\epsilon(\Delta\nu)_a} |\bar{E}_l(\vec{r}_a)|^2, \quad (2.5)$$

where μ is the dipole transition matrix element, $(\Delta\nu)_a$ is the frequency width of the lineshape function of the atom transition at the lasing frequency ν_0 .

The electric field distribution of the laser mode (\vec{E}_l) is normalized as,

$$\int_{-\infty}^{\infty} |\bar{E}_l(\vec{r})|^2 dV = 1. \quad (2.6)$$

With this normalization, the confinement factor of mode (l) in the region i can be written as,

$$\Gamma_i = \int_i |\bar{E}_l(\vec{r})|^2 dV. \quad (2.7)$$

Thus, $|\bar{E}_l(\vec{r}_a)|^2$ in Equation $A' = W_{\text{sp}}^{(l)} = \frac{2\pi^2\mu^2\nu_0}{h\epsilon(\Delta\nu)_a} |\bar{E}_l(\vec{r}_a)|^2$, (2.5) can be viewed as the normalized field due to a single photon in the cavity at the location \vec{r}_a of the emitting atoms, and is our “knob” to engineer the spontaneous emission rate into the laser mode.

The induced transition rate per electron, $W_{\text{st}}^{(l)}$, by N_p photons and the simulated emission rate due to the total number of the electrons, R_{st} , then can be written as,

$$W_{\text{st}}^{(l)} = N_p W_{\text{sp}}^{(l)}. \quad (2.8)$$

$$R_{\text{st}} = W_{\text{st}}^{(l)} (N - N_{\text{tr}}) = A' (N - N_{\text{tr}}) N_p. \quad (2.9)$$

Loss

An optical mode in a cavity decays through various mechanisms. Photons can be lost intrinsically in the cavity through absorption in materials, scattering by the roughness of the surface, and radiation into leaky modes. Also, a portion of the photons is lost by escaping the

cavity through a mirror, which is used as a useful output of the laser. The total amount of loss that a mode experiences is expressed using α (s^{-1}), loss coefficient per unit time.

A *quality-factor* (*Q-factor*) is also used to characterize the loss of the cavity and is defined as

$$Q = \omega \frac{E_{\text{stored}}}{P_{\text{loss}}} = \frac{\omega}{\alpha} = \omega \tau_p, \quad (2.10)$$

where τ_p is the *photon lifetime* in the cavity.

Then, the total loss experienced by a mode in a cavity composed of different materials can be expressed by a sum of losses in each material α_i weighted by a modal confinement factor in each material (Γ_i),

$$\alpha = \sum_i \Gamma_i \alpha_i. \quad (2.11)$$

For our lasers, we consider a heterogeneous platform composed of Si and InP, and the total loss of the platform can be expressed as,

$$\alpha_{\text{total}} = \Gamma_{\text{Si}} \alpha_{\text{Si}} + \Gamma_{\text{III-V}} \alpha_{\text{III-V}}. \quad (2.12)$$

The above equation also can be expressed in terms of Q-factor,

$$\frac{1}{Q_{\text{total}}} = \frac{\Gamma_{\text{Si}}}{Q_{\text{Si}}} + \frac{\Gamma_{\text{III-V}}}{Q_{\text{III-V}}} = \frac{1-\Gamma_{\text{III-V}}}{Q_{\text{Si}}} + \frac{\Gamma_{\text{III-V}}}{Q_{\text{III-V}}}. \quad (2.13)$$

Thus, we see that having large modal energy in low-loss, high-Q Si than in high-loss, low-Q III-V (i.e., large Γ_{Si} and small $\Gamma_{\text{III-V}}$) results in the large total Q-factor.

Threshold condition and threshold current

As we increase the modal gain by injecting more current, the carrier number reaches the transparency carrier number N_{tr} . A further increase in the carrier number is used to overcome the losses in the cavity. At the point where the modal gain equals the total loss in the cavity, the optical wave returns to the wave with the same amplitude and phase after each round trip in the cavity,

establishing a laser oscillation. Therefore, the laser threshold condition can be written with the threshold material gain g_{th} ,

$$g_{th} = \alpha_{total} = \frac{1}{\tau_p} = \frac{\omega}{Q}. \quad (2.14)$$

Above threshold, any carrier number rise slightly increases the stimulated emission rate, increasing the photon number through Equation $g = \frac{1}{N_p} \frac{dN_p}{dt} = \frac{R_{st}}{N_p}$. (2.3) and **Error! Reference source not found.**) Then, the increased photon number will in turn deplete the carriers through increased stimulated emission rate. This negative feedback clamps the gain above threshold at its threshold value g_{th} .

Since the gain above threshold is monotonically related to the carrier number, the carrier number is clamped at its threshold value N_{th} .

2.1.3 Spontaneous emission rate

The stimulated emission rate is dependent on the population inversion (the difference between the number of excited electrons and ground state electrons), whereas the spontaneous emission rate depends only on the total number of excited electrons.

At the steady-state above threshold, there is a balance between the number of photons generated by the stimulated emission and the photons lost in the cavity, and the balance yields,

$$(N_2 - N_1)W_{st}^{(l)} = \frac{N_p}{\tau_p}, \quad (2.15)$$

where $N_{1,2}$ is the number of electrons in the valance and conduction band.

Using Equation $g = \frac{1}{N_p} \frac{dN_p}{dt} = \frac{R_{st}}{N_p}$. (2.3) $3W_{st}^{(l)} = N_p W_{sp}^{(l)}$. (2.8), and $g_{th} = \alpha_{total} = \frac{1}{\tau_p} = \frac{\omega}{Q}$.

(2.14), it can be shown that the spontaneous emission rate into the lasing mode due to N_2 electrons in the conduction band ($R_{sp}^{(l)}$) and the total stimulated emission rate (R_{st}) is related by,

$$R_{sp}^{(l)} = N_2 W_{sp}^{(l)} = \frac{N_2}{N_2 - N_1} \frac{1}{\tau_p} = \frac{n_{sp}}{\tau_p} = n_{sp} g_{th} = \frac{n_{sp}}{N_p} R_{st} = \frac{n_{sp} \omega}{Q}, \quad (2.16)$$

where the population inversion factor n_{sp} is defined as $\frac{N_2}{N_2 - N_1}$ [24, p. 192].

2.1.4 Rate equations

Based on the discussion so far, the rate equation for the total number of carriers in the active region with the volume V_a can be written as,

$$\frac{dN}{dt} = \eta_i \frac{I}{q} - \frac{N}{\tau} - R_{st} \quad (2.17)$$

$$= \eta_i \frac{I}{q} - \frac{N}{\tau} - gN_p \quad (2.18)$$

$$= \eta_i \frac{I}{q} - \frac{N}{\tau} - A'(N - N_{tr})N_p \quad (2.19)$$

In the last equation, the 1st term describes the generation of the carriers via a current injection. The 2nd term accounts for the carrier recombination through both radiative and non-radiative process. The 3rd term is the loss of carriers through the stimulated emission.

In the steady-state at threshold, with threshold current I_{th} and threshold carrier number N_{th} , the number of the photons is negligible ($N_p = 0$). Thus, Equation $\frac{dN}{dt} = \eta_i \frac{I}{q} - \frac{N}{\tau} - R_{st}$ (2.17) can be used to find the threshold carrier number N_{th} ,

$$\eta_i \frac{I_{th}}{q} = \frac{N_{th}}{\tau}. \quad (2.20)$$

As discussed, above threshold, the carrier number in a laser is clamped at its threshold value N_{th} . Thus, we can obtain an above-threshold carrier number equation,

$$\frac{dN}{dt} = \eta_i \frac{I - I_{th}}{q} - g_{th}N_p. \quad (2.21)$$

$$= \eta_i \frac{I - I_{th}}{q} - A'(N_{th} - N_{tr})N_p. \quad (2.22)$$

Using Equation $\frac{dN}{dt} = \eta_i \frac{I - I_{th}}{q} - g_{th}N_p$ (2.21) and $g_{th} = \alpha_{total} = \frac{1}{\tau_p} = \frac{\omega}{Q}$ (2.14), the photon number in the lasing mode above threshold (N_{p0}) can be obtained as,

$$N_{p0} = \frac{\eta_i}{g_{th}} \frac{I - I_{th}}{q} = \eta_i \tau_p \frac{I - I_{th}}{q} = \eta_i \frac{Q}{\omega} \frac{I - I_{th}}{q}. \quad (2.23)$$

The rate equation for the total number of photons in the laser resonator can be written as,

$$\frac{dN_p}{dt} = R_{st} - \frac{N_p}{\tau_p} + R_{sp}^{(l)} \quad (2.24)$$

$$= gN_p - \frac{N_p}{\tau_p} + R_{sp}^{(l)} \quad (2.25)$$

$$= A'(N - N_{tr})N_p - \frac{N_p}{\tau_p} + R_{sp}^{(l)} \quad (2.26)$$

In the above equation, the 1st term accounts for the stimulated emission rate. The 2nd term describes the photon loss in the cavity both internally and through the laser mirrors. The 3rd term corresponds to the spontaneous emission rate.

2.2 Phase noise in semiconductor lasers

Based on the analysis described so far, we now investigate the phase noise in semiconductor lasers. The lasing mode can be expressed as,

$$E(t) = A(t)e^{j(\omega_0 t + \Delta\theta(t))}, \quad (2.27)$$

where $A(t)$ is the amplitude, $\omega_0/2\pi$ is the lasing frequency, and $\Delta\theta(t)$ is the random phase.

So far, we have assumed that the carrier and photon number in a laser remain constant in the steady-state operation. In fact, even in the steady state and in the absence of any kind of modulation, random carrier and photon recombination and generation occurs, causing fluctuations in the carrier and photon number (i.e., noise).

The frequency noise of a laser partly results from technical noise, with a dominant 1/f noise. This noise includes the noise from the pump source, and vibrations of cavity mirrors. As frequencies increase, the ever-decreasing 1/f noise is eventually dominated by the quantum white noise due to spontaneous emission into the laser mode. This type of the frequency noise is limited

by fundamental quantum processes. Thus, it is the noise that is ultimately responsible for the deviation of the lasing field from that of an ideal monochromatic field.

2.2.1 Phase drift due to spontaneous emission (Schawlow-Townes linewidth)

In 1982, Henry showed that the phase variance of a laser, accumulated over time τ , due to spontaneous emission into the laser mode, can be expressed using the total number of the spontaneous emission $R_{\text{sp}}^{(l)}\tau$, the photon number in the lasing mode N_p , and the linewidth enhancement factor α [25],

$$\langle \Delta\theta(\tau)^2 \rangle = \frac{R_{\text{sp}}^{(l)}}{2N_p} (1 + \alpha^2)\tau. \quad (2.28)$$

Assuming that the laser has only a white frequency noise, the phase variance $\langle \Delta\theta(\tau)^2 \rangle$ can be shown to be related to the laser linewidth $\Delta\nu_L$ as [26, p. 488],

$$\langle \Delta\theta(\tau)^2 \rangle = \Delta\omega_L \tau = 2\pi\Delta\nu_L \tau. \quad (2.29)$$

By combining the two above equations, a spontaneous emission-induced linewidth, known as ‘‘Schawlow-Townes linewidth’’, can be obtained as,

$$\Delta\nu_{\text{ST}} = \frac{R_{\text{sp}}^{(l)}}{4\pi N_p} (1 + \alpha^2). \quad (2.30)$$

As seen in the above equation, the Schawlow-Townes linewidth originates from two sources.

First, the spontaneous emission causes the instantaneous phase change to the lasing field (the blue line in Figure 2.1), and the term $\frac{R_{\text{sp}}^{(l)}}{4\pi N_p}$ describes this effect.

Besides, the spontaneous emission alters the intensity of the lasing field. To restore the steady-state photon number, the laser undergoes relaxation resonance oscillations, causing the carrier fluctuations. These carrier fluctuations result in not only a gain variation (to restore the steady-state photon number), but also a variation in the refractive index, and finally manifest as an

additional, delayed phase change [27, 28]. The linewidth enhancement factor α effectively characterizes the coupling between the gain variation and the refractive index variation.

Using Equation $A' = W_{sp}^{(l)} = \frac{2\pi^2\mu^2\nu_0}{h\epsilon(\Delta\nu)_\alpha} |\bar{E}_l(\bar{r}_a)|^2$, (2.5), $g_{th} = \alpha_{total} = \frac{1}{\tau_p} = \frac{\omega}{Q}$, (2.14), $N_{p0} = \frac{\eta_i}{g_{th}} \frac{I - I_{th}}{q} = \eta_i \tau_p \frac{I - I_{th}}{q} = \eta_i \frac{Q}{\omega} \frac{I - I_{th}}{q}$. (2.23) and $g_{th} = |\bar{E}_l(\bar{r}_a)|^2 V_a g' (N_{2t} - N_{tr})$ (g' : temporal differential material gain coefficient, V_a : volume of the active region), the quantum-limited

Schawlow-Townes linewidth in Equation $\Delta\nu_{ST} = \frac{R_{sp}^{(l)}}{4\pi N_p} (1 + \alpha^2)$. (2.30) can be expressed in terms of the Q-factor and the bias current,

$$\Delta\nu_{ST} = \frac{\pi^2\mu^2\omega_0^2}{2\pi\eta_i h\epsilon(\Delta\nu)_\alpha(I - I_{th})} \left(\frac{|\bar{E}_l(\bar{r}_a)|^2 N_{tr}}{Q} + \frac{\omega_0}{g'Q^2} \right) (1 + \alpha^2). \quad (2.31)$$

This expression demonstrates that the Schawlow-Townes linewidth has a $1/Q^2$ dependence and thus, the reduction of the modal loss in a laser (i.e., high-Q) is a key requirement for the reduction of a linewidth in the laser. The increase in the pump current also reduces the linewidth by increasing the number of photons N_p stored in the cavity. Thus, linewidths measured from different lasers should be compared at the same value of $(I - I_{th})$ to make a fair comparison.

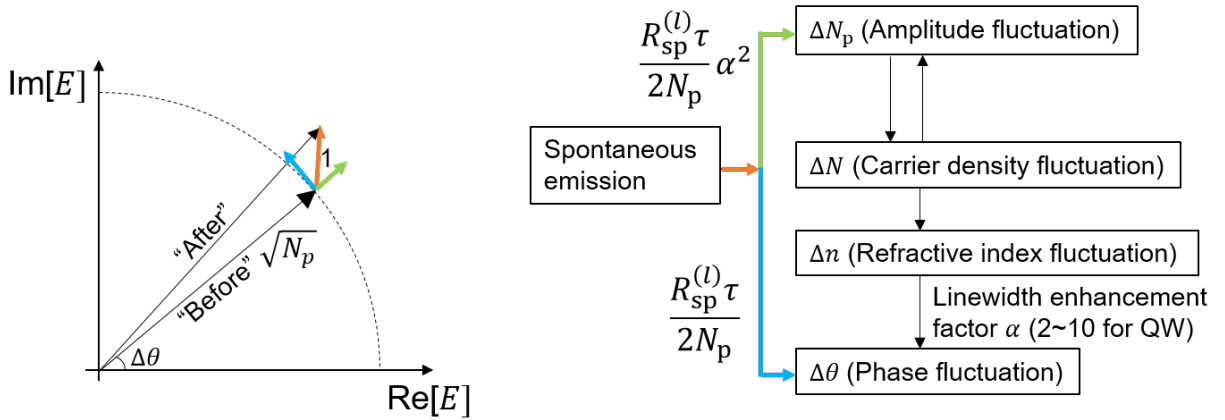


Figure 2.1 (Left) The phasor model for the laser field phase. It shows the effect of a single spontaneous emission event on the laser field. The laser field rotating at a radian frequency of ω_0 has a length of $\sqrt{N_p}$. The phase $\Delta\theta$ represents phase fluctuation caused by lasing frequency noise due to one spontaneous emission event. Spontaneous emission introduces direct phase noise (blue line) and amplitude noise (green line). Spontaneous emission creates photons whose phases are uncorrelated with that of the lasing field, making the angle ϕ a random variable uniformly

distributed between $[0, 2\pi]$. (Right) The additional photons created by spontaneous emission induce carrier density fluctuations through stimulated emission. This coupling between photons and carriers is called a relaxation resonance and will be discussed in Section 4.2. The phase fluctuation caused by the refractive index change due to carrier density fluctuation is characterized by a parameter called a “linewidth enhancement factor” (α in Equation $\langle \Delta\theta(\tau)^2 \rangle = 2\pi^2\tau S_{\Delta\nu}(\omega)$). (2.33).

Experimentally, the Schawlow-Townes linewidth can be obtained by measuring the power spectral density (PSD) of the frequency noise $S_{\Delta\nu}(f)$. The phase variance of the laser can be written in terms of the frequency noise PSD (double-sided) [29, p. 197],

$$\langle \Delta\theta(\tau)^2 \rangle = 2\pi^2\tau^2 \int_{-\infty}^{\infty} S_{\Delta\nu}(f) \frac{\sin^2(\pi f\tau)}{(\pi f\tau)^2} df. \quad (2.32)$$

If the frequency noise PSD $S_{\Delta\nu}(f)$ is assumed to be a white frequency noise, the integral in the above equation becomes,

$$\langle \Delta\theta(\tau)^2 \rangle = 2\pi^2\tau S_{\Delta\nu}(\omega). \quad (2.33)$$

By replacing the above equation with Equation $\langle \Delta\theta(\tau)^2 \rangle = \frac{R_{sp}^{(l)}}{2N_p} (1 + \alpha^2)\tau$. (2.28), the frequency fluctuation (noise) PSD (double-sided) then can be obtained,

$$S_{\Delta\nu}(f) = \frac{R_{sp}^{(l)}}{4\pi^2 N_p} (1 + \alpha^2). \quad (2.34)$$

2.2.2 Linewidth enhancement factor

The *linewidth enhancement factor* α , also called Henry's alpha parameter or amplitude-phase coupling factor, is defined as the ratio of the real refractive index fluctuation to the imaginary refractive index fluctuation due to a variation of the carrier density in the active region,

$$\alpha \equiv \frac{dn_r/dN}{dn_i/dN} = -\frac{4\pi}{\lambda} \frac{dn_r/dN}{dg/dN} = -\frac{4\pi}{\lambda a} \frac{dn_r}{dN}, \quad (2.35)$$

where $a = dg/dN$ represents a differential material gain and $g = 2k_0n_i = 4\pi n_i/\lambda$ is used.

Physically, the linewidth enhancement factor arises from asymmetry of the differential gain spectrum about the lasing frequency [30]. In the case of quantum-well (QW) lasers (such as ours), α ranges between 2 and 10 [31]. This causes the phase noise created by the carrier fluctuations due to the spontaneous emission to be larger than the direct phase noise by the factor of α^2 (i.e., more than an order of magnitude), and becomes the dominant frequency noise source of semiconductor lasers. Whereas the linewidth enhancement factor in the quantum-dot (QD) lasers is smaller than in the QW lasers. This is because of the high differential gain and a small carrier-induced modulation of the refractive index in the active region. The delta-function-like density of states (DOS) of 0-dimensional QD system yields a narrow symmetrical gain spectrum and subsequently symmetrical differential gain spectrum around the lasing frequency. Ideally, the QD lasers should have zero linewidth enhancement factor, however, it is difficult to achieve ideal QD properties, because of QD size variations. The linewidth enhancement factor less than a value of 1 has been reported for the QD lasers. [32, 33].

2.3 Phase noise reduction in heterogeneous Si/III-V lasers

2.3.1 Limitation of conventional semiconductor lasers

As illustrated in Figure 2.2, in the conventional semiconductor lasers made out of the III-V semiconductors, the cladding layers are heavily-doped to a concentration of 10^{18} to 10^{19} to achieve efficient carrier injection into the active region. The abundant free-carriers (electrons in the n-cladding and holes in the p-cladding layer) in those cladding layers interact with photons through free-carrier absorption (FCA). Thus, the lasers suffer from high loss, and the Q-factor of the lasers has been less than 10^4 .

Also, the larger refractive index in the active region than in the surrounding cladding layers, due to the plasma dispersion effect, causes the mode to be concentrated in the active region, making the peak of the lasing mode profile to be located at the active region (i.e., large $|\bar{E}_l(\bar{r}_a)|^2$) and subsequently, resulting in the high spontaneous emission rate.

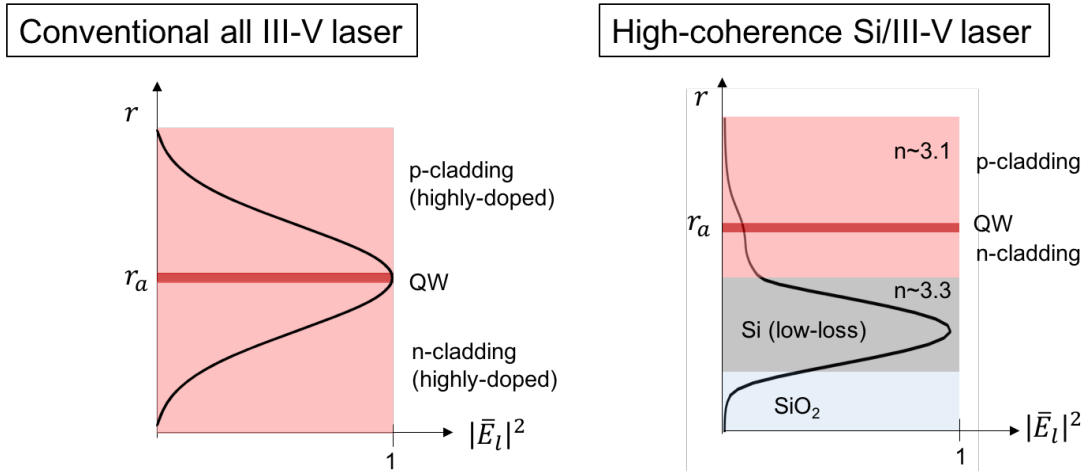


Figure 2.2 Transverse mode profile $|\bar{E}_l(\bar{r}_a)|^2$ in conventional III-V laser and in a heterogeneous Si/III-V laser. (Left) In the conventional semiconductor laser made with III-V, the electric field of the laser mode is maximum at the active region (large $|\bar{E}_l(\bar{r}_a)|^2$), resulting in large spontaneous emission rate ($R_{sp}^{(l)}$). Also, the large confinement in the lossy III-V material leads to high loss and small number of photons (N_p) in the laser. For these reasons, the linewidth of the III-V lasers is limited to the MHz range. (Right) In our heterogeneous lasers with two different Si/III-V materials, most of the light is confined in low-loss Si instead of lossy III-V. Due to low electric field at the active medium (small $|\bar{E}_l(\bar{r}_a)|^2$), we effectively reduce the spontaneous emission rate ($R_{sp}^{(l)}$). Also, due to the small confinement factor in the III-V, a greater number of photons in the laser cavity (N_p) can be achieved. Reduction in gain due to reduced stimulated emission is balanced with reduction in loss, resulting in a constant threshold current density despite the drastic change of electric field distribution in the active region.

Thus, the use of the same layer (i.e., active region) as both photon-generating and photon-storing layers inherently causes this platform to be lossy, and thus limits its linewidth to be in the range of a MHz [34, 35].

2.3.2 Phase noise reduction through modal engineering in heterogeneous lasers

Silicon is transparent for the light of a wavelength, which is bigger than its bandgap wavelength of approximately $1.12 \mu\text{m}$. At the wavelength of $1.5 \mu\text{m}$, absorption of light in Si is negligible. Also, advanced CMOS fabrication technologies allow for the fabrication of the Si waveguide with minimal scattering losses. In Section 3.1.2, we show the implementation of a high-Q Si resonator, in which the Q-factors up to 10^6 were achieved. The availability of the high-Q Si resonators, however, does not by itself yield a narrow-linewidth laser.

In the heterogeneous Si/III-V platform, to achieve a narrow-linewidth laser, the reduction of the modal loss can be accomplished by storing the vast majority of the mode energy in low-loss Si instead of the lossy III-V active region, thus reducing $|\bar{E}_l(\bar{r}_a)|^2$ in the quantum wells. To “push” the mode further into the Si, i.e., to reduce $|\bar{E}_l(\bar{r}_a)|^2$ further, we introduce a thin silicon oxide (SiO_2) layer, which we call the quantum noise control layer (QNCL), between the Si and III-V layers. Figure 2.3 illustrates the change in the transverse mode profile with the increasing QNCL thickness. The mode is “pushed” further into the Si, reducing the electric field “intensity” at the active region ($|\bar{E}_l(\bar{r}_a)|^2$) and the confinement factor in the III-V layer ($\Gamma_{\text{III-V}}$). The reduction of $|\bar{E}_l(\bar{r}_a)|^2$ reduces the spontaneous emission rate into the lasing mode ($R_{\text{sp}}^{(l)}$), and the reduced $\Gamma_{\text{III-V}}$ leads to a greater number of photons in the laser cavity (N_p). The two combined effects reduce the linewidth of the laser effectively.

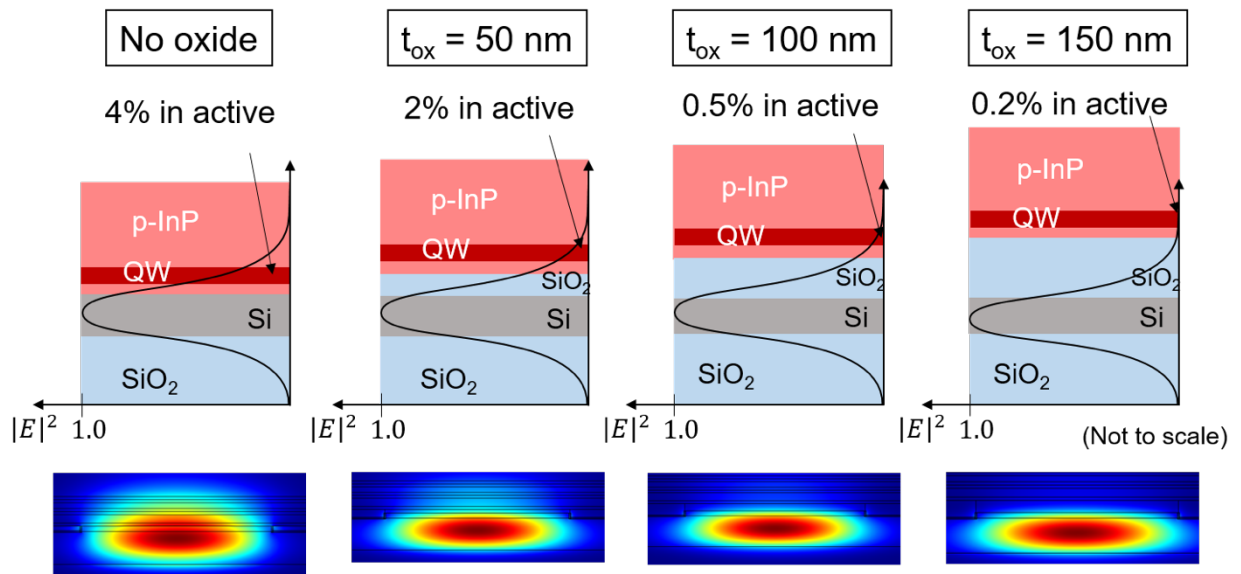


Figure 2.3 SiO_2 layer, which we call the “quantum noise control layer (QNCL)”, is introduced in between Si and III-V to further push the mode into the Si layer and reduce the confinement factor in the active region (QWs). (Top figures) The peak of the transverse mode profile stays further away from III-V (i.e., reduced $|\bar{E}_l(\bar{r}_a)|^2$), and the confinement factor in the QWs decreases with thicker QNCL thickness. (Bottom figures) COMSOL simulation showing the transverse mode profile with varying QNCL thickness. The reduction of the QW confinement factor with increasing QNCL thickness is evident.

This strategy of reducing the frequency noise fluctuation by pushing the mode further into the Si continues to work until the loss from the Si becomes comparable to the loss from the III-V.

From that point on, the overall improvement begins to saturate (i.e., saturation of the total Q-factor), but the reduction in gain continues. The imbalance between the reduction in the gain and loss then leads to an increase in the threshold carrier density to maintain the gain that matches the no-longer-decreasing modal loss. In turn, the increase in the threshold carrier density causes an increase in the spontaneous emission rate, diminishing the returns in reducing the phase noise.

Threshold current and output power

As long as the dominant loss in the laser cavity is the loss in III-V, the reduction in the gain, loss, and the spontaneous emission rate occurs at the same scale, as modal engineering shifts modal energy away from the active region. As a result, the reduction in the laser linewidth can be achieved, while parameters such as the threshold carrier density, differential quantum efficiency (the ratio between the generated photon number and the injected carrier number, i.e., $\frac{dP_0/h\nu}{dI/q}$), and subsequently, the optical output power are unaffected by the modal engineering.

2.4 Conclusions

In this chapter, we showed theoretically that by storing the vast majority of the modal energy in the low-loss Si rather than in the high-loss III-V active region, we can reduce the linewidth of the semiconductor lasers by two to three orders of magnitude, while keeping other parameters (e.g., threshold current density, output power density) the constant. In Chapter 3, we will provide experimental evidence that the dramatic linewidth reduction is possible through the modal engineering.

Chapter 3

PHASE NOISE REDUCTION IN HETEROGENEOUS SI/III-V LASERS

In Chapter 2, we discussed the modal engineering between the low-loss Si and high-loss III-V active layer as a way to reduce the linewidth of a laser by decreasing the total loss of a laser cavity (i.e., increasing the Q-factor), while keeping the other parameters such as the threshold current density, and output power density constant. Thus, it is critical to implement a high-Q resonator in the low-loss Si for this modal engineering strategy to be effective. In this chapter, we experimentally demonstrate the achievement of a few to tens of kHz linewidth in our lasers fabricated using the high-Q Si resonator through the modal engineering strategy.

In the 1st part of the chapter, the design and measurement results of the fabricated high-Q Si resonator will be presented. In the 2nd part, measurement results of the fabricated lasers including the frequency noise measurements are described.

3.1 High-Q Silicon resonator for high-coherence heterogeneous lasers

To achieve higher total Q-factor using the modal engineering between Si and InP and thus a narrow intrinsic quantum-limited linewidth in laser, a high-Q cavity needs to be employed as an integral part of the laser resonator. In this work, a 1D-grating-based defect-mode resonator is utilized to implement a high-Q cavity in Si for various purposes including support of a single mode with a very high-Q factor, ease of change of mirror strength, and small footprint required on-chip.

In this section, the design and the measurement results of the high-Q Si resonator will be presented. The fabrication part of the resonator will be discussed in Appendix A.

3.1.1 Si resonator design

Transverse Si waveguide design

As discussed in Chapter 2, increasing Q-factor in the Si/III-V lasers requires that most of the modal energy be confined in the low-loss Si rather than in the lossy III-V active layer.

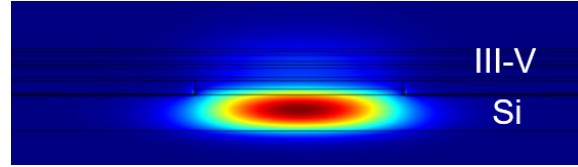


Figure 3.1 Optical field intensity distribution of TE_0 mode in the 2D Si/III-V laser simulation.

To confine more modal energy in the Si than the III-V layer, Si must have a larger refractive index than InGaAsP/InP epi-wafer (~ 3.45). This is achieved using an SOI wafer with 500 nm thick Si, which is thicker than conventional photonic-application SOI wafers with 200 to 400 nm Si. A shallow etch into the Si is utilized in order to mitigate the interaction of the optical mode with the sidewalls, thus minimizing the loss from sidewall scattering. This also enables the use of a long defect-section in our resonators, minimizing leakage loss to the radiation modes. The width of the Si waveguide is chosen to accommodate TE_0 and TE_1 mode in the waveguide. Due to TE_1 mode's odd transverse symmetry, it interacts minimally with gratings that have even transverse symmetry. Figure 3.1 shows the optical traverse profile of the TE_0 mode in our Si/III-V waveguide. The design parameters of the Si waveguide are shown in Table 3.1.

Parameters	Value
Si waveguide thickness	500 nm
Si waveguide width	[1:0.5:2.5] μm
Si rib waveguide etch depth	60 nm
SiO ₂ QNCL thickness (t_{QNCL})	50 ~ 150 nm

Table 3.1. 2D Si waveguide design parameters

We have designed and tested a series of lasers where the thickness of the SiO₂ quantum noise control layer (QNCL) varies from 50 to 150 nm. The confinement factor in each layer of Si, III-V, and QW is shown in the Table 3.2 for each thickness. When t_{QNCL} is 150 nm, the confinement factor in Si reaches 99%, leaving less than 1% in III-V.

t_{QNCL}	Γ_{Si}	$\Gamma_{\text{III-V}}$	Γ_{QW}
0 nm	0.79	0.21	0.031
50 nm	0.90	0.10	0.015
100 nm	0.96	0.03	0.006
150 nm	0.99	0.003	0.002

Table 3.2 Confinement factors in Si, III-V, and QW layer for various QNCL thickness.

1D grating mode-gap resonator design

In 1D-grating-based mode-gap resonators, a photon-bandgap effect is used to confine light in the in-plane direction. In-plane gratings in the Si waveguide are designed such that its defect section shapes its photonic well to be parabolic (Figure 3.3Figure 3.4), analogous to an electron in a parabolic potential well. The mode in the parabolic potential well exhibits a well-defined Gaussian spatial field envelope along the z -direction (i.e., wave-propagating direction). Our design features an especially long defect length. The gentle z -variation of the grating reduces radiation loss to unbound radiation modes. In our elongated defect section with a parabolic potential well, the envelope of the in-plane mode profile varies gently, but still remains spatially localized as a Gaussian function [37, 38, 39, 40].

Reflectors for the resonator that bound the defect section are made using periodic gratings. The gentle variation in the defect section is made by gradually modulating the strength of the gratings. In our design, we choose to vary the width W_y of the gratings in the direction perpendicular to the z -direction (Figure 3.2).

To obtain the band edge frequencies, i.e., conduction band frequencies f_c and valence band frequencies f_v for each grating size, a 3D unit cell simulation is performed using the commercial finite element method software Comsol, and the eigenfrequencies of the infinitely long 3D unit grating are searched. To reduce computation time, the grating unit cell is cut in half along the light propagating direction (z -direction in Figure 3.2), and the perfect electric conductor (PEC) boundary condition is applied to the cut boundary for the simulation of the even TE_0 mode. To further reduce the computation time, the grating is cut in half once again along the x -direction, and the PEC and PMC (perfect magnetic conductor) boundary condition is properly applied to each surface to extract the eigenfrequencies of the dielectric and the air mode as a function of a W_y [40]. The conduction band frequency f_c is extracted from the air mode, and the valence band frequency

f_v is extracted from the dielectric mode. Using these band edge frequencies, along with our pre-defined parabolic well structure, the spatial mode profile in the cavity and the mirror strength (i.e., external Q-factor) can be obtained using the 1D coupled-mode equation.

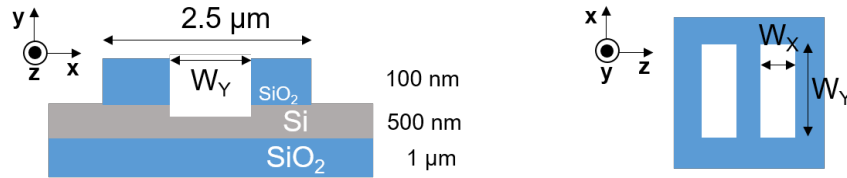


Figure 3.2 Grating unit cell model for 3D periodic grating simulation.

Parameters	Value
Si layer thickness	500 nm
Si waveguide width	2.5 μm
Si rib waveguide etch depth	60 nm
SiO ₂ QNCL thickness (t_{QNCL})	100 nm
Grating period	240 nm
W_x	120 nm
Etch depth difference between grating and trench area due to ARDE effect	15 nm

Table 3.3 3D grating unit cell simulation parameters.

For our resonators, we design and fabricate both the accept-mode and donor-mode type resonators, of which the optical band structure is shown in Figure 3.3 and Figure 3.4, respectively [41].

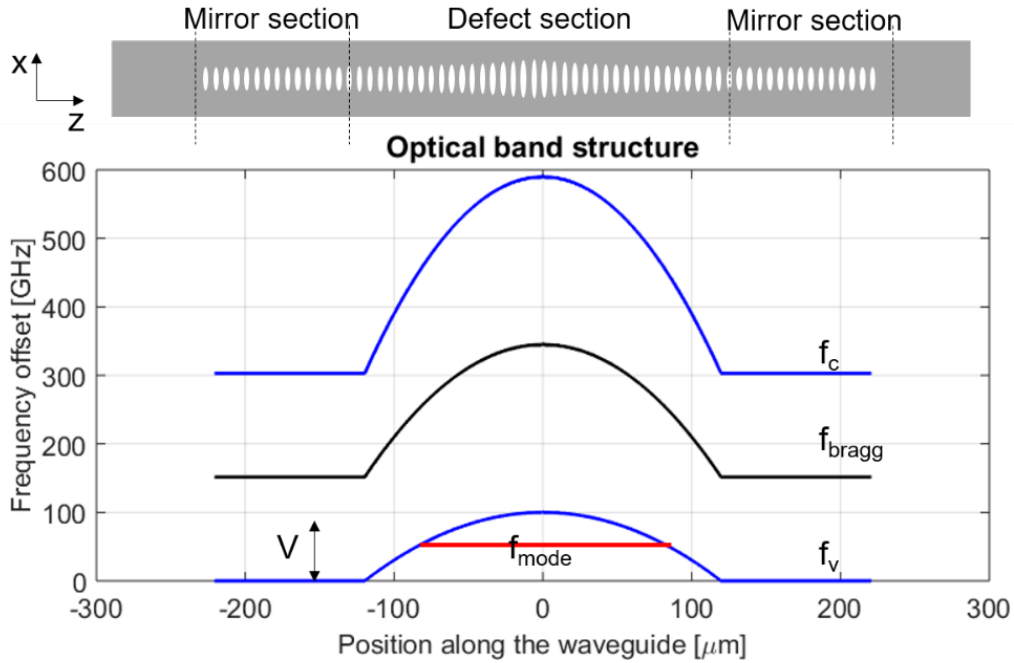


Figure 3.3 Schematic of the acceptor-type defect mode resonator and its optical band structure.

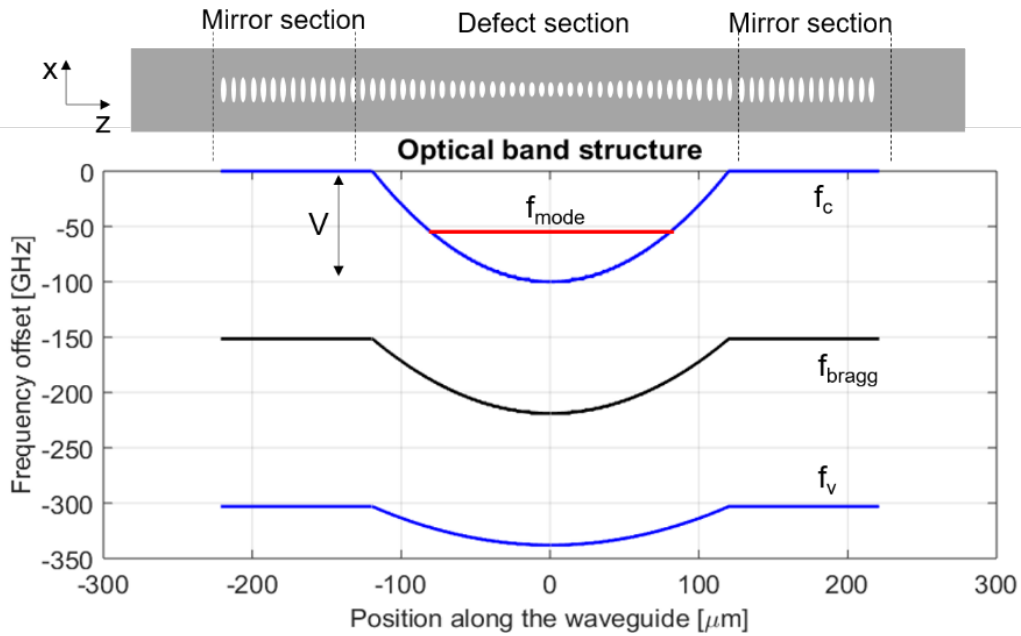


Figure 3.4 Schematic of donor-type defect mode resonator and its optical band structure.

For both type of the resonators, two kinds of the photonic well depth $V = 70, 120$ GHz were used. Even though the photon well depth of 70 GHz creates a single-mode in the photonic well, 120 GHz was included in the design to create a mode in the well even when the Si material was under-etched.

For the mirror section of the resonator, periodic gratings with $W_y = 300$ nm (coupling coefficient $\kappa = 110$ cm⁻¹) are used, creating a photonic bandgap of approximately 300 GHz (Figure 3.3 and Figure 3.4).

The mirror strength is designed to cover all the external coupling regimes from the over-coupling ($Q_{\text{ext}} < Q_{\text{int}}$) to the under-coupling regime ($Q_{\text{ext}} > Q_{\text{int}}$). Table 3.4 shows the external Q-factor in terms of the mirror length. The external coupling strength to achieve an optimum laser output power can be theoretically calculated [26, p. 248], and was found to be approximately when Q_{ext} is 0.3 to 0.5 of Q_{int} . In the later laser measurements, the optimum output power was achieved when the mirror had the number of grating holes $N_{\text{mirror}} = 1200$ and $N_{\text{mirror}} = 1600$ for the 50 nm and 90 nm QNCL lasers, respectively. More details about this resonator design can be found in [42].

Number of grating holes in the mirror section	Length of the mirror (μm)	External Q-factor	Reflectivity (R)
400	96	1.6×10^4	0.63
800	192	7.2×10^4	0.90
1200	288	1.9×10^5	0.96
1600	384	3.8×10^5	0.98
2000	480	4.8×10^6	0.99

Table 3.4 External Q-factor as a function of number of grating holes in the mirror section (for the reflectivity calculation, the laser cavity round time τ_L of 6 ps was used).

3.1.2 Si resonator passive measurement

The transmission spectrum of the donor-type mode-gap resonator as a function of frequency is shown in Figure 3.5. The high-Q mode from the donor-type mode-gap resonator is found to be

resonant at a wavelength inside the photonic bandgap, near the conduction band edge (high frequency). In the top figure, the resonance wavelength is near 1565 nm, and the measured Q-factor is 10^5 , limited by the external Q-factor (mirror loss). With an under-coupled mirror, as shown in the bottom figure, the loaded Q-factor reaches 1 million, implying that the intrinsic Q-factor of the localized mode is near 1 million.

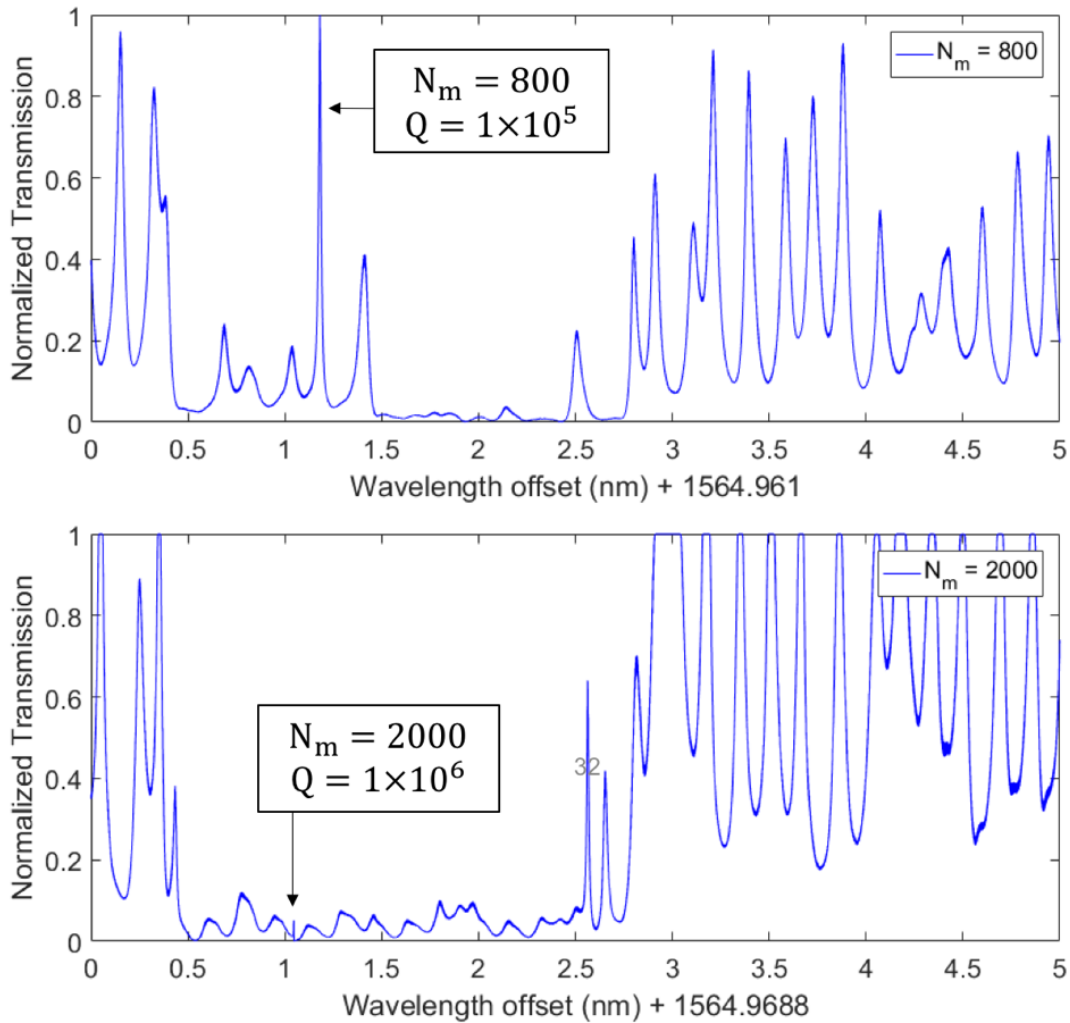


Figure 3.5 Transmission spectrum of high-Q Si resonators (Top figure: donor-type mode, $N_{\text{defect}} = 299$, $N_{\text{mirror}} = 800$, $V = 200$ GHz, bottom figure: donor-type mode, $N_{\text{defect}} = 299$, $N_{\text{mirror}} = 2000$, $V = 200$ GHz).

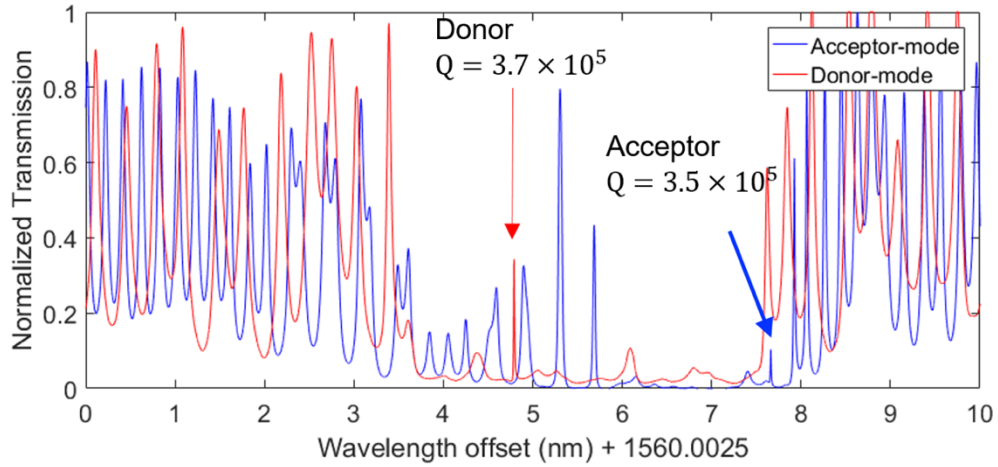


Figure 3.6 Transmission spectrum of passive Si resonators with donor-type (in red) and acceptor-type (in blue) mode (Donor-mode: $N_{\text{defect}} = 499$, $N_{\text{mirror}} = 1200$, $V = 150$ GHz, acceptor-mode: $N_{\text{defect}} = 299$, $N_{\text{mirror}} = 2000$, $V = 150$ GHz).

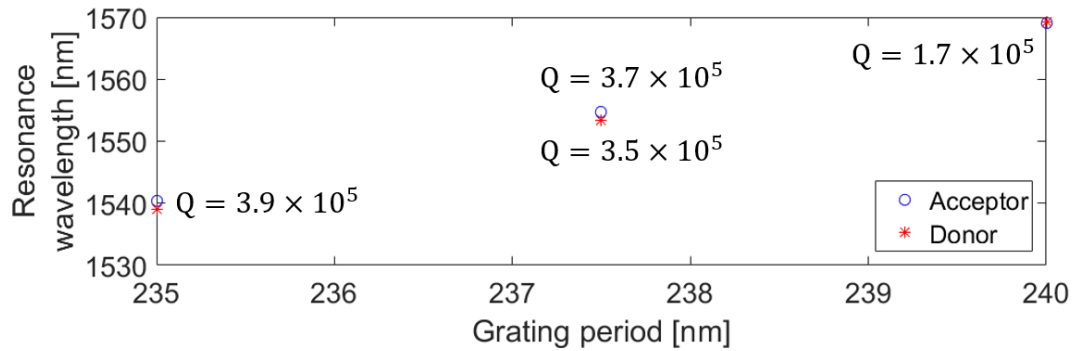


Figure 3.7 Grating period vs. resonance wavelength of the Si resonator. Resonance wavelength can be coarsely tuned by varying the grating period. Grating period difference of 2.5 nm leads to

resonance wavelength difference of ~ 15 nm. In all wavelength, Q-factor larger than 10^5 is achieved.

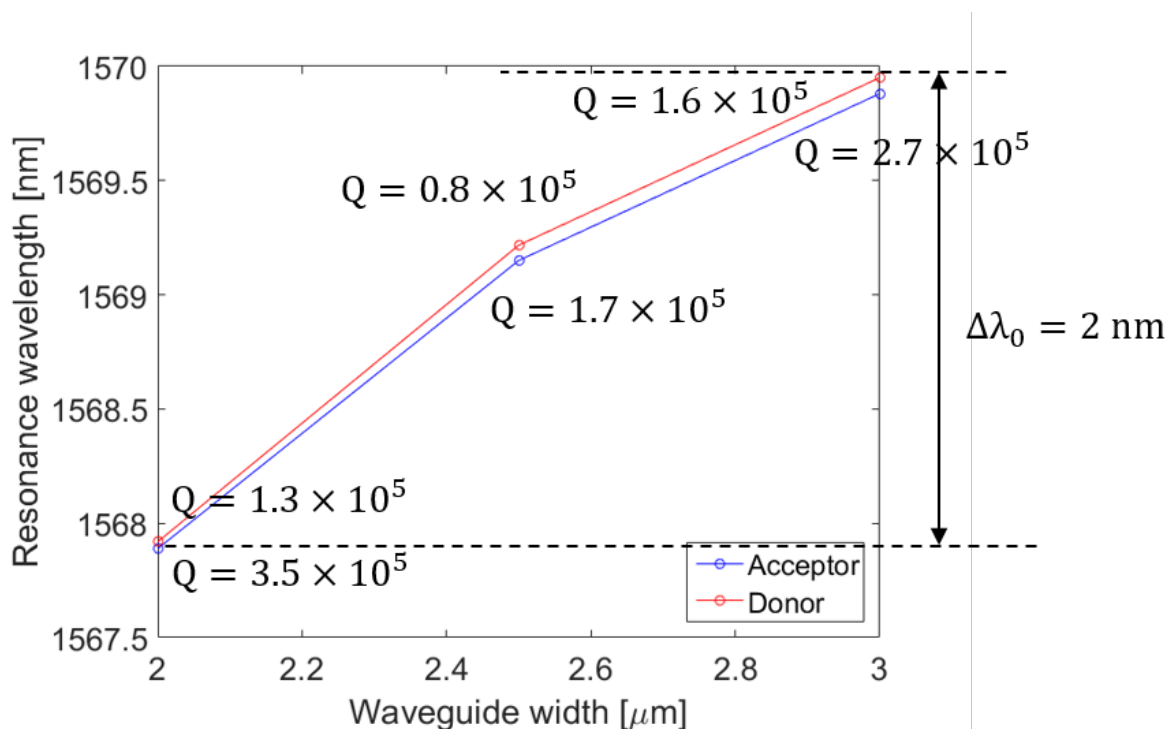


Figure 3.8 Grating period vs. resonance wavelength of the Si resonator. Resonance wavelength can be coarsely tuned by varying the grating period. Grating period difference of $2.5 \sim \text{nm}$ leads to resonance wavelength difference of ~ 15 nm. In all wavelength, Q-factor larger than 10^5 is achieved.

Figure 3.6 shows overlaid plots of transmission spectra of donor- and acceptor-type modegap resonator. The acceptor-type mode resides near the valence band edge (low frequency), in contrast with the donor-type mode in the low wavelength. Similar Q-factors have been observed between the acceptor- and donor-type resonators.

These in-plane resonators can be fabricated into a dense array of lasers, with each device emitting a different wavelength, which is suitable for applications such as WDM. The Bragg condition $\lambda_B = 2n_{\text{eff}}a$ reveals that either the grating period or effective refractive index can be varied to change the resonance wavelength.

The coarse resonance wavelength tuning can be obtained by varying the grating period. The grating period is varied from 235 to 240 nm with a step of 2.5 nm. The fixed grating period change of 2.5 nm is limited by the nominal minimum beam step size of e-beam lithography. Figure 3.7 shows that the resonance wavelengths are distributed between 1540 and 1570 nm, and a change of

the grating period by 2.5 nm gives a resonance wavelength change of approximately 15 nm. Q-factors larger than 10^5 are achieved at all grating periods.

Fine-tuning of the resonance wavelength can be achieved by varying the effective refractive index, which can be accomplished with the waveguide variation. Figure 3.8 shows that when the waveguide width is varied from 2 to 3 μm , the resonance wavelength changes by 2 nm. This fine-tuning range of 2 nm is not enough to cover the coarse wavelength tuning of 15 nm. However, this limitation can be circumvented by using the scaling feature of the e-beam lithography. By varying the lens current, the field scaling and the arbitrary step size of the e-beam can be obtained. This limitation also can be avoided when patterns are written using optical lithography with feasible resolution and a continuously scaling optical mask.

3.2 Laser measurements

In this section, the laser measurement results are presented. The III-V mesas are fabricated two different ways in this thesis: one method employs the ion implantation and the other the oxide-confinement. The III-V wafers are InP-based and have five InGaAsP quantum wells (QWs). The fabrication procedure is discussed in A.2. The lasers with the QNCL thickness of 50 and 90 nm are fabricated.

3.2.1 LIV and OSA measurement

The devices are mounted such that the Si substrate in an SOI wafer makes contact with a temperature-controlled copper heat sink. The light-current characteristic of the fabricated lasers is shown in Figure 3.9.

The threshold current of the 50 nm QNCL laser is 55 mA, and that of the 90 nm laser 65 mA. Despite the dramatic decrease in the confinement factor in the active region in the 90 nm QNCL laser compared with the 50 nm laser, they possess similar thresholds. This demonstrates our claim that the threshold current remains constant even with the reduction of the laser modal gain when the QNCL thickness increases. This is due to the fact that the drop in optical losses, with the increasing QNCL thickness, is nearly the same as the drop in the gain.

The output power from the lasers is in the range of 2 mW. Thermal roll-off occurs around 200 mA at 20°C in both lasers. The roll-off at relatively low current is due to the high thermal impedance in the laser and subsequent high rise of the temperature in QW. The poor thermal

conductivity mostly comes from the QNCL oxide layer and the buried oxide layer between the QW and the heat sink underneath the Si substrate. The maximum pumping current of the laser can be increased by improving the thermal conductivity of the laser by directing heat generated in the QW to the III-V layer. This can be accomplished using a flip-chip bonding technique [43] or thermal shunt method [44, 45].

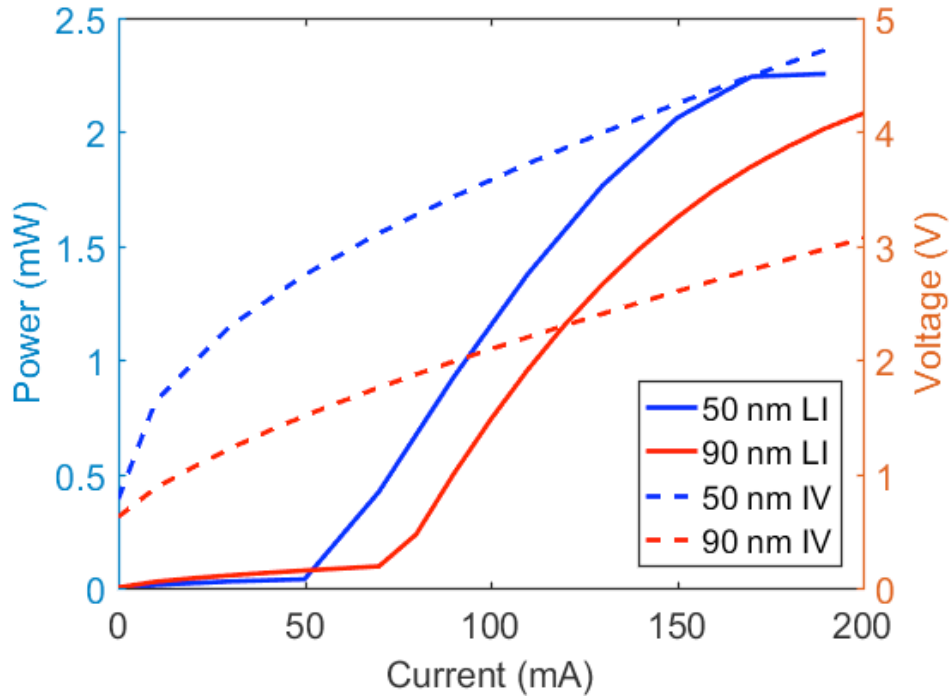


Figure 3.9 Light-current and current-voltage characteristics of the fabricated lasers with 50 nm (device ID: hQsp6 ch01 slot2 bar6 dev5) and 90 nm (hQsp7 ch9 slot1 bar4 dev9) QNCL lasers.

3.2.2 Temperature dependence

The temperature dependence of the laser is determined by taking LI curves while varying the stage temperature. Figure 3.10 shows the LI characteristics when the stage temperature is varied from 20 °C to 45 °C. We achieve the lasing operation up to 45 °C. Overall characteristic temperature (T_0) and above-threshold characteristic temperature (T_1) are extracted using the formula $I_{\text{th}} = I_0 e^{T/T_0}$ and $I - I_{\text{th}} = I_{p0} e^{T/T_1}$. T_0 of 51 °C and T_1 of 80 °C have been obtained.

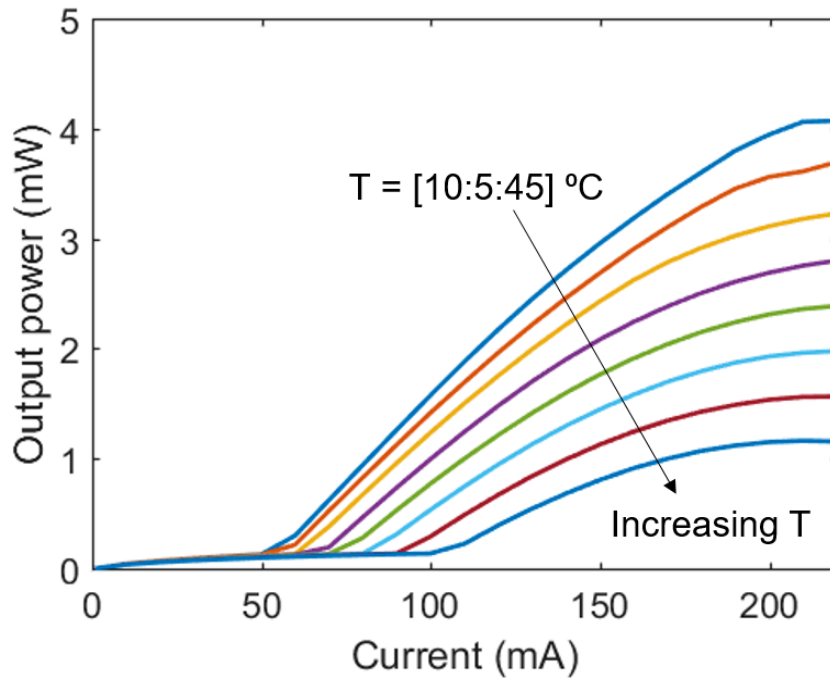


Figure 3.10 Light-current and current-voltage characteristics of the 50 nm QNCL laser at different stage temperatures (device ID: hQsp6 ch01 slot2 bar06 dev05).

The optical spectrum is taken using an optical spectrum analyzer with the resolution bandwidth of 0.08 nm. Figure 3.11 shows the optical emission spectrum of the 50 nm and 90 nm QNCL lasers at the bias current of 160 mA and 190 mA, respectively. The lasers exhibit stable single-mode operation with a side-mode suppression ratio (SMSR) of greater than 45 dB at the lasing wavelength of 1577 nm and 1556 nm.

As shown in Figure 3.12, a differential lasing wavelength rate of 0.012 nm/mA in the 50 nm QNCL laser has been obtained. Figure 3.13 shows the spectra of the 90 nm QNCL lasers when the grating period is varied between 237.5 and 242.5 nm with a step of 2.5 nm.

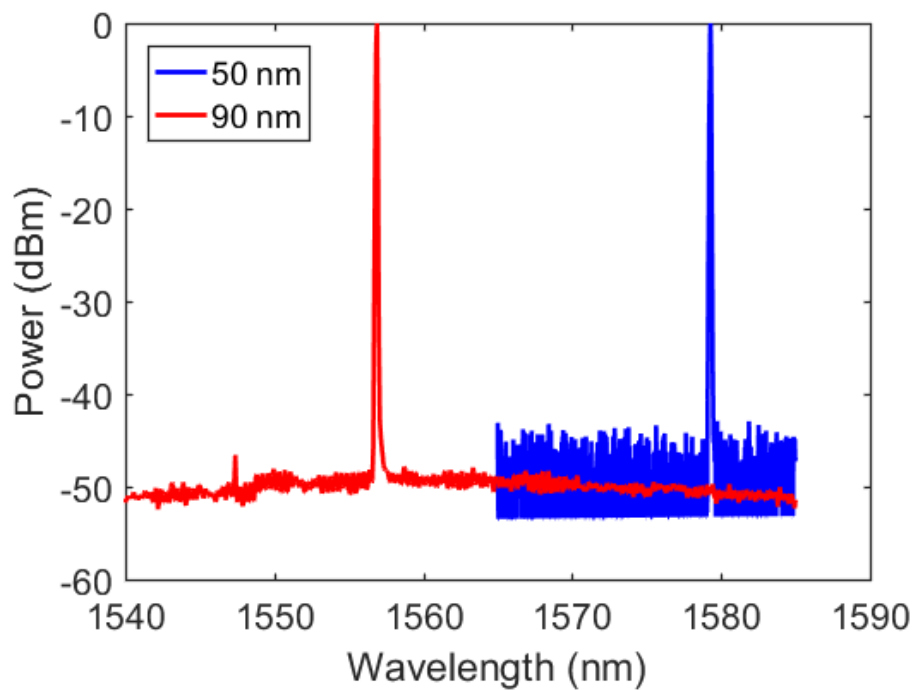


Figure 3.11 Optical emission spectrum of the 50 nm and 90 nm QNCL laser at 160 mA and 190 mA, respectively (device ID: hQsp6 ch01 slot2 bar6 dev5, hQsp7 ch09 slot1 bar04 dev09).

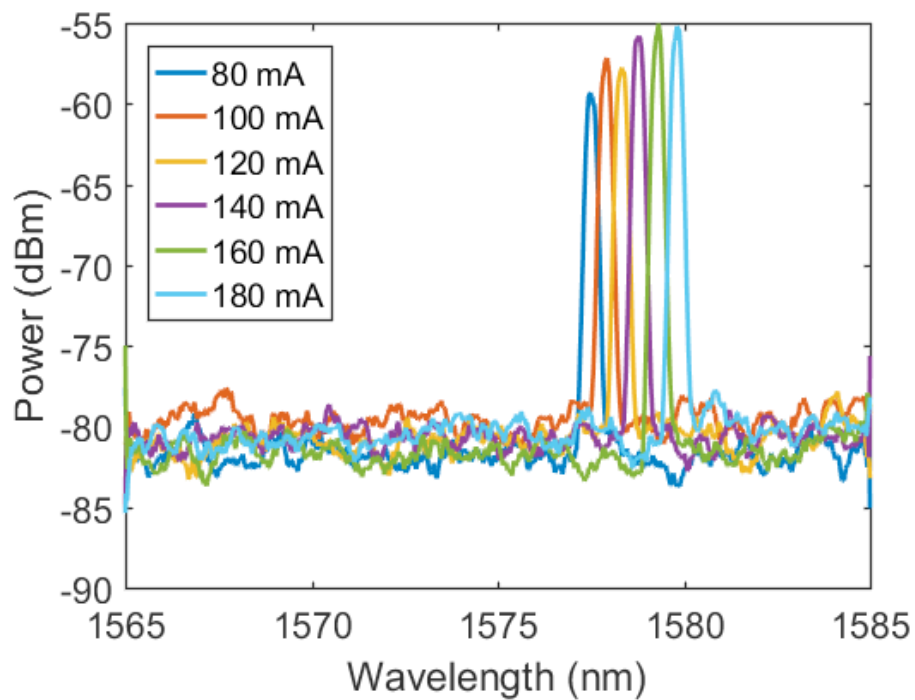


Figure 3.12 Optical emission spectrum of the 50 nm QNCL laser at different currents (device ID: hQsp6 ch01 slot2 bar06 dev05).

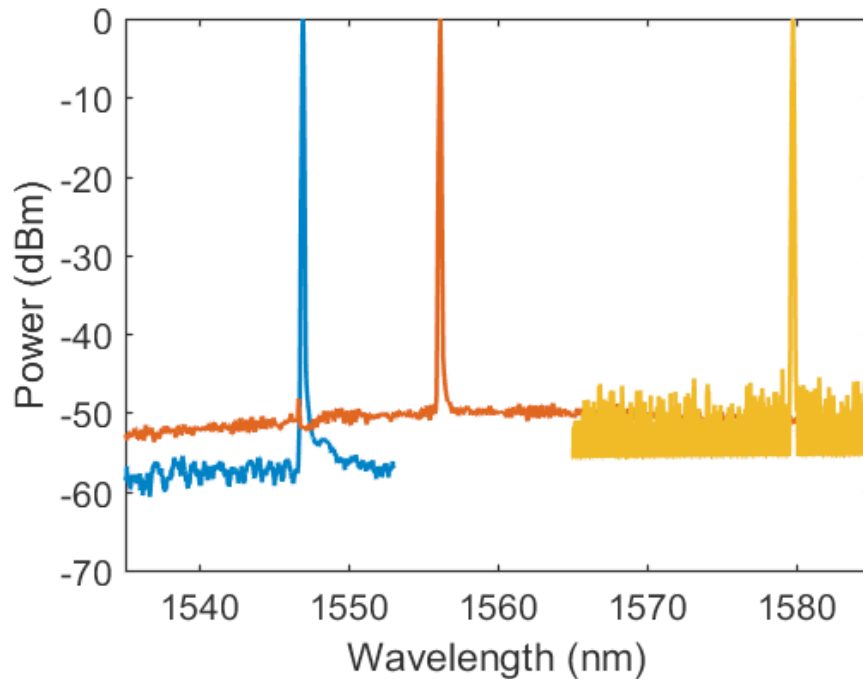


Figure 3.13 Optical emission spectrum of the three different 90 nm QNCL lasers. Each device has a different grating period.

3.3 Frequency noise measurements

3.3.1 Measurement setup

Frequency noise due to spontaneous emission can be determined by measuring the power spectral density (PSD) of the phase deviation $\Delta\theta$. Figure 3.14 displays the frequency noise measurement setup.

A ultra-low noise laser diode driver (ILX lightwave, LDX-3620B) is used to pump the laser, and the laser light is collected using a lensed fiber (tapered PM fiber with AR coated, TPMJ-3A-1550-8/125-0.25-5-2-12-0.5-AR). Two optical isolators are placed after the lensed fiber to prevent undesirable external reflections from affecting the laser linewidth.

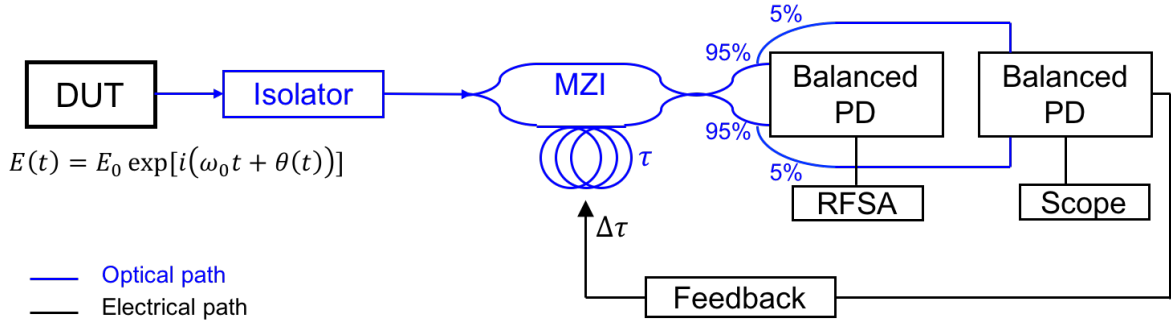


Figure 3.14 Frequency noise measurement setup (DUT: device under test, PD: photodetector, MZI: Mach–Zehnder interferometer, RFSA: RF spectrum analyzer).

A Mach-Zehnder interferometer (MZI) with a FSR of 1.575 GHz ($\tau = 0.6$ ns) is used as a frequency discriminator by converting phase fluctuations into photocurrent fluctuations. MZI output is split into two photodetectors using 95%/5% fiber optic couplers. 5% tab of the MZI output is connected to a slow photodetector (PD, New-Focus 1817), and used to stabilize and lock the differential phase between the two arms at the quadrature point ($\omega_0 \tau = \pi/2$) for the duration of the measurement [46]. One of the arms of the MZI was mounted on a piezo-electric fiber stretcher (Evanescent Optics, 915B). The output of the slow PD is routed to an electronic feedback circuit (custom battery powered), which is connected to the piezo-electric controller (Evanescent Optics, 914) and drives the fiber stretcher. The two 95% tabs of the MZI are connected to a fast balanced photodetector (PD, Optilab BPR-20-M), which removes most of the intensity noise present in the field. The PSD of the photocurrent generated by the PD is measured by an RF spectrum analyzer to extract the frequency noise PSD and finally the laser linewidth.

The laser's linewidth is extracted from the measured PD current PSD as follows. The collected laser's electric field is expressed with the amplitude of the field $A(t)$, the lasing frequency ω_0 , and the phase fluctuation caused by lasing frequency noise $\theta(t)$,

$$E(t) = A(t)e^{i(\omega_0 t + \theta(t))}. \quad (3.1)$$

The optical field is then sent through the MZI, and the field at the output of the MZI is written as

$$E_{\text{MZI}}(t) = \frac{1}{2} [E(t) - E(t - \tau)]. \quad (3.2)$$

The output of the MZI is measured with a photodetector, which generates a photocurrent proportional to the intensity of the field. The photocurrent from each output of the balanced PD can be expressed using the phase difference between the two MZI arms $\Delta\theta(t, \tau) = \theta(t) - \theta(t, \tau)$ and a phase to photocurrent gain conversion factor I_g

$$I_{\text{PD one port}}(t) = I_0 \pm \frac{I_g}{2} \cos(\omega_0\tau + \Delta\theta(t, \tau)) \quad (3.3)$$

Then, the output of the balanced PD is the sum of each output, and is written as

$$I_{\text{BPD}}(t) = I_g \cos(\omega_0\tau + \Delta\theta(t, \tau)). \quad (3.4)$$

The interferometer is locked at quadrature ($\omega_0\tau = \pi/2$) and under the assumption that the phase fluctuation $\Delta\theta(t, \tau)$ is small enough, the PD current generated by the balanced PD becomes proportional to $\Delta\theta(t, \tau)$,

$$I_{\text{BPD}}(t) = I_g \Delta\theta(\tau). \quad (3.5)$$

The phase to current gain conversion factor I_g is found experimentally by modulating $\omega_0\tau$ from its quadrature point and measuring the maximum excursion of the voltage recorded on a oscilloscope. Since our lasers emitted more than 2 mW of optical power in free space, it was possible to obtain 1 mW in fiber with careful alignment of the lensed fiber. Possessing optical power more than 1 mW in fiber allowed us to perform the frequency noise measurement without any use of an amplifier, making our gain conversion factor I_g the same as the DC current I_0 . The DC current I_0 was characterized at various levels of optical power, using a frequency chirped laser developed in the group [47], and used as the gain factor I_g .

The RF spectrum analyzer measures the PSD of the PD current ($S_{I_{\text{PD}}}(\omega)$, one-sided, W/Hz), which can be converted into the PSD of the phase fluctuation ($S_{\Delta\theta}(\omega)$, Hz^2/Hz):

$$S_{I_{\text{PD}}}(\omega) = I_g^2 R_L S_{\Delta\theta}(\omega), \quad (3.6)$$

where R_L is the load resistance (50 Ω) of the spectrum analyzer. The phase noise PSD can be related to the PSD of instantaneous frequency deviation Δf [29, 48] by

$$S_{\Delta\theta}(\omega) = (2\pi)^2 \tau^2 S_{\Delta\nu}(\omega) \frac{\sin^2(\omega_0\tau/2)}{(\omega_0\tau/2)^2}. \quad (3.7)$$

Therefore, the PSD of instantaneous frequency deviation Δf can be obtained from $S_{I_{PD}}(f)$ yielding,

$$S_{\Delta\nu}(\omega) = \frac{S_{I_{PD}}(\omega) \cdot R_L}{(2\pi)^2 v_g^2 \tau^2 \text{sinc}^2(\omega_0/2\text{FSR})}. \quad (3.8)$$

The phase variance of a laser can be written in terms of the frequency noise PSD $S_{\Delta\nu}(f)$ [29, p. 197],

$$\langle \Delta\theta(\tau)^2 \rangle = \frac{\tau^2}{\pi} \int_{-\infty}^{\infty} S_{\Delta\nu}(\omega) \frac{\sin^2(\omega\tau/2)}{(\omega\tau/2)^2} d\omega. \quad (3.9)$$

If the frequency noise PSD $S_{\Delta\nu}(f)$ is assumed to be a white frequency noise, the integral in the above equation becomes,

$$\langle \Delta\theta(\tau)^2 \rangle = \pi\tau S_{\Delta\nu}(\omega). \quad (3.10)$$

Replacing the above equation with Equation $\langle \Delta\theta(\tau)^2 \rangle = \frac{R_{sp}^{(l)}}{2N_p} (1 + \alpha^2)\tau$. (2.28) relates the Schawlow-Townes linewidth with the one-sided white frequency noise PSD by,

$$\Delta\nu = \pi S_{\Delta\nu}. \quad (3.11)$$

Therefore, the Schawlow-Tones linewidth can be obtained using the above formula at the white noise floor.

The dark noise of the PD set the ultimate noise signal that can be measured. The PSD of the dark noise from the photodetector is subtracted from the photocurrent PSD $S_{I_{PD}}(\omega)$, and the gain profile of the photodetector is also accounted for after subtraction of the dark noise.

3.3.2 Experimental results

Figure 3.15 shows the frequency noise PSD for the laser with QNCL thickness 50 nm ($I_{th} = 55$ mA).

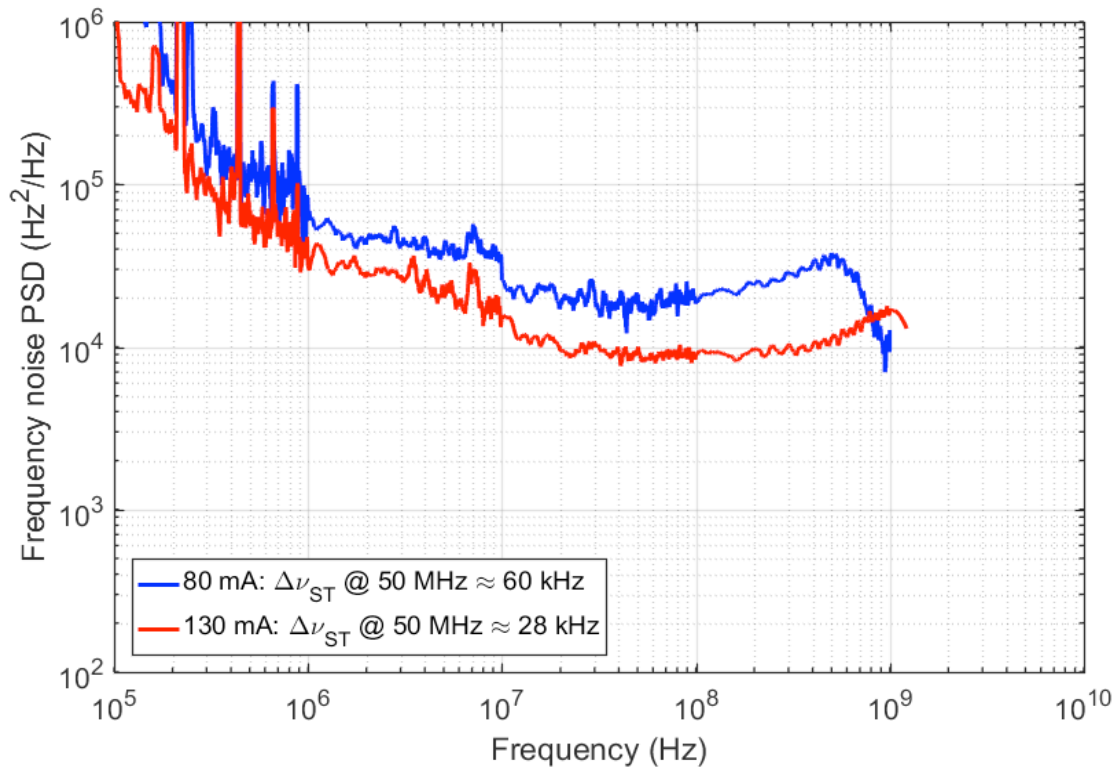


Figure 3.15 Frequency noise power spectral density of the 50 nm QNCL laser (device ID: hQsp6 ch01 slot2 bar06 dev05).

As discussed in Section 2.2, the steep $1/f$ noise is observed in the low frequency region up to 10 MHz. Noise from spontaneous emission is found when the spectrum reaches a flat white frequency floor, which is observed at the flat line at the frequencies between 10 and 100 MHz. The frequency noise PSD ($S_{\Delta\nu}$) at the flat floor measures to be 1.9×10^4 Hz²/Hz for the current of 80 mA. This value can be converted to the Schawlow-Townes linewidth of 60 kHz using Equation

$\Delta\nu = \pi S_{\Delta\nu}$. (3.11). When the current is increased to 130 mA, the frequency noise drops to $8.9 \times 10^3 \text{ Hz}^2/\text{Hz}$ (Schawlow-Townes linewidth: 28 kHz).

Figure 3.16 shows the frequency noise PSD for the laser with QNCL of 90nm ($I_{\text{th}} = 65 \text{ mA}$). The same $1/f$ noise is observed up to 10 MHz. In this laser, the white noise floor drops even further down to 14 kHz at the current of 45 mA above threshold, and 4 kHz at 125 mA above threshold.

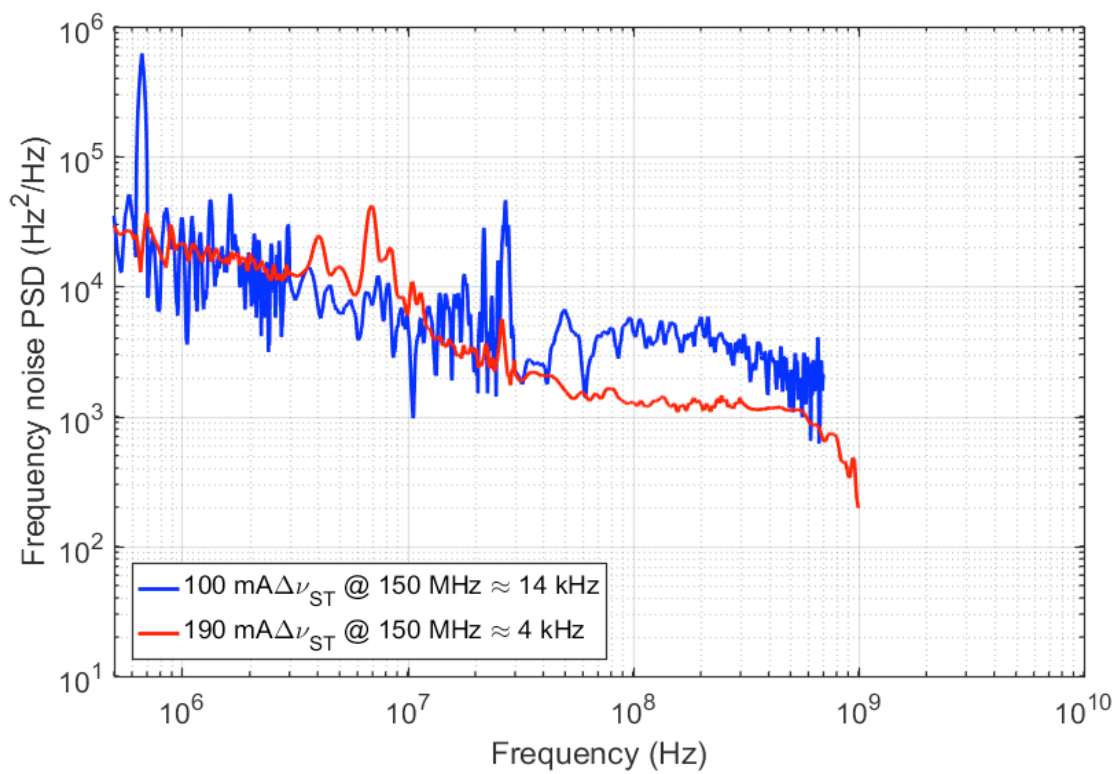


Figure 3.16 Frequency noise power spectral density of the 90 nm QNCL laser (device ID: hQsp7 ch9 slot1 bar4 dev9).

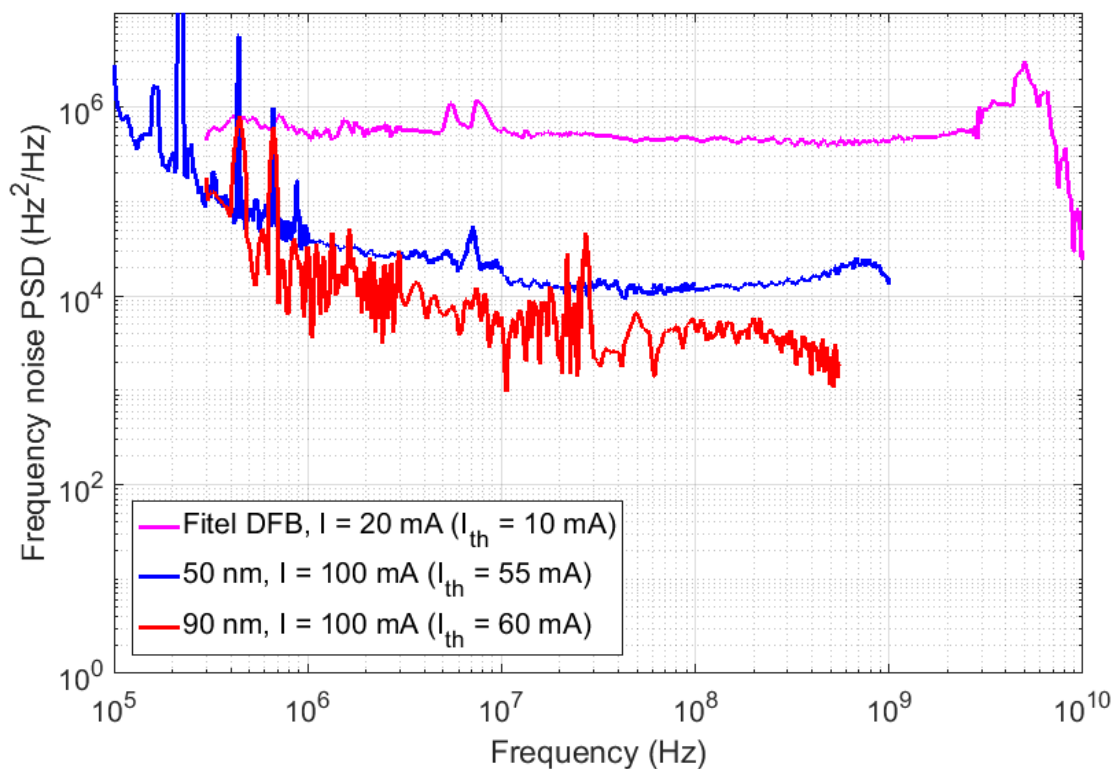


Figure 3.17 Frequency noise PSD of the 50, 90 nm QNCL lasers. The commercial laser from Fitel is plotted for comparison.

Figure 3.17 shows the frequency noise PSD of the 50 and 90 nm QNCL lasers together when the current is about 40 mA above threshold. A commercially available DFB laser manufactured by Fitel (model number) is presented as a control. The commercial laser shows the linewidth larger than 1 MHz, as opposed to our narrow-linewidth lasers having the linewidth in the range of a few tens of kHz.

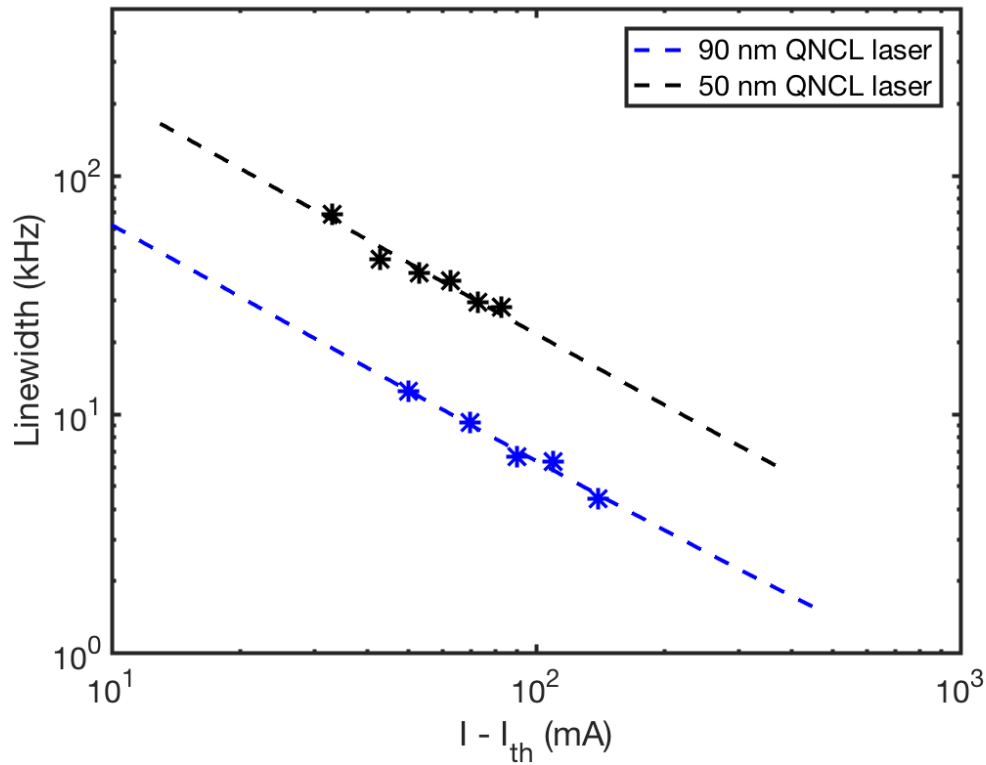


Figure 3.18 Linewidth as a function injection current above the threshold current for the 50 nm (device ID: hQsp6 ch01 slot2 bar06 dev05) and 90 nm (device ID: hQsp7 ch9 slot1 bar4 dev9) QNCL lasers.

The Schawlow-Townes linewidth has a $(I - I_{th})^{-1}$ dependence according to Equation 2.79. Figure 3.18 shows the fitted line for the linewidths of the 50 and 90 nm QNCL lasers, plotted together with the linewidth measured at each current above threshold. It can be seen that the linewidth of the 90 nm laser is smaller almost by $\times 4$ compared to the 50 nm laser.

Figure 3.19 shows a scatter plot of the minimum linewidth measured for the lasers with output power larger than 1.5 mW. Figure 3.20 shows the minimum linewidth measured at each wavelength.

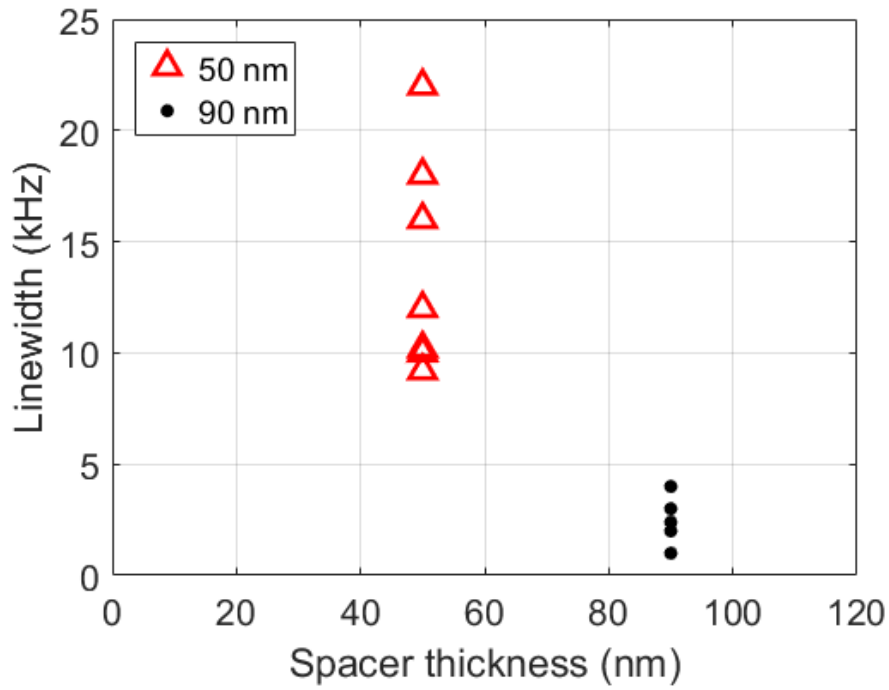


Figure 3.19 Linewidth at the maximum pumping current as a function of the QNCL thickness.

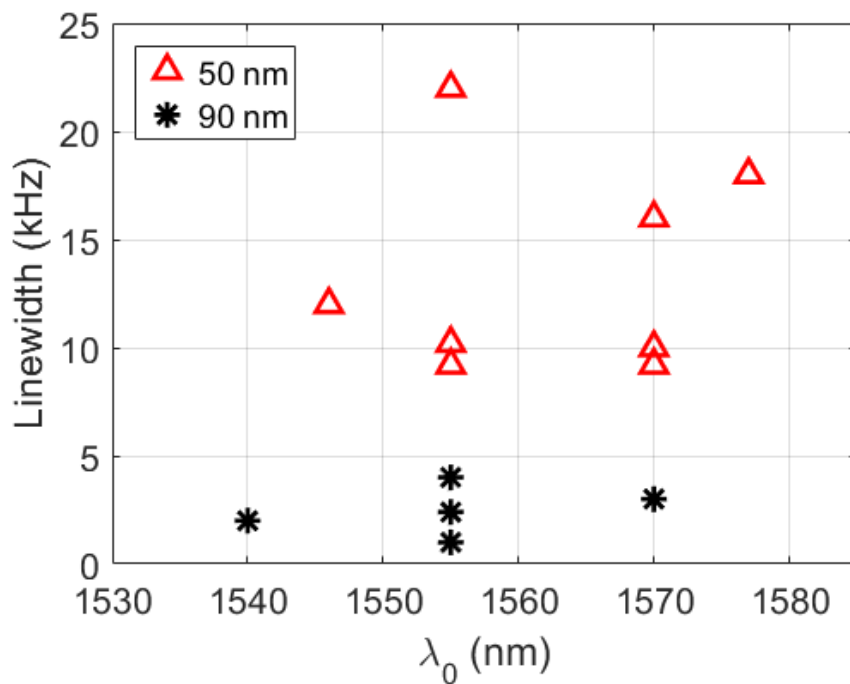


Figure 3.20 Linewidth at the maximum pumping current as a function of the lasing wavelength.

3.4 Discussions and conclusions

In this work, the concept of reducing the phase noise of a laser by decreasing the laser loss is realized through modal engineering in the transverse direction of the waveguide.

The concept has also been realized in the past by increasing the Q-factor of the laser cavity through the modal engineering in the longitudinal direction, a method which includes the use of tapers to transition between regions of high loss and high gain, and regions including only a passive waveguide [49] as well as external cavity laser [50]. In both these architectures, the confinement factor in the active region scales as the ratio of the length of the active region to the effective length of the cavity. This means that reducing the frequency noise by more than an order of magnitude as shown in this chapter would require the size of the external cavity laser to scale by the required reduction in active confinement, yielding devices larger by orders of magnitude.

However, in the lasers described here, small changes in the thickness of the SiO₂ layer on the order of tens of nm can change the confinement factor by orders of magnitude and can alter the linewidth of the laser by orders of magnitude. This transverse modal control allows us to achieve the same effect with very little compromise in footprint. In addition, the thickness of the QNCL can be readily controlled through standard fabrication techniques before patterning, making this technique highly scalable for full wafer fabrication. This strategy can be utilized for any semiconductor lasers by replacing the active region with low-loss resonator, when the modal losses are dominated by the losses in the active region.

This chapter has presented transverse modal engineering as the optimum way to decrease phase noise in lasers by storing most of the light in low-loss resonator rather than lossy active region. Modal engineering has been demonstrated on the heterogeneous Si/III-V platform by introducing a low-index SiO₂ layer between Si and III-V waveguides to push the mode further into low-loss Si and away from the highly-doped III-V active layer. The resulting reduced modal loss in the laser is accompanied by the reduced modal gain, making the threshold current density ideally constant. These lasers are experimentally shown to have narrow linewidths reaching a few kHz Schawlow-Townes linewidths even at a current slightly above threshold.

Chapter 4

DYNAMIC RESPONSE

In Chapter 3, we demonstrated the reduction of frequency noise in our heterogeneous Si/III-V laser through modal engineering in the heterogeneous Si/III-V structure. Here, we investigate the effect of such a design on the modulation response of the lasers. Due to the reduced mode confinement factor in the active layer, we show theoretically and demonstrate experimentally that the lasers possess reduced relaxation resonance frequencies, compared to the conventional III-V semiconductor lasers. At frequencies above the relaxation resonance frequency, carrier modulation due to spontaneous emission is effectively suppressed, diminishing the contribution of carrier number modulation to frequency noise via amplitude-phase coupling. Thus, at a GHz frequency range, it becomes possible to reveal the intrinsic, quantum-limited Schawlow-Townes noise floor, which is due to the direct spontaneous emission into the laser mode. This leads to further reduction of the linewidth.

In this chapter, measurement results of the intensity modulation (IM) response of our lasers are presented. The relaxation resonance frequencies and the frequency modulation (FM) response of lasers with different QNCL thickness are measured. The two are used to obtain the linewidth enhancement factors of the lasers. Lastly, in section 4.6, we update our frequency noise results, presented in section 3.3, by using the measured modulation data to extrapolate the frequency noise of the lasers further into the GHz range, and reveal the intrinsic Schawlow-Townes noise floor of the lasers.

4.1 Differential analysis of the rate equations

To investigate the dynamic modulation response of a laser in response to the perturbation to the laser [26, 24], we employ the photon and carrier number rate equations derived in Section 2.1.4.

$$\frac{dN}{dt} = \eta_i \frac{I}{q} - \frac{N}{\tau} - A'(N - N_{tr})N_p \quad (4.1)$$

$$\frac{dN_p}{dt} = \left[A'(N - N_{tr}) - \frac{1}{\tau_p} \right] N_p, \quad (4.2)$$

where N and N_p are the total number of carriers and photons, η_i is an injection efficiency, τ is the carrier recombination time, τ_p is the photon lifetime. The induced transition rate into the laser mode per electron due to one photon, A' , was written as,

$$A' = W_{sp}^{(l)} = \frac{2\pi^2\mu^2\nu_0}{h\epsilon(\Delta\nu)_a} |\bar{E}_l(\bar{r}_a)|^2, \quad (4.3)$$

where $|E_l(r_a)|^2$ is proportional to the intensity of the modal profile of a single photon in the high-Q resonator at the location of the emitting atoms.

In Equation $\frac{dN_p}{dt} = \left[A'(N - N_{tr}) - \frac{1}{\tau_p} \right] N_p$, (4.2), the contribution of spontaneous emission to the photon number is ignored, since only a small portion of the spontaneously emitted photons couple into the lasing mode.

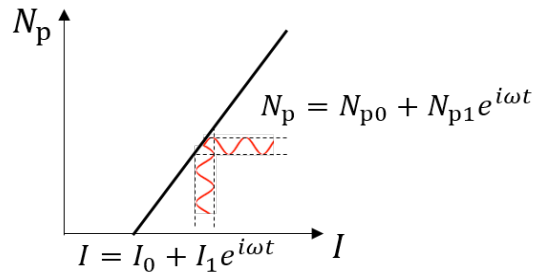


Figure 4.1 Laser small-signal model.

We consider the case in which a laser is biased to operate at a DC current I_0 with a small AC current I_1 of frequency ω superimposed on the DC bias. A laser is a linear time-invariant (LTI) system to a first approximation, so the applied current, carrier number, and photon number can be expressed as,

$$I = I_0 + I_1 e^{i\omega t}, \quad (4.4)$$

$$N = N_0 + N_1 e^{i\omega t}, \quad (4.5)$$

$$N_p = N_{p0} + N_{p1} e^{i\omega t}, \quad (4.6)$$

where N_0 and N_{p0} are the steady-state carrier and photon number.

Using the threshold condition $A'(N_0 - N_{tr}) = 1/\tau_p$, the steady-state solution $0 = \eta_i \frac{I_0}{q} - \frac{N_0}{\tau} - \frac{N_{p0}}{\tau_p}$ can be obtained. Using Equations $I=I_0 + I_1 \square^{i\omega t}$, (4.4-5) and this steady-state solution, we obtain:

$$i\omega N_1 = \eta_i \frac{I_1}{q} - N_1 \left(\frac{1}{\tau} + A'N_{p0} \right) - \frac{N_{p1}}{\tau_p}, \quad (4.7)$$

$$i\omega N_{p1} = A'N_{p0}N_1. \quad (4.8)$$

Then, the modulation response of the photon number N_{p1} to the sinusoidal current modulation I_1 is,

$$\frac{N_{p1}(\omega)}{I_1(\omega)} = \frac{\eta_i A' N_{p0}}{q} \frac{1}{\frac{A' N_{p0}}{\tau_p} - \omega^2 + i\omega \left(A' N_{p0} + \frac{1}{\tau} \right)}. \quad (4.9)$$

The above equation can be rewritten as,

$$\frac{N_{p1}(\omega)}{I_1(\omega)} = \frac{\eta_i \tau_p}{q} H(\omega), \quad (4.10)$$

where the modulation response is described using the modulation transfer function $H(\omega)$,

$$H(\omega) = \frac{\omega_R^2}{\omega_R^2 - \omega^2 + j\omega\gamma}. \quad (4.11)$$

The *relaxation resonance frequency* ω_R and the damping factor γ are given by

$$\omega_R = \sqrt{\frac{A' N_{p0}}{\tau_p}} \quad (4.12)$$

$$\gamma = A' N_{p0} + \frac{1}{\tau}. \quad (4.13)$$

The generated optical power P_1 from the modulating photons N_{p1} can be derived using the ratio of the mirror loss to the total loss $\frac{Q_{\text{ext}}^{-1}}{Q_{\text{ext}}^{-1}+Q_{\text{int}}^{-1}}$ and a photon lifetime τ_p , and is written as $P_1 = \frac{Q_{\text{ext}}^{-1}}{Q_{\text{ext}}^{-1}+Q_{\text{int}}^{-1}} h\nu \frac{N_{p1}}{\tau_p}$. Accordingly, the IM response of the optical output power P_1 to the modulation current I_1 becomes:

$$\frac{P_1(\omega)}{I_1(\omega)} = \eta_d \frac{h\nu}{q} \frac{\omega_R^2}{\omega_R^2 - \omega^2 + i\omega\gamma'} \quad (4.14)$$

with a differential quantum efficiency $\eta_d = \eta_i \frac{Q_{\text{ext}}^{-1}}{Q_{\text{ext}}^{-1}+Q_{\text{int}}^{-1}}$.

We define the IM depth (also called the IM index) as $m = \frac{P_1}{P_0}$. The DC output power P_0 from the photon number N_{p0} can be expressed as $P_0 = \frac{Q_{\text{ext}}^{-1}}{Q_{\text{ext}}^{-1}+Q_{\text{int}}^{-1}} h\nu \frac{N_{p0}}{\tau_p}$. Therefore, the IM depth m per unit modulation current can finally be written as,

$$\frac{m(\omega)}{I_1(\omega)} = \frac{P_1(\omega)/P_0}{I_1(\omega)} = \frac{1}{(I-I_{\text{th}})} \frac{\omega_R^2}{\omega_R^2 - \omega^2 + i\omega\gamma'}. \quad (4.15)$$

This transfer function is essentially that of a 2nd-order low-pass filter response. The magnitude of the transfer function is constant at low frequencies, peaks at frequency ω_R , and then drops steeply at a rate of 40 dB/dec, as shown in Figure 4.2 Illustration of the intensity and frequency modulation depth of a semiconductor laser as a function of modulation frequency. The relaxation resonance frequency ω_R corresponds to a natural resonance frequency of oscillation associated with the coupling between the carriers and the photons.

By using Equation $A' = W_{\text{sp}}^{(l)} = \frac{2\pi^2\mu^2\nu_0}{h\epsilon(\Delta\nu)_a} |\bar{E}_l(\bar{r}_a)|^2$, (4.3) and the steady-state photon number $N_{p0} = \eta_i\tau_p(I - I_{\text{th}})/q$ (Equation $N_{p0} = \frac{\eta_i}{g_{\text{th}}} \frac{I - I_{\text{th}}}{q} = \eta_i\tau_p \frac{I - I_{\text{th}}}{q} = \eta_i \frac{Q}{\omega} \frac{I - I_{\text{th}}}{q}$.(2.23)), the relaxation resonance frequency in Equation $\omega_R = \sqrt{\frac{A'N_{p0}}{\tau_p}}$ (4.12) can be written as,

$$\omega_R = \sqrt{\eta_i \frac{A'}{q} (I - I_{\text{th}})} = \sqrt{\frac{2\pi^2\mu^2\nu_0}{h\epsilon(\Delta\nu)_a} \eta_i (I - I_{\text{th}}) |\bar{E}_l(\bar{r}_a)|}. \quad (4.16)$$

The relaxation resonance frequency determines the direct modulation bandwidth $\omega_{3\text{dB}}$, which $\omega_R = \eta_i A' q (I - I_{\text{th}}) = 2\pi \mu_0 h \epsilon \Delta v a \eta_i (I - I_{\text{th}}) E l r a$. (4.16) describes the relaxation resonance frequency's square root dependence on the offset current above threshold $(I - I_{\text{th}})$ and the linear dependence on $|E_l(\tau_a)|$.

We now study the response of the carriers to the modulation current. The small-signal response of the carrier number to the injection current $N_1(\omega)/I_1(\omega)$ is written as,

$$\frac{N_1(\omega)}{I_1(\omega)} = \frac{\eta_i}{q} \frac{i\omega}{\omega_R^2 - \omega^2 + i\omega\gamma}. \quad (4.17)$$

The carrier number modulation caused by the current modulation also leads to refractive index modulation in the active region through the plasma dispersion effect, and results in frequency modulation. The amount of frequency modulation $\Delta\nu$ is related to the amount of the carrier density modulation through the linewidth enhancement factor [26, p. 706],

$$\Delta\nu = \frac{\alpha}{4\pi} \Gamma_a v_g a \frac{\Delta N}{v_a}. \quad (4.18)$$

Using Equation $\frac{N_1(\omega)}{I_1(\omega)} = \frac{\eta_i}{q} \frac{i\omega}{\omega_R^2 - \omega^2 + i\omega\gamma}$. (4.17), we obtain the frequency modulation response of the modulation frequency ν_1 to a sinusoidal modulation current I_1 ,

$$\frac{\nu_1(\omega)}{I_1(\omega)} = \frac{\alpha}{4\pi} \Gamma_a v_g a \frac{\eta_i}{q} \frac{i\omega}{\omega_R^2 - \omega^2 + i\omega\gamma}. \quad (4.19)$$

We define the FM depth (also called the FM index), as $M = \frac{\nu_1}{f}$. Replacing Equation $\frac{\nu_1(\omega)}{I_1(\omega)} = \frac{\alpha}{4\pi} \Gamma_a v_g a \frac{\eta_i}{q} \frac{i\omega}{\omega_R^2 - \omega^2 + i\omega\gamma}$. (4.19) with $\omega_R = \sqrt{\frac{\Gamma_a v_g a N_{p0}}{\tau_p}}$ and $N_{p0} = \eta_i \tau_p \frac{I - I_{\text{th}}}{q}$ yields the FM depth per unit modulation current,

$$\frac{M(\omega)}{I_1(\omega)} = \frac{\nu_1(\omega)/f}{I_1(\omega)} = \frac{\alpha}{2(I - I_{\text{th}})} \frac{\omega_R^2}{\omega_R^2 - \omega^2 + i\omega\gamma}. \quad (4.20)$$

Figure 4.2 describes the typical behavior of the IM and FM response of semiconductor lasers. Both the IM and the FM indices show peaks at the relaxation resonance frequency, and falls off steeply above the relaxation resonance frequency with a slope of 40 dB/dec.

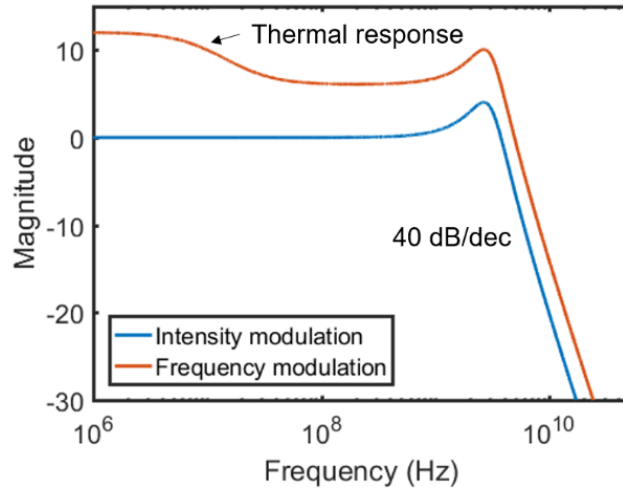


Figure 4.2 Illustration of the intensity and frequency modulation depth of a semiconductor laser as a function of modulation frequency. For the FM depth, both temperature and carrier effects are included.

At low modulation frequencies, the FM response includes another source of the frequency modulation, which is caused by the temperature fluctuations due to the modulating current. Through the thermo-optic coefficient, the temperature variations cause the frequency of the laser to change independently from the linewidth enhancement factor. To isolate the carrier modulation effect from the thermal effect, we must compare the IM and FM at GHz frequencies where temperature fluctuations can be ignored. In this regime, the linewidth enhancement factor is related to the IM and the FM depth, and can be obtained from the ratio between Equation $\frac{m(\omega)}{I_1(\omega)} =$

$$\frac{P_1(\omega)/P_0}{I_1(\omega)} = \frac{1}{(I-I_{th})} \frac{\omega_R^2}{\omega_R^2 - \omega^2 + i\omega\gamma}. \quad (4.15) \quad \text{and} \quad \frac{M(\omega)}{I_1(\omega)} = \frac{\nu_1(\omega)/f}{I_1(\omega)} = \frac{\alpha}{2(I-I_{th})} \frac{\omega_R^2}{\omega_R^2 - \omega^2 + i\omega\gamma}. \quad (4.20),$$

$$\alpha = \frac{M}{m/2}.$$

4.2 The linewidth enhancement factor revisited

In Section 2.2.2, the linewidth enhancement factor was introduced to account for additional linewidth broadening, which arises from the refractive index fluctuations due to the carrier density fluctuations during the spontaneous emission events. However, the spectral dependence of the carrier density fluctuations and their effect on the frequency noise power spectral density were not considered.

In [27, 28], Vahala described the noise spectrum of a laser in the quantum-limited regime and showed that the effect of the linewidth enhancement factor α follows the same spectral dependence as the IM response of a laser $H(\omega)$ by including the carrier density as a dynamical variable. Therefore, the frequency noise arising from the carrier fluctuations during the spontaneous emission events shows $(\alpha|H(\omega)|)^2$ spectral dependence, where $|H(\omega)|$ is the modulation transfer function of the laser, previously discussed in Section 4.1. Thus, the frequency noise PSD of semiconductor lasers can finally be written as,

$$S_{\Delta\nu}(\omega) = \frac{R_{\text{sp}}^{(l)}}{4\pi^2 N_p} (1 + \alpha^2 |H(\omega)|^2). \quad (4.21)$$

The above equation demonstrates that in a FM noise spectrum, the carrier modulation-induced noise ($\frac{R_{\text{sp}}^{(l)}}{4\pi^2 N_p} \alpha^2$) becomes negligible at frequencies above the relaxation resonance frequency and the total frequency noise reduces to the white noise floor generated only by the spontaneous emission phase noise ($\frac{R_{\text{sp}}^{(l)}}{4\pi^2 N_p}$).

Various techniques to measure the linewidth enhancement factor have been reported. They include linewidth-based measurement [51, 52, 53], modulation-based estimation [54, 55], injection-locking based [56, 57], and optical feedback self-mixing based [58, 59, 60] estimation. These different approaches are summarized and compared in [61]. For our lasers, we choose to use the modulation-based method, which takes the ratio of the FM and IM depth in a direct-modulating state [62], as described in the previous section. This method allows for the direct observation of the IM and FM response, and the linewidth enhancement factor of the lasers at the same time.

4.3 Suppression of the influence of the linewidth enhancement factor in QNCL

Based on the analysis performed in the previous section, we now investigate the dynamic modulation response of our high-coherence Si/InP lasers.

In the on-off keying (OOK) or intensity-modulated/direct-detection (IMDD) systems, it is desirable for a solitary laser device to possess large relaxation resonance frequencies to achieve a high modulation bandwidth. Lasers with relaxation resonance frequencies in the tens of GHz have been demonstrated by reducing the damping of the resonance peak, reducing contact parasitic or improving the diffusion-limited carrier transport into the active region. A modulation bandwidth (f_{3dB}) of more than 25 GHz in VCSEL [63] and larger than 30 GHz in DFB lasers has been reported [64, 65, 66, 67].

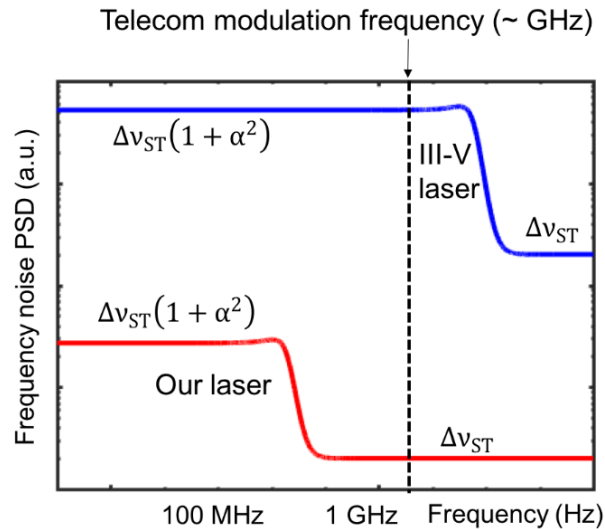


Figure 4.3 Expected frequency noise PSD of QNCL laser and conventional III-V laser. In our high-coherence Si/III-V lasers, due to reduction of the confinement factor in the active region, decrease in the relaxation resonance frequency compared to III-V only laser is expected. Due to suppression of the effect of the linewidth enhancement factor above the relaxation resonance frequency, we expect to see even further reduced noise frequency at the frequency range of a few GHz (i.e., optical telecommunication frequency).

On the other hand, in coherent communication, information is encoded in the phase of the field in addition to the intensity, and direct modulation is replaced by external modulators. Therefore, it is beneficial to decrease the relaxation resonance frequency of the laser to below the data

modulation frequencies to suppress the additional phase noise resulting from carrier density fluctuations at telecommunication relevant frequencies (few to tens of GHz).

In our high-coherence Si/InP lasers, the normalized field at the active QW layer, $|\bar{E}_l(\bar{r}_a)|$, is reduced drastically in the process of reducing the modal loss in the laser cavity. Due to the relaxation resonance frequency's $|E_l(r_a)|$ dependence (Equation $\omega_R = \sqrt{\eta_i \frac{A'}{q} (I - I_{th})} = \sqrt{\frac{2\pi^2 \mu^2 v_0}{h\epsilon(\Delta v)_a} \eta_i (I - I_{th})} |\bar{E}_l(\bar{r}_a)|$. (4.16)), we can expect this design to yield a lower relaxation resonance frequency by one or two orders of magnitude, compared to conventional III-V semiconductor lasers.

Figure 4.3 illustrates that at frequencies of a few GHz (the frequencies of interest in optical telecommunication), the conventional III-V lasers still exhibit the “enhanced” frequency noise including the carrier modulation-induced frequency noise. In comparison, at the same frequencies, our high-coherence lasers are predicted to exhibit a frequency noise due to direct spontaneous emission phase noise only. This is due to the suppression of the influence of the linewidth enhancement factors at relatively low frequencies. Thus, we expect our lasers with their reduced linewidths down to a few to tens of kHz, to possess a frequency noise spectral density corresponding to a sub-kHz Schawlow-Townes linewidth at frequencies of a few GHz.

In the remainder of this chapter, we present the measured IM and FM response of our lasers. The relaxation resonance frequencies from lasers with different QNCL thicknesses are measured and compared. We also revisit our frequency noise measurements presented in Section 3.3, and extrapolate the frequency noise further into a GHz range, revealing the intrinsic Schawlow-Townes noise floor of the lasers.

4.4 Intensity modulation response of the heterogeneous laser

4.4.1 Measurement setup

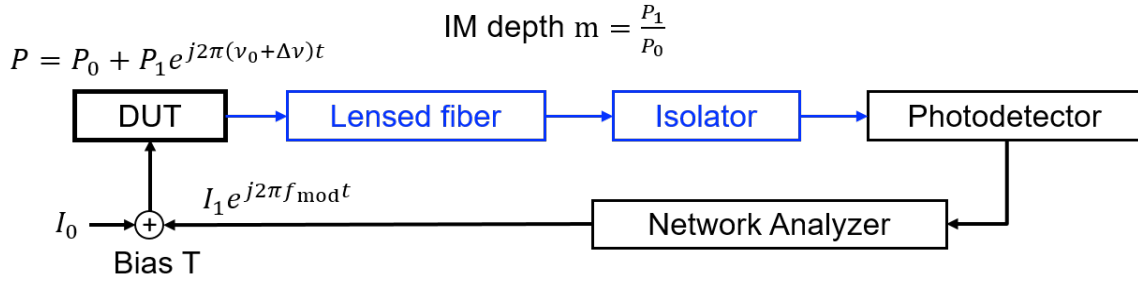


Figure 4.4 Intensity modulation measurement setup.

Figure 4.4 presents the IM measurement setup. A bias tee (ZFBT-6GW, 0.1-6000MHz) is used to combine the DC and the high-frequencies. An ultra-low noise laser diode driver (LDX-3620) is connected to the DC port of the bias tee and used to bias the laser above threshold. The high-frequency signal available from the output port of the network analyzer (NA) is connected to the RF port of the bias tee. The set-point power for the NA is set to apply i_1 of 2 mA for a modulation power $P_{\text{mod}} = i_1^2 R_{\text{laser}}/2$ to the laser. The combined DC and high-frequency signal is routed to the laser probe (Picoprobe ACP40-GSG-100, max frequency: 40 GHz). The laser light, collected through the lensed fiber (tapered PM fiber with AR coated, TPMJ-3A-1550-8/125-0.25-5-2-12-0.5-AR), is directly fed into one port of a fast-balanced PD (Optilab BPR-20-M). The PD generates voltage in the form of,

$$V(t) = V_0 + V_1 \sin(\omega_m t) = V_0(1 + m \sin(\omega_m t)), \quad (4.22)$$

where m is the IM depth discussed in Section 4.1. Therefore, the IM depth m can be extracted as,

$$m = \frac{V_1}{V_0}. \quad (4.23)$$

The output of the PD is routed to the return port of the NA to measure the forward transmission coefficient $S_{21}(\omega)$. The DC voltage V_0 is calculated from the optical power measured on the PD and the responsivity (V/W) of the PD (R_{PD}). The responsivity is characterized prior to conducting the experiment by passing the fast frequency chirping laser [47] and varying the laser output power. An Agilent 4395A network analyzer is used to measure the low-frequency range from 10 Hz to

500 MHz, and another network analyzer HP 8722 C is used to measure the high-frequency range from 50 MHz to 40 GHz. The peak amplitude of the AC signal, V_1 , can be calculated using the measured S_{21} and input average power P_{mod} ,

$$V_1(\omega) = \sqrt{2R_{\text{PD}}[P_{\text{mod}}S_{21}(\omega)]} = \sqrt{R_{\text{PD}}[i_1^2 R_{\text{laser}} S_{21}(\omega)]}. \quad (4.24)$$

Corrections are made to the measured data to compensate for the response of the driving circuitry (including bias tee, probe tip, SMA coax cable), measured prior to the experiment. The same number of the cables as in the laser modulation configuration is used.

4.4.2 Experimental results

Figure 4.5 illustrates the IM response of the laser with the 50 nm QNCL ($I_{\text{th}} = 55$ mA) at bias currents of 70, 90, and 130 mA. As expected, the IM response displays a 2nd-order low-pass filter behavior with a flat response for frequencies up to the relaxation resonance frequencies, and 40 dB/dec drop-off thereafter. The relaxation resonance frequency increases with increasing bias current. Fitting the measured response to the 2nd-order low-pass filter response in Equation

$$H(\omega) = \frac{\omega_{\text{R}}^2}{\omega_{\text{R}}^2 - \omega^2 + j\omega\gamma}. \quad (4.11)$$

yields a relaxation resonance frequencies of 380, 650, and 900 MHz at the bias currents of 70, 90, and 130 mA, respectively. The 3 dB modulation bandwidth can be obtained from the relaxation resonance frequencies through the relationship $\omega_{3\text{dB}} = (\sqrt{1 + \sqrt{2}}) \cdot \omega_{\text{R}}$ [24, p. 265]. The 3 dB modulation bandwidth $\omega_{3\text{dB}}$ of 590 MHz, 1 GHz, and 1.4 GHz is obtained at 70, 90, and 130 mA.

Figure 4.6 shows the IM modulation response of the laser with 90 nm QNCL ($I_{\text{th}} = 65$ mA) at bias currents of 100, 140, and 170 mA. The larger number of photons in the lasing mode in the 90 nm QNCL laser than in the 50 nm laser makes the damping in the 90 nm laser larger, and thus the relaxation resonance less apparent than in the 50 nm laser. Fitting the measured curves to the 2nd-order low-pass filter response yields relaxation resonance frequencies of 320, 540, and 610 MHz at 100, 140, and 170 mA, respectively.

In Figure 4.7, we plot the IM response of the lasers from the 50, 90, and 130 nm QNCL all $\omega_{\text{R}} = \eta_i A' q I - I_{\text{th}} = 2\pi \mu 2\nu 0 h \epsilon \Delta \nu a \eta_i (I - I_{\text{th}}) E l r a$. (4.16), the relaxation resonance frequency occurs at lower frequencies, as the QW confinement factor decreases with the thicker QNCL

thickness. The lasers show relaxation resonance frequencies of 200, 500 MHz, and 1 GHz at the increment of 80 mA above their respective threshold in the 50, 90, and 130 nm QNCL laser, respectively. These low relaxation resonance frequencies stand in contrast to those of conventional III-V lasers of tens of GHz.

Figure 4.8 shows the linear dependence of the relaxation resonance frequencies of the laser on $\sqrt{I - I_{\text{th}}}$. The relaxation resonance frequencies fall below 1 GHz even for bias current 100 mA above threshold. The reduction in the relaxation resonance frequencies with the increasing QNCL thickness is evident.

The difference between the QW confinement factor in the 50 and 90 nm QNCL lasers can be extracted from the slopes in Figure 4.8. The slope of the 50 nm QNCL laser is larger than that of the 90 nm laser by a factor of 1.77. Considering the $\sqrt{\Gamma_a}$ dependence of the relaxation resonance frequency (Equation $\omega_R = \sqrt{\eta_i \frac{A'}{q} (I - I_{\text{th}})} = \sqrt{\frac{2\pi^2 \mu^2 v_0}{h\epsilon(\Delta v)_a} \eta_i (I - I_{\text{th}}) |\bar{E}_l(\bar{r}_a)|}$ (4.16)), the 50 nm laser has a larger Γ_a than the 90 nm laser by a factor of $1.8^2 = 3.24$. This number matches our simulation result, which yielded a Γ_a of 2% and 0.6% for the 50 and 90 nm lasers, respectively (as described in Figure 2.3 SiO₂ layer, which we call the “quantum noise control layer (QNCL)”, is introduced in between Si and III-V to further push the mode into the Si layer and reduce the confinement factor in the active region (QWs). (Top figures) The peak of the transverse mode profile stays further away from III-V (i.e., reduced $|\bar{E}_l(\bar{r}_a)|^2$), and the confinement factor in the QWs decreases with thicker QNCL thickness. (Bottom figures) COMSOL simulation showing the transverse mode profile with varying QNCL thickness.

The damping factor γ is also extracted from the fitting of the IM response to the 2nd-order low-pass filter. The K-factor, the slope of the linear fits of γ vs. f_R^2 in Figure 4.9, is found to be 0.5 ns and 1.3 ns for the 50 nm and 90 nm QNCL lasers, respectively. The large K-factors, compared to III-V only lasers [68], reflect the increased photon lifetime in our lasers [24, p. 264].

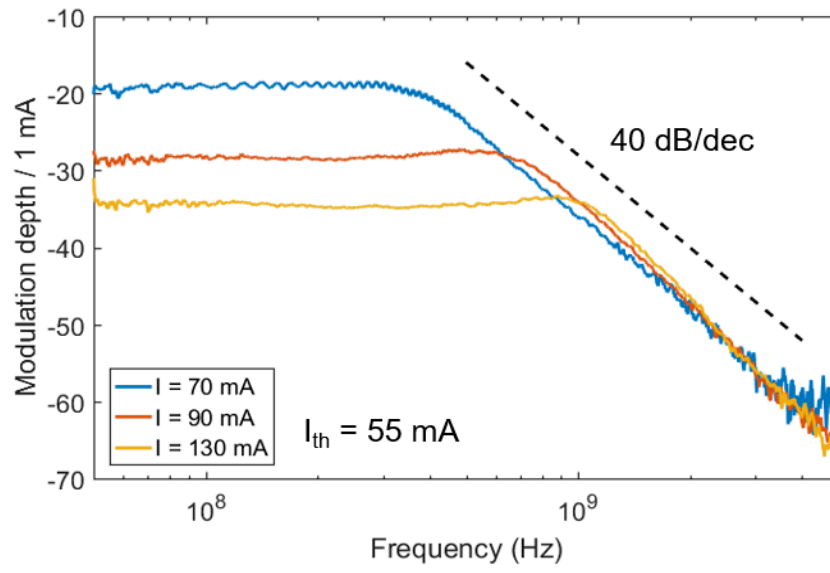


Figure 4.5 IM response of the 50 nm QNCL laser at different bias currents (device ID: hQsp6 ch01 slot2 bar6 dev5).

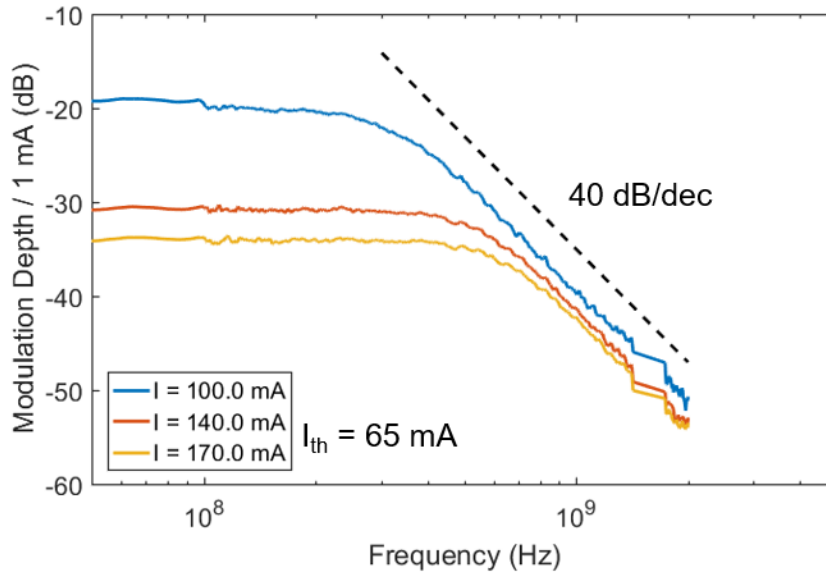


Figure 4.6 IM response of the 90 nm QNCL laser at different bias currents (device ID: hQsp7 ch09 slot1 bar4 dev9).

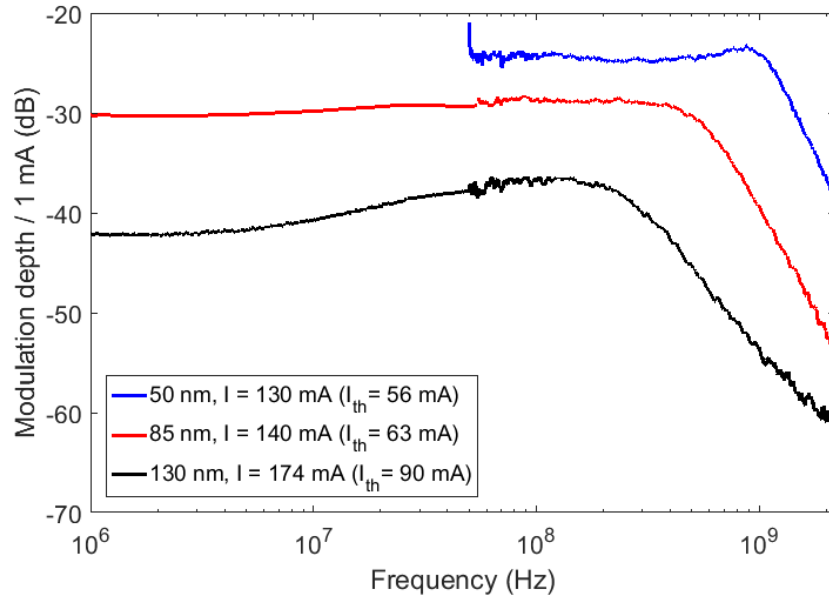


Figure 4.7 IM response of the 50, 90, and 130 nm QNCL lasers at the similar bias current above each threshold.

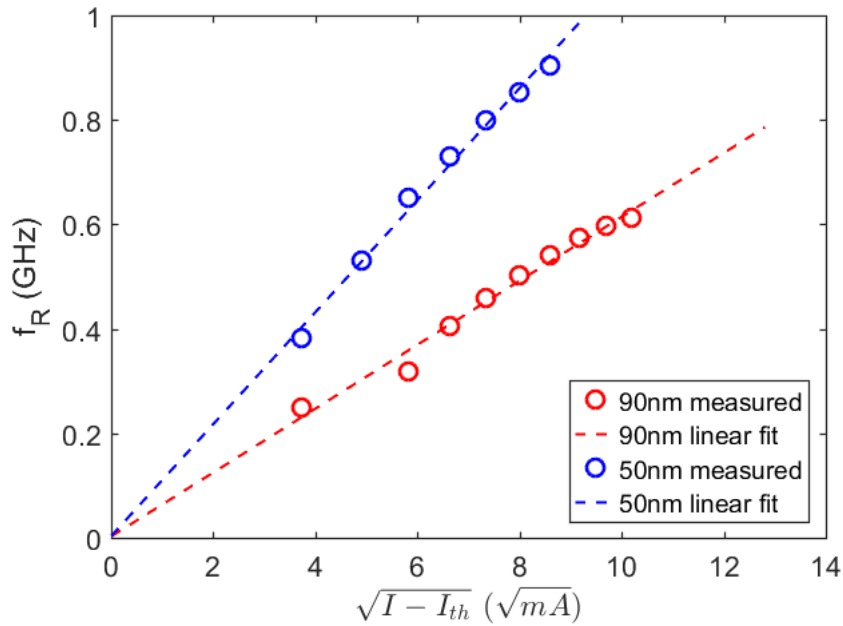


Figure 4.8 Relaxation resonance frequencies of the 50 nm and 90 nm QNCL lasers as a function of $\sqrt{I - I_{th}}$.

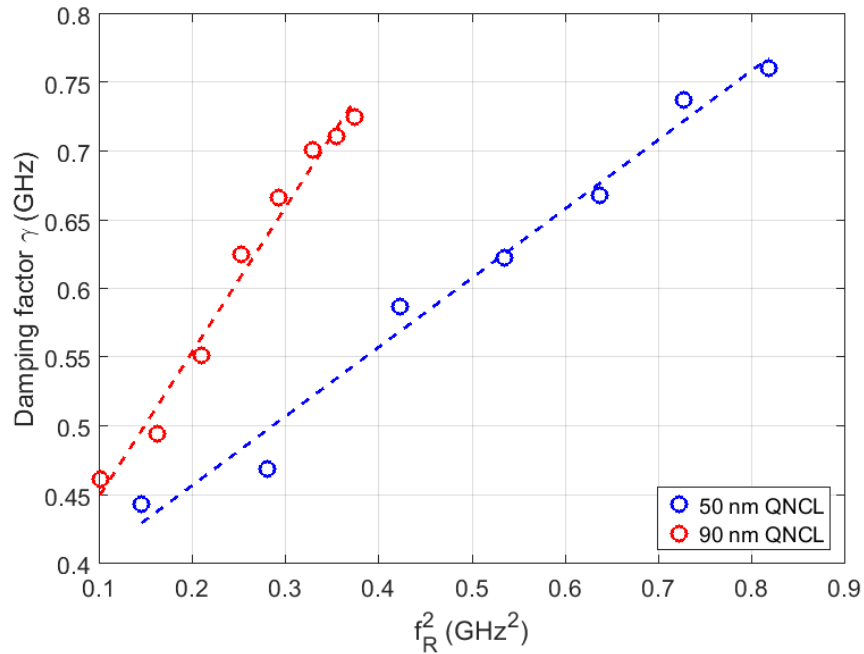


Figure 4.9 Dependence of damping factor of the Si/III-V lasers on the relaxation resonance frequency.

4.5 Frequency modulation response and linewidth enhancement factor

4.5.1 Measurement setup

The FM response is measured using the setup shown in Figure 4.10. Except for an additional MZI path, the same setup is used as in the IM setup. As discussed for the frequency noise measurement setup, an MZI serves as a frequency discriminator by converting phase modulation into intensity modulation.

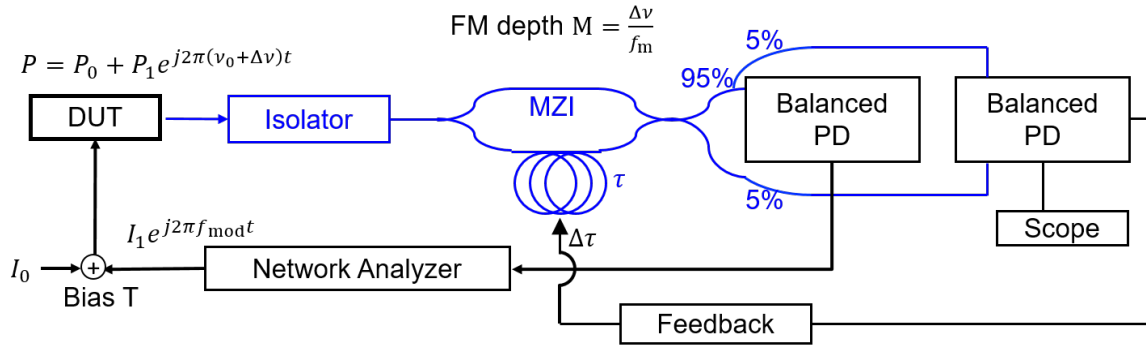


Figure 4.10 Frequency modulation measurement setup.

The high-frequency signal generated from the output port of the network analyzer (NA) is connected to the RF port of the bias tee, whereas the bias current is provided by the ultra-low noise laser diode driver (LDX-3620). The set-point power for the NA is set to apply i_1 of 2 mA for a modulation power of $P_{\text{mod}} = i_1^2 R_{\text{laser}}/2$ to the laser.

Laser light, collected through the lensed fiber (tapered PM fiber with AR coated, TPMJ-3A-1550-8/125-0.25-5-2-12-0.5-AR), is passed through the MZI with an FSR of 1.575 GHz. The length of one of the arms of the MZI is controlled using a fiber stretcher piezo (Evanscent Optics 915B). The piezo is used to lock the phase difference between the two MZI arms at the quadrature point.

The two outputs of the MZI are connected to a pair of couplers that couple 5% of the light to a slow balanced PD (New Focus 1817, DC \sim 80MHz), and the other 95% to a fast PD (Optilab BPR-20-M). The slow balanced PD is connected to an electronic feedback circuit. The output of the feedback circuit is fed to an MZI piezo driver (Evanscent Optics 914-2) and closes the feedback circuit.

The output of the fast PD is routed to the return port of the NA to measure the forward transmission coefficient $S_{21}(f_m)$. The Agilent 4395A network analyzer is used to measure the low-frequency range from 10 Hz to 500 MHz, and another network analyzer HP 8722 C is used to measure the high-frequency range from 50 MHz to 40 GHz. The same method as in the IM response is used to measure the DC voltage V_0 and the peak amplitude of the AC voltage V_1 .

The laser's frequency chirp due to the modulation current can be extracted from the measured AC signal V_1 as follows. When the interferometer is locked at the quadrature ($\omega_0\tau = \pi/2$) and the

phase modulation is small enough, the PD voltage generated is proportional to the phase difference between the two MZI arms $\Delta\theta(t, \tau) = \theta(t) - \theta(t - \tau)$,

$$V_1(t) = V_g[\theta(t) - \theta(t - \tau)], \quad (4.25)$$

where V_g is a voltage gain conversion factor.

The Fourier component at each frequency is extracted by taking the Fourier transform of the above equation,

$$\begin{aligned} \hat{V}_1(\omega) &= V_g \hat{\theta}(\omega)(1 - e^{i\omega\tau}) \\ &= 2iV_g \hat{\theta}(\omega) e^{i\pi\tau} \sin(\omega\tau/2) \\ &= iV_g \omega\tau \hat{\theta}(\omega) e^{i\omega\tau/2} \text{sinc}(\omega\tau/2). \end{aligned} \quad (4.26)$$

Using $1/\tau = \text{FSR}$ and $\Delta\nu = \frac{1}{2\pi} \frac{d\theta}{dt} \leftrightarrow \Delta\hat{\nu}(\omega) = \frac{1}{2\pi} i\omega \hat{\theta}(\omega)$, the frequency modulation index $M = \frac{|\Delta\hat{\nu}(\omega)|}{f}$ can be obtained from the measured V_0 and V_1 ,

$$M = \frac{|\Delta\hat{\nu}(\omega)|}{f} = \frac{\text{FSR}}{2\pi f \text{sinc}(\omega/2\text{FSR})} \frac{|\hat{V}_1(\omega)|}{V_g}. \quad (4.27)$$

By placing the polarization controllers after the isolators and in one of the MZI arms, an interferometer fringe visibility value of 1 is achieved. This allow us to use the measured DC voltage V_0 as the voltage gain conversion factor V_g (i.e., $V_g = V_0$). In addition, corrections to the measured data are made to compensate for the response of the driving circuitry (including bias tee, probe tip, and SMA coax cable) which is measured prior to conducting the experiment. The same number of cables in the laser modulation configuration is used.

4.5.2 Experimental results

Figure 4.11 illustrates the FM response of the 50 nm QNCL laser ($I_{\text{th}} = 55$ mA, $\lambda_0 = 1577$ nm) together with its IM response at a bias current of 130 mA. Both the IM and FM depth exhibits the 2nd-order low-pass filter response, where the response is flat up to the relaxation resonance

frequency and then drops steeply. The FM modulation response also shows a peak at the same relaxation resonance frequency of 900 MHz, as does the IM response.

At low modulation frequencies, the FM response exhibits an additional modulation contribution from the thermal effect, as described in Section 4.1. The cut-off frequency for the thermal response is approximately 60 MHz. Compared to a conventional III-V laser, which has a thermal cut-off frequency in the few hundred kHz range, our laser shows a high thermal cut-off frequency. This can probably be attributed to the thermal time constant being inversely proportional to the thermal conductivity. Due to the relatively high thermal conductivity of Si (149 W/(m·K)) compared to InP (68 W/(m·K)), Si possesses a smaller thermal time constant than InP at a given surface area and volume, explaining the fast thermal response of our Si-based laser.

The ratio between the FM and IM depth is used to extract the linewidth enhancement factor α of this laser. The ratio between the IM and FM depth of the 50 nm QNCL laser is shown in Figure 4.12. In the frequency region below 1 GHz, the larger current has a larger value of the ratio, due to the residual thermal frequency modulation effect. Above 1 GHz past the relaxation resonance frequency, the thermal response is heavily suppressed, and only the carrier modulation effect remains in the lasers. The ratios converge to the value of ~ 5.8 , regardless of the bias current level.

Figure 4.13 describes the IM and FM depth of the 90 nm QNCL laser ($I_{th} = 65$ mA, $\lambda_0 = 1556$ nm) at the bias current of 120 mA. Both responses are maximized at the same relaxation resonance frequency of 450 MHz.

Figure 4.14 presents the calculated ratio between the IM and FM depth of the 90 nm QNCL laser. At approximately 1 GHz, the linewidth enhancement factor converges to the value of approximately 3 at all bias currents.

Finally, we observe that the 50 nm QNCL laser, which has a lasing wavelength of 1577 nm, shows a linewidth enhancement factor of 5.8, whereas the 90 nm laser lasing at the wavelength of 1556 nm has a linewidth enhancement factor of 3. As discussed in [30, 69], an increase in the linewidth enhancement factor is observed, as the lasing wavelength is blue-detuned from the differential gain peak.

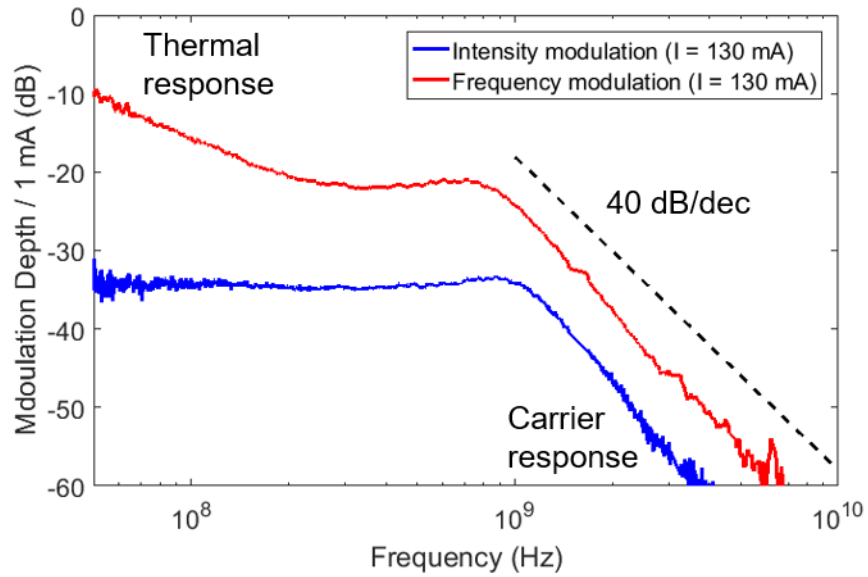


Figure 4.11 The IM and FM response of the 50 nm QNCL laser at the bias current of 130 mA ($I_{th} = 55$ mA, device ID: hQsp6 ch01 slot2 bar6 dev5).

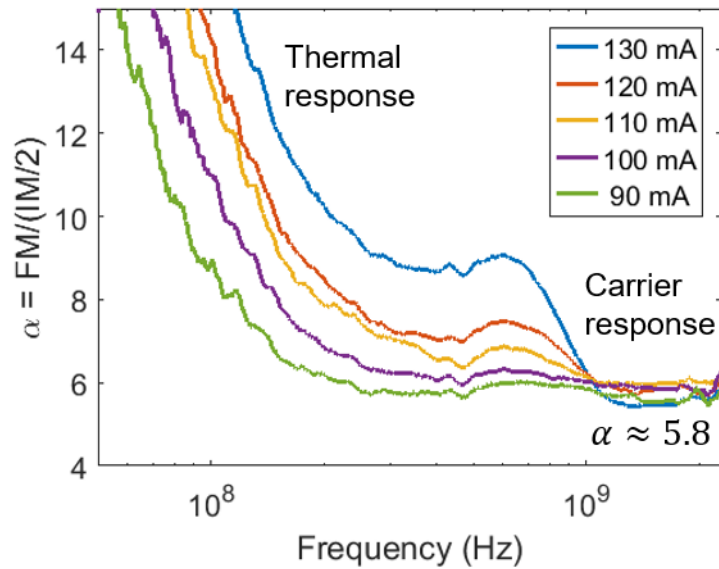


Figure 4.12 Linewidth enhancement factor calculation for the 50 nm QNCL laser.

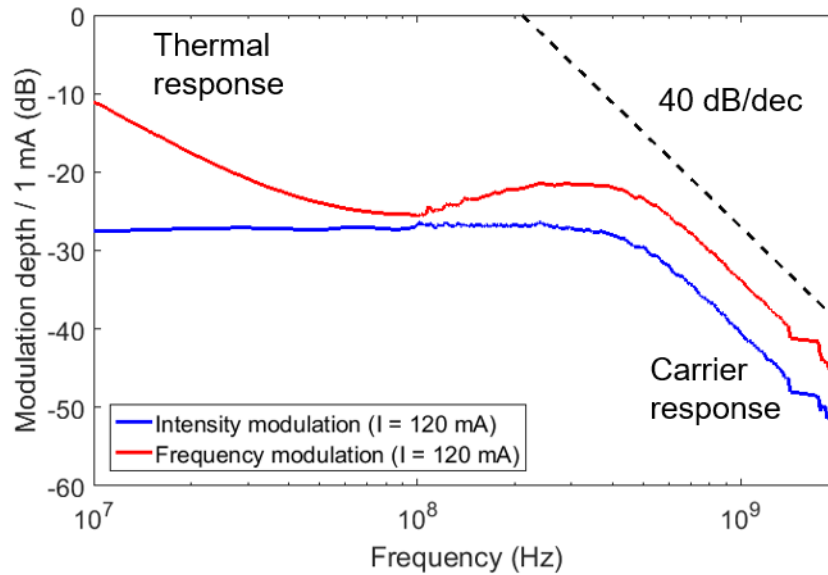


Figure 4.13 The IM and FM response of the 90 nm QNCL laser at the bias current of 130 mA ($I_{th} = 65$ mA, device ID: hQsp7 ch09 slot1 bar4 dev9).

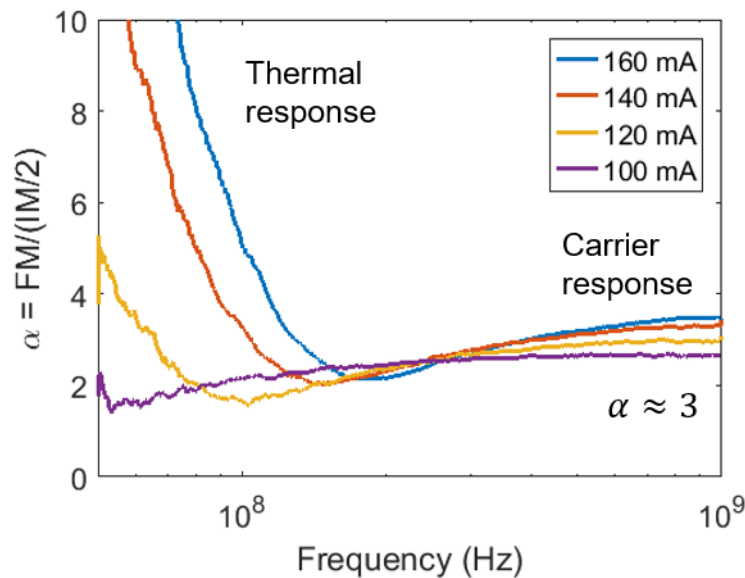


Figure 4.14 Linewidth enhancement factor calculation for the 90 nm QNCL laser.

4.6 Frequency noise above relaxation resonance frequency

As discussed in Section 4.2, due to the spectral dependence of the carrier fluctuation, the effect of linewidth enhancement factor decreases rapidly beyond the relaxation resonance frequency. In this frequency range, the frequency noise caused by the carrier fluctuations is heavily suppressed,

and the total frequency noise reduces to the white noise floor generated only by the spontaneous emission phase noise.

A direct measurement of the spontaneous emission white noise floor is desirable. However, the limited output power of our lasers made their frequency noise approach the shot-noise level at approximately 1 GHz. As a consequence, it was not possible to measure the frequency noise above the relaxation resonance frequency. Instead, we extrapolate the expected frequency noise of lasers, $\Delta\nu_{ST}(1 + \alpha^2|H(f)|^2)$, based on the measured modulation response and the linewidth enhancement factor.

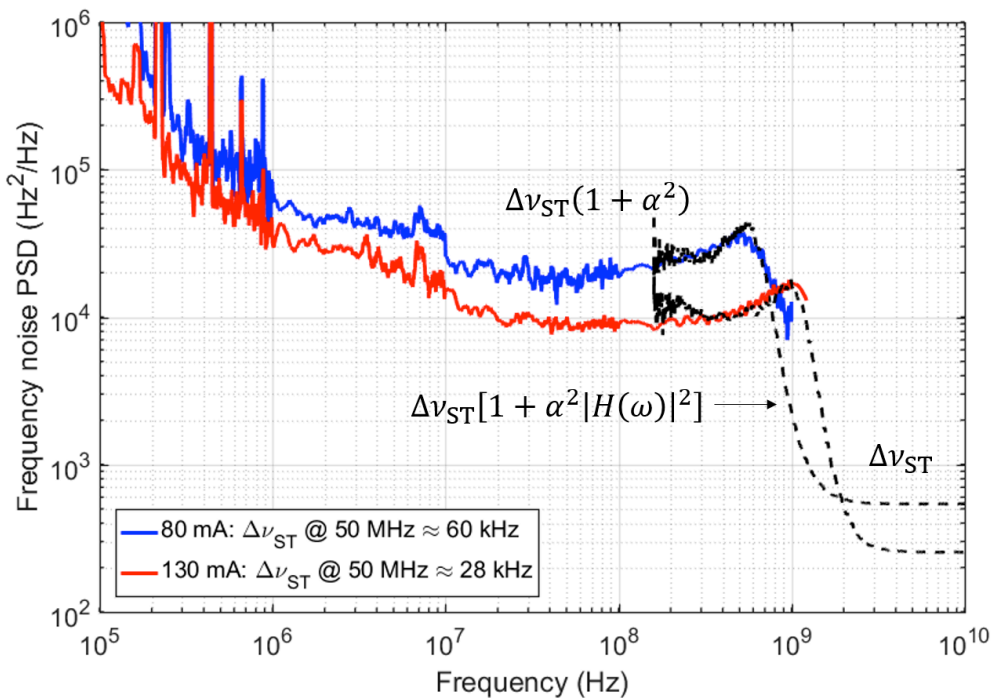


Figure 4.15 shows the frequency noise PSD of the 50 nm QNCL laser ($I_{th} = 55$ mA, $\lambda_0 = 1577$ nm), together with the extrapolated line at the bias current of 80 and 130 mA. The linewidth enhancement factor of 5.8 (Figure 4.12) was used for the extrapolated line. The measured and extrapolated curves at both currents are in good agreement up to 1.25 GHz, at which point the frequency noise PSD becomes shot-noise limited. The extrapolated frequency noise curve exhibits the same relaxation resonance frequency at 530 MHz (80 mA) and 900 MHz (130 mA) as that in the directly measured frequency noise spectrum.

Consequently, we predict that the frequency noise, measured to be 1.9×10^4 Hz²/Hz below the relaxation resonance frequency at a bias current of 80 mA, will drop to 540 Hz²/Hz at a few GHz,

yielding a Schawlow-Townes linewidth of 1.7 kHz. At a bias current of 130 mA, the frequency noise $8.9 \times 10^3 \text{ Hz}^2/\text{Hz}$ (Schawlow-Townes linewidth: 28 kHz) below the relaxation resonance frequency is expected to decrease to $250 \text{ Hz}^2/\text{Hz}$ (Schawlow-Townes linewidth: 0.8 kHz).

Figure 4.16 presents the relaxation resonance frequencies of the 50 nm QNCL laser at various bias currents, measured by two different methods. The two curves, one from the frequency noise measurement and the other from the IM measurement, show a good agreement with each other, displaying the $\sqrt{I - I_{\text{th}}}$ dependence of the relaxation resonance frequency.

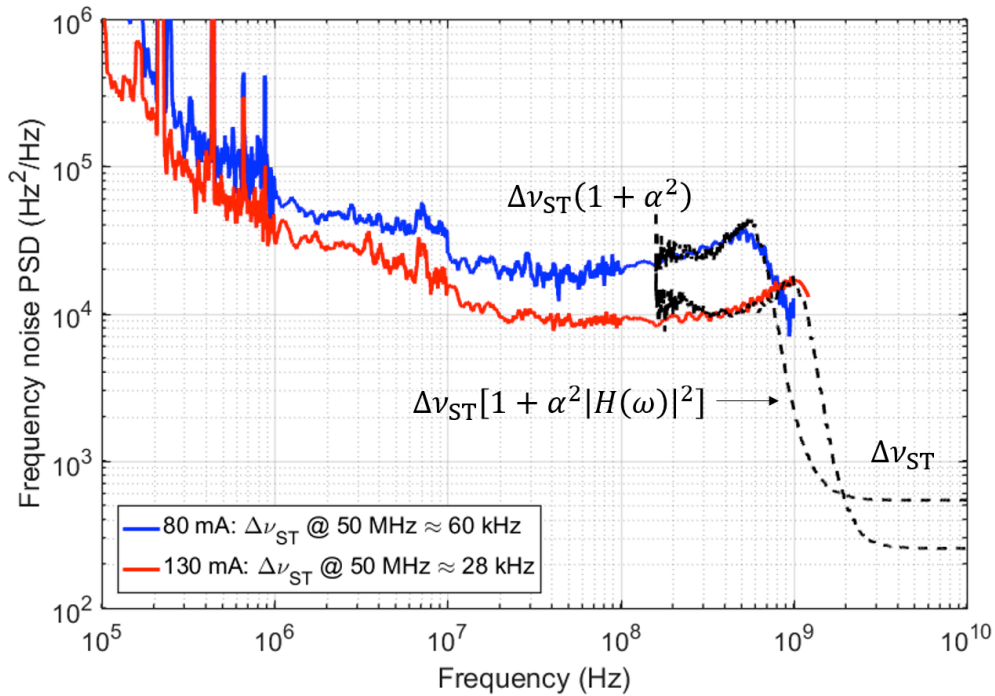


Figure 4.15 Frequency noise PSD for the 50 nm QNCL laser ($I_{th} = 55$ mA, $\lambda_0 = 1577$ nm, $\alpha = 5.8$, device ID: hQsp6 ch01 slot2 bar6 dev5). The extrapolated line for $\Delta\nu_{ST}(1 + \alpha^2|H(\omega)|^2)$ is overlaid.

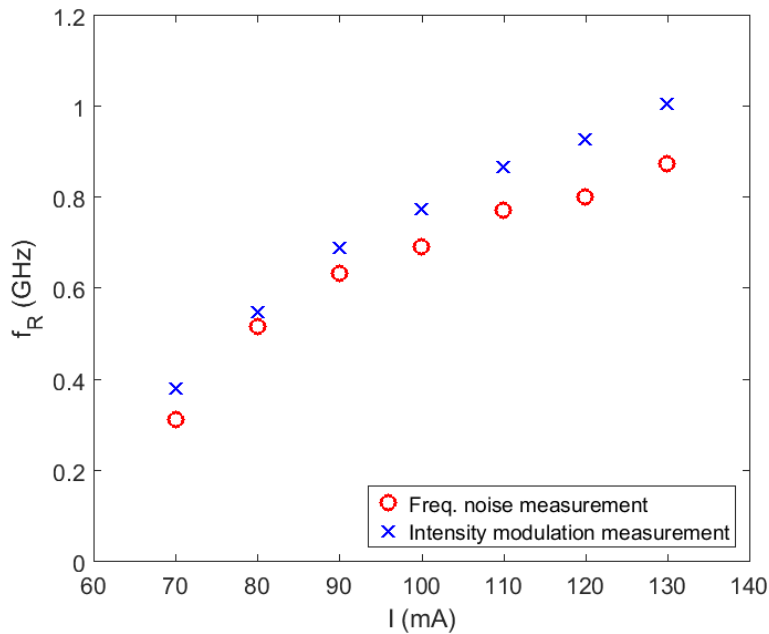


Figure 4.16 Comparison of the relaxation resonance frequencies of the 50 nm QNCL laser at various bias currents, measured from two different measurements: the frequency noise and intensity modulation measurement.

Figure 4.17 shows the frequency noise PSD of the 90 nm QNCL laser ($I_{\text{th}} = 65$ mA, $\lambda_0 = 1556$ nm), together with the extrapolated line. The linewidth enhancement factor of 3.0 (Figure 4.14) is used for the extrapolated line. The measured and the extrapolated lines show a good agreement with each other, up to approximately 1 GHz, including the relaxation resonance frequency at 360 MHz and 680 MHz at 100 mA and 190 mA, respectively.

Hence, we predict that the below- f_R frequency noise 4.5×10^3 Hz²/Hz at the bias current of 100 mA will drop to 450 Hz²/Hz at a few GHz, yielding a Schawlow-Townes linewidth of 1.4 kHz. At a bias current of 190 mA, the frequency noise 1.3×10^3 Hz²/Hz (Schawlow-Townes linewidth: 4 kHz) is expected to decrease to 130 Hz²/Hz (Schawlow-Townes linewidth: 0.4 kHz).

Figure 4.18 shows the comparison of the relaxation resonance frequencies of the 90 nm QNCL laser at various bias currents, measured with the two different methods. The two curves, one from the frequency noise measurement and the other from the IM modulation measurement, match closely, displaying the $\sqrt{I - I_{\text{th}}}$ dependence of the relaxation resonance frequency.

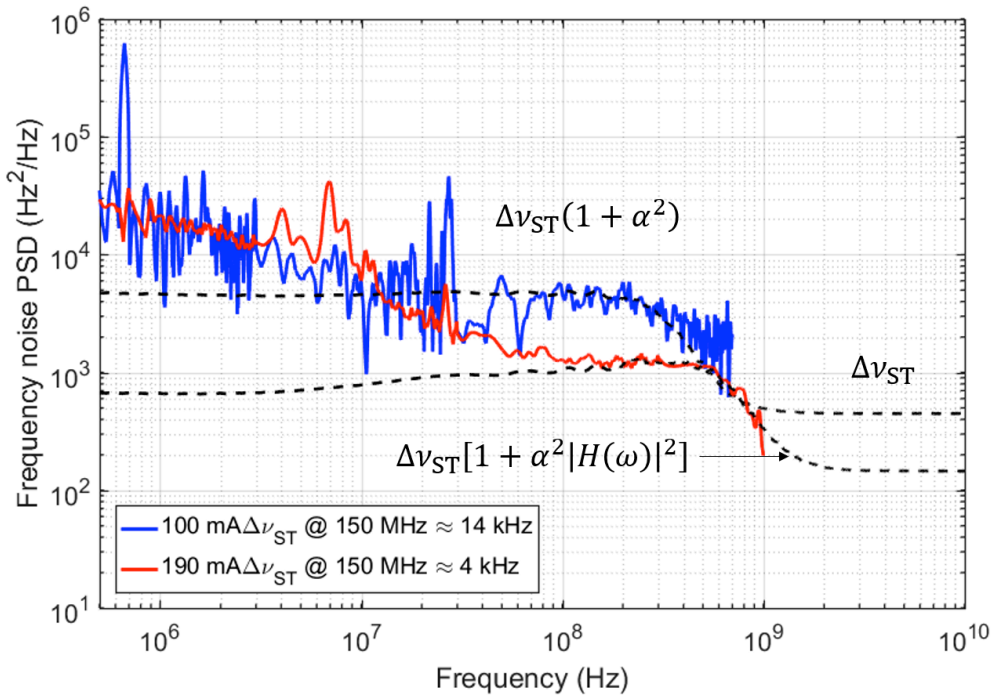


Figure 4.17 Frequency noise PSD of the 90 nm QNCL laser ($I_{th} = 65$ mA, $\lambda_0 = 1556$ nm, $\alpha = 3.0$, device ID: hQsp7 ch9 slot1 bar4 dev9). The extrapolated line for $\Delta\nu_{ST}(1 + \alpha^2 |H(\omega)|^2)$ is overlaid.

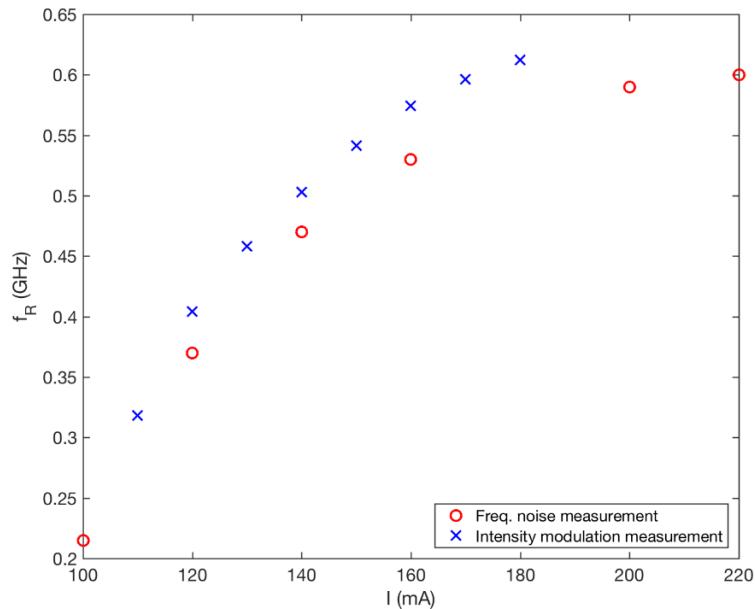


Figure 4.18 Comparison of the relaxation resonance frequencies of the 90 nm QNCL laser at various bias currents, measured from two different measurements: the frequency noise and intensity modulation measurement.

4.7 Discussion and conclusions

In Chapter 3, we described the reduction of the total frequency noise of a laser, by up to two orders of magnitude, compared to conventional III-V only lasers, including both the direct spontaneous emission phase noise as well as the attendant noise due to carrier modulation. This was achieved by modal engineering and by utilizing a low-loss Si material for photon storage and the lossy InP for photon-generation (gain). In this chapter, we investigated the modulation response, and showed that the same modal engineering has a major and beneficial effect on the relaxation resonance frequency.

As discussed in Section 3.4, more conventional methods for controlling the confinement in the active region include the use of tapers to transition between the gain and the passive waveguide region [70] as well as external cavities [50]. In these platforms, the active region confinement factor scales as the square root of the ratio between the length of the active region and the effective length of the cavity. Due to the square root dependence of the relaxation resonance frequencies on the active region confinement factor, a longer external cavity length by two orders of magnitude would be needed to achieve a single order of magnitude reduction in the relaxation resonance frequency. In our platform, however, the same reduction of the relaxation resonance frequency was achieved by just tens-of-nm change in the QNCL thickness, as demonstrated in Figure 4.7.

In this chapter, we also investigated the frequency noise spectrum beyond the relaxation resonance frequency of our lasers. We demonstrated the sub-kHz linewidths at a few GHz range, due to the suppression of the carrier modulation-induced frequency noise at a relatively low frequency.

It is notable that the magnitude of the linewidth enhancement factor is an intrinsic property of the gain medium, regardless of the laser structure. As defined, the linewidth enhancement factor is the change in the refractive index due to an increase in carriers divided by the change of the modal gain due to the same increase in carriers:

$$\alpha = \frac{dn_{r,\text{eff}}/dN}{dn_{i,\text{eff}}/dN} = \frac{\Gamma_{\text{III-V}} dn_{r,\text{III-V}}/dN}{\Gamma_{\text{III-V}} dn_{i,\text{III-V}}/dN} = \frac{dn_{r,\text{III-V}}/dN}{dn_{i,\text{III-V}}/dN}, \quad (4.28)$$

where N is the number of carriers in the gain medium, $n_{r,\text{eff}}$ and $n_{r,\text{III-V}}$ are the real part of the mode's effective index and the average refractive index of the QWs, while $n_{i,\text{eff}}$ and $n_{i,\text{III-V}}$ are

the imaginary part of the refractive index in the QWs. Therefore, for a given material, one cannot eliminate the presence of the linewidth enhancement factor. As discussed in Section 2.2.2, quantum-dots (QDs), for example, do not exhibit a linewidth enhancement factor, due to their delta function-like density of states. However, QDs still remain difficult to grow for certain materials and often exhibit lower material gain than their QW counterparts. The demonstration of the suppression of the linewidth enhancement factors at a relatively low frequency in our lasers means that using this approach, any laser with different material system can reduce to insignificance the effect of phase-amplitude coupling (i.e., the linewidth enhancement factor) at telecommunication relevant frequencies (i.e. a few GHz).

Of further importance is the dependence of the linewidth enhancement factor on the operating wavelength of the laser. It has been shown, both theoretically [30] and experimentally in this chapter, that lasers that operate further from the differential gain peak experience a larger linewidth enhancement factor. Lasers designed with the same gain medium operating at different wavelengths will consequently have different noise characteristics, owing to differences in the linewidth enhancement factor. Here, we showed that our lasers with low relaxation resonance frequencies can be used to suppress the influence of the linewidth enhancement factor above the relaxation resonance frequency. This ensures that lasers operating at different wavelengths will have nearly identical spectral characteristics at a few GHz range.

In conclusion, we demonstrated that engineering of the relaxation resonance frequencies is possible through modal engineering in our high-coherence Si/InP lasers, and the relaxation resonance frequency as low as a few hundreds of MHz is achieved. In addition, we could achieve a frequency noise corresponding to the sub-kHz quantum-limited Schawlow-Townes linewidth at frequencies of a few GHz range, as a consequence of the suppression of the influence of the linewidth enhancement factor.

This sub-kHz linewidth semiconductor laser can be beneficial for many application systems including optical communication as a way to enhance the optical coherent telecommunication capacity.

Chapter 5

FEEDBACK SENSITIVITY

In the optical network, external reflections back into the laser from cleaved facets, splices, dust, connectors, and other components in the system, are unavoidable. This external optical feedback can sometimes be beneficial, as it can be utilized to achieve better side-mode suppression for Fabry-Perot lasers through the gain section mechanism using short external reflectors [71, 72, 73] or to achieve a linewidth narrowing by coupling the laser cavity to a high-Q external resonator [74, 75, 76, 77, 70, 78]. However, in most cases, the external reflections are undesirable, because they lead to an instability and degradation of coherence in semiconductor lasers.

Thus far, consistent performance of semiconductor lasers has been achieved by the use of costly, but indispensable optical isolators in many communication and sensing systems. These non-reciprocal magneto-optic-based devices prevent undesirable external reflections in the optical networks from reaching the laser cavity, and increase the laser stability against optical feedback.

The combination of the use of the high reflectivity mirrors and the relatively long cavity in our high-coherence Si/III-V lasers makes these lasers inherently less sensitive to external feedback. This eliminates the need for costly optical isolators in certain settings. In this chapter, we demonstrate the stability of the lasers against external optical feedback by investigating their fringe visibility and the RF noise spectrum under various levels of external reflections.

5.1 Feedback sensitivity of lasers

A simple analysis regarding the effect of an external cavity to a laser cavity diode can be performed based on the Fabry-Perot-type compound cavity model, as shown in Figure 5.1 (a) [79]. The compound cavity model consists of a laser diode cavity with mirror reflection coefficients r_1 and r_L , and an external cavity with reflection coefficient r_{ext} . The external reflectivity R_{ext} is defined as the ratio between the reflected power and the emitted power,

$$R_{\text{ext}} = r_{\text{ext}}^2 = \frac{P_{\text{reflected}}}{P_{\text{emitted}}}. \quad (5.1)$$

The effective reflection coefficient of the laser, r_{eff} , with optical frequency ν at $z = L$ can be given by,

$$r_{\text{eff}}(\nu) = r_L + (1 - |r_L|^2)r_{\text{ext}}e^{-i2\pi\nu\tau_{\text{ext}}}, \quad (5.2)$$

where τ_{ext} is the round-trip time of the external cavity, which has a length of L_{ext} . We do not consider multiple reflections within the external cavity under the assumption $|r_{\text{ext}}r_L| \ll 1$.

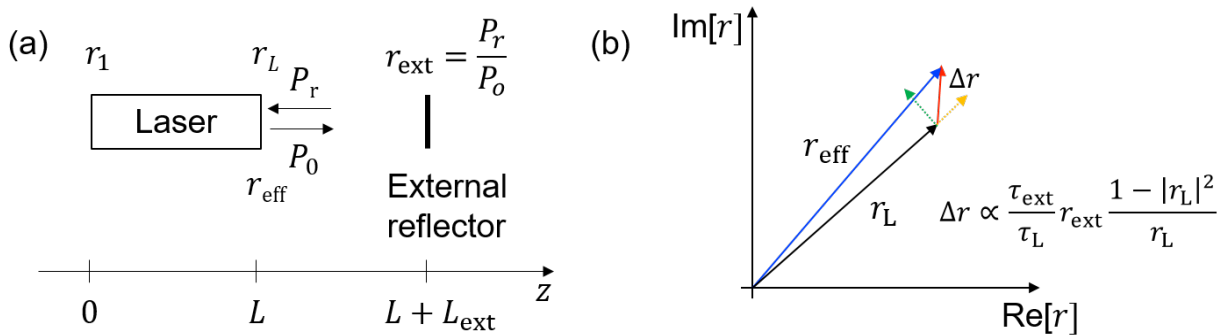


Figure 5.1 (Left) A model of a compound cavity consisting of a laser diode and an external optical reflection. (Right) A diagram for the effective laser cavity mirror reflection. Δr represents a perturbation by the external optical feedback to the reflection coefficient of the laser cavity mirror.

In the presence of external reflection, the effective reflection coefficient r_{eff} varies. This causes variation in the laser cavity loss, and subsequently the threshold gain (dotted yellow line in Figure 5.1 (b)). The required gain in the laser under feedback is given by,

$$g_c = g_{\text{th}} - \frac{\kappa_{\text{ext}}}{L} \cos(2\pi\nu\tau_{\text{ext}}), \quad (5.3)$$

where g_{th} is the threshold gain with external feedback. The coupling coefficient κ_{ext} to the external cavity is defined as,

$$\kappa_{\text{ext}} = \frac{\tau_{\text{ext}}}{\tau_L} (1 - |r_L|^2). \quad (5.4)$$

In addition to the gain variation, the external reflection causes the laser's round trip phase change $\Delta\phi_L$, through the direct mirror phase change (dotted green line in Figure 5.1 (b)), the lasing frequency change, and the refractive index change induced by the threshold gain variation (dotted yellow line in Figure 5.1 (b)). The round trip phase change, due to the carrier density change, is again related to the refractive index change through the linewidth enhancement factor α . Then, the round-trip phase change $\Delta\phi_L$, due to the external feedback, is written as [29],

$$\Delta\phi_L = 2\pi\tau_L(\nu - \nu_{th}) + \kappa_{ext}\sqrt{1 + \alpha^2} \sin(2\pi\nu\tau_{ext} + \text{atan } \alpha), \quad (5.5)$$

where ν_{th} is the lasing frequency without feedback, and $\tau_L = 2n_{eff}L/c$ is the round-trip time of the solitary laser diode cavity.

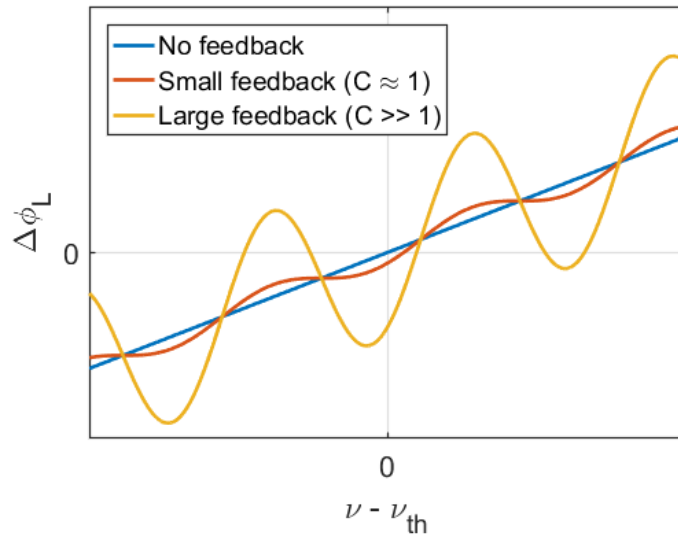


Figure 5.2 The round trip phase change $\Delta\phi_L$, as a function of the optical frequency ν at different levels of external optical feedback. ν_{th} represents the lasing frequency when there is no feedback ($\Delta r = 0$). The resonant phase condition of the compound cavity is satisfied when $\Delta\phi_L = 0$.

The feedback sensitivity of a laser is essentially governed by a parameter called a *feedback coefficient* C , defined as

$$C = X\sqrt{1 + \alpha^2} = \frac{\tau_{\text{ext}}}{\tau_L} \kappa_{\text{ext}} \sqrt{1 + \alpha^2} = \frac{\tau_{\text{ext}}}{\tau_L} r_{\text{ext}} \frac{1 - |r_L|^2}{r_L} \sqrt{1 + \alpha^2}. \quad (5.6)$$

$$\text{Equations } C = X\sqrt{1 + \alpha^2} = \frac{\tau_{\text{ext}}}{\tau_L} \kappa_{\text{ext}} \sqrt{1 + \alpha^2} = \frac{\tau_{\text{ext}}}{\tau_L} r_{\text{ext}} \frac{1 - |r_L|^2}{r_L} \sqrt{1 + \alpha^2}. \quad (5.6) \quad \text{and}$$

Error! Reference source not found.) show that a laser with a stronger mirror (large r_L) and a long cavity (large τ_L) is less sensitive to the external reflections for a given external reflector configuration with a fixed external cavity round trip delay τ_{ext} and an external reflection coefficient r_{ext} . Therefore, a laser with a high endurance against optical feedback can be obtained: (1) by increasing the round-trip group delay τ_L of the laser by increasing the cavity length, (2) by decreasing the coupling to the external cavity (i.e., κ_{ext}) by increasing the laser's mirror reflection coefficient r_L , or (3) by decreasing the linewidth enhancement factor α .

Error! Reference source not found. describes the round-trip phase change as a function of the frequency ν , according to Equation $\Delta\phi_L = 2\pi\tau_L(\nu - \nu_{\text{th}}) + \kappa_{\text{ext}}\sqrt{1 + \alpha^2} \sin(2\pi\nu\tau_{\text{ext}} + \text{atan } \alpha)$, (5.5). The zeros that meet the phase condition $\Delta\phi_L = 0$ correspond to the possible lasing frequencies. When there is no feedback (which corresponds to the blue line in **Error! Reference source not found.**), the lasing occurs at frequency ν_{th} , i.e., the lasing frequency without a feedback. The five different regimes of the feedback effects have been studied and identified as a function of the feedback coefficient C , as the amount of the external reflection increases. [80].

In Regime I, with a small amount of external feedback, characterized by a feedback coefficient C of less than 1, Equation $\Delta\phi_L = 2\pi\tau_L(\nu - \nu_{\text{th}}) + \kappa_{\text{ext}}\sqrt{1 + \alpha^2} \sin(2\pi\nu\tau_{\text{ext}} + \text{atan } \alpha)$, (5.5) has one solution for the frequency ν . The red line in **Error! Reference source not found.** illustrates the case where the round-trip phase change $\Delta\phi_L$ still increases monotonically with an increasing frequency, yielding only one solution that satisfies the resonant condition $\Delta\phi_L = 0$. Only a small change in the linewidth broadening or narrowing takes place depending on the phase of the external feedback, maintaining a single mode operation [79, 81].

In Regime II, the feedback coefficient C becomes larger than 1 (yellow line in **Error! Reference source not found.**). The round-trip phase change $\Delta\phi_L$ undergoes strong oscillations so that $\Delta\phi_L$ is zero at more than one frequency, and the laser can oscillate at a number of frequencies near ν_{th} . Transitioning from Regime I to Regime II, a second external cavity mode appears, thus creating a linewidth splitting [82, 81].

As the amount of feedback increases further, the strong feedback makes the threshold gain difference for the different external cavity modes stronger. In Regime III, the mode hopping between the external cavity modes is suppressed. A stable external cavity mode lasing with a large linewidth reduction is achieved through the gain selection mechanism and the extended total cavity length [71, 72, 73]. This regime only occurs in a small range of the external feedback level.

In Regime IV, with further increased feedback, strong laser instability occurs, which is evidenced by the drastic increase in the intensity and the phase noise of the laser. Because of the complete loss of coherence, this regime is termed “coherence collapse”. In the coherence collapse regime, one observes an extreme broadening of the laser linewidth up to several tens of GHz [83, 84, 85], and a drastic increase in the laser relative intensity noise (RIN) [86]. In optical fiber communication, coherence collapse results in an increase in bit error rate (BER), and should be avoided [87, 88].

In Regime V, the external reflector starts to have a stronger reflectivity than the laser cavity reflectivity. As such, it basically forms an external cavity laser.

The most undesirable laser operation takes place in the coherence collapse regime. Consequently, we will focus our attention on identifying this regime in our lasers.

5.2 Feedback sensitivity of QNCL

Section 5.1 illustrates that it is desirable to have a high mirror reflectivity r_L to reduce the laser feedback sensitivity. But for a given laser cavity with a fixed intrinsic loss, the mirror reflectivity cannot be increased indefinitely, because it would suppress the optical output power. Thus, to achieve the same output power with a higher-reflectivity mirror would require a reduction of the intrinsic cavity loss.

To achieve a narrow linewidth, the key strategy of our high-coherence Si/III-V laser was the reduction of the modal loss in the laser cavity by storing most of the modal energy in the low-loss Si instead of the III-V. By moving modal energy away from III-V to Si, we increase the Q-factor and thus increase the stored number of photons at a given current. This enables us to increase the mirror reflectivity for the same output power. This makes our lasers less sensitive to external reflections.

To compare the feedback sensitivity of our lasers with the conventional III-V lasers, let us assume that the mirror loss of each laser (i.e., Q_{ext}) is designed to be 30% of the intrinsic cavity loss (i.e., Q_{total}) to achieve optimum output power.

With a proper assumption for the intrinsic loss for each layer (i.e., $Q_{\text{Si}} = 10^6$ and $Q_{\text{III-V}} = 10^4$), Q_{ext} , which yields the optimal output power, can be calculated as a function of the confinement factor in the III-V layer (Figure 5.3 (left axis)). This, in turn, allows us to compute the mirror reflectivity R using the following equation,

$$Q_{\text{ext}} = \frac{\omega}{v_g \alpha_m} = \frac{\omega}{v_g \left(\frac{1}{L} \ln \frac{1}{R} \right)} = \frac{\omega \tau_L}{\ln(1/R)}, \quad (5.7)$$

where L is the laser cavity length. Using the calculated mirror reflectivity R , the ratio of the feedback coefficient C between the heterogeneous laser and the III-V only laser can be extracted using Equation $C = X \sqrt{1 + \alpha^2} = \frac{\tau_{\text{ext}}}{\tau_L} \kappa_{\text{ext}} \sqrt{1 + \alpha^2} = \frac{\tau_{\text{ext}}}{\tau_L} r_{\text{ext}} \frac{1 - |r_L|^2}{r_L} \sqrt{1 + \alpha^2}$. (5.6), under the assumption that the lasers have the same cavity length τ_L . The effective isolation, compared to the III-V only laser, can then be obtained as,

$$\text{Effective isolation (dB)} = 20 \log \frac{C_{\text{QNCL}}}{C_{\text{III-V}}} = 20 \log \frac{(1 - R_{\text{QNCL}}) / \sqrt{R_{\text{QNCL}}}}{(1 - R_{\text{III-V}}) / \sqrt{R_{\text{III-V}}}}. \quad (5.8)$$

The right axis of Figure 5.3 illustrates the effective isolation of the high-coherence Si/III-V laser. Considering that the lasers possess a confinement factor in the III-V layers of 10%, 2.5%, and 1% for 50nm, 100 nm, and 150 nm QNCL thickness, respectively (Figure 2.3), we can expect that the lasers would be less sensitive to the external optical reflections than a III-V only laser by 10 to 30 dB. This calculation did not account for the optical cavity length difference. Thus, we can expect even further improvement from our lasers, considering their large cavity length, owing to the use of the extended defect-mode resonator.

In the remainder of this chapter, the improved feedback sensitivity of our lasers is demonstrated by experimental data by searching the coherence collapse regime, while monitoring the optical linewidth, the interferometric fringe visibility, and the relative intensity noise under external

feedback. The coherence collapse manifests itself as an abrupt linewidth broadening, a sudden drop in the fringe visibility, and a drastic enhancement of the RIN.

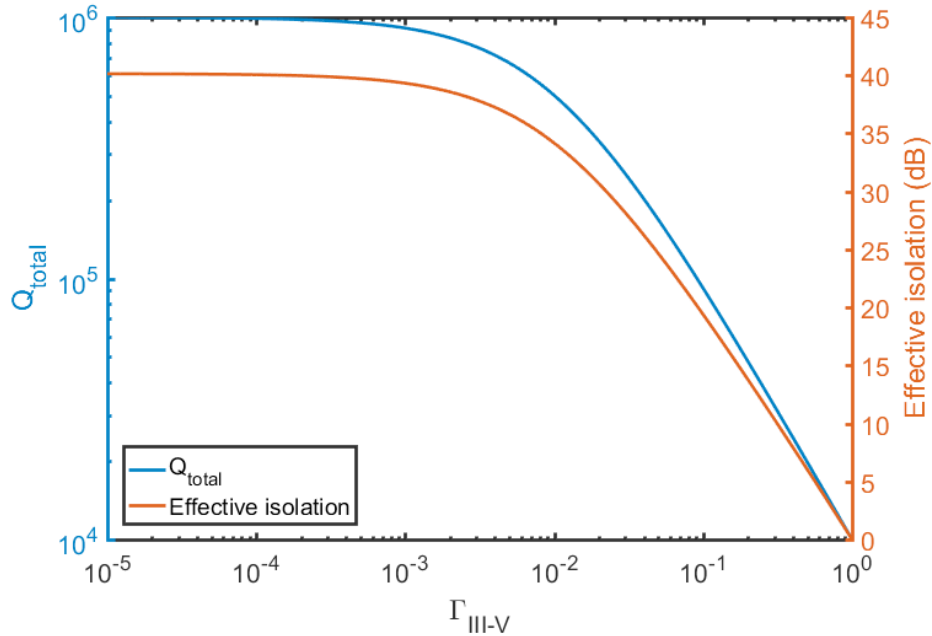


Figure 5.3 Q-factor of the heterogeneous laser and the effective isolation, compared to the conventional III-V laser, as a function of the confinement factor in the III-V layer (Assumption: $Q_{\text{Si}} = 10^6$ and $Q_{\text{III-V}} = 10^4$).

5.3 MZI fringe visibility measurement

5.3.1 Measurement setup

The interferometric fringe visibility is a good measure to quantify the coherence of two or more waves. Two or more waves are combined and the intensity of the combined wave varies from a maximum to a minimum as a function of the phase difference between them. The fringe visibility is defined as the ratio of the amplitude of the resulting oscillating wave envelope $(I_{\text{max}} - I_{\text{min}})/2$ to the average amplitude $(I_{\text{max}} + I_{\text{min}})/2$. It can be written as

$$V = \frac{I_{\text{max}} - I_{\text{min}}}{I_{\text{max}} + I_{\text{min}}}, \quad (5.9)$$

where $I_{\max/\min}$ are the maximum/minimum intensity measured on a photodetector collecting light from the interferometer.

Experimentally, we combine the wave in an uneven MZI. The phase difference is controlled by varying the delay τ (sec). As we pass the laser light through the MZI, we combine the emitted laser field $E(t)$ and a time-delayed version of itself $E(t - \tau)$ at the output of the MZI, with a time delay $\tau = 1/\text{FSR}$. Since the laser is not a perfectly monochromatic source, the phases of the two interfering fields become progressively less correlated with each other, as the time delay τ increases. The envelope of the interference pattern V can be given by

$$V = e^{-\tau/\tau_c}, \quad (5.10)$$

where τ_c is the coherence length of the laser. Plugging $\tau = 1/\text{FSR}$ and $\tau_c = 1/\Delta\nu$ ($\Delta\nu$: laser linewidth) [26, p. 59] into the above equation yields

$$V = e^{-\Delta\nu/\text{FSR}}. \quad (5.11)$$

The fringe visibility, in the case where the laser output is fed into the MZI, will be close to 1 if the laser linewidth is much smaller than the FSR of the MZI. However, it will drop rapidly, if the laser linewidth becomes comparable to the FSR.

To characterize the laser's fringe visibility under the external optical feedback, two types of setup are used (Figure 5.4). To collect the laser light into the fiber, the light is coupled into the slow axis of a polarization maintaining (PM) fiber using a lensed fiber. A coupling efficiency typically in the range of 30 to 40% is measured.

The top path of the setup, created by the forward 95% tap of the fiber coupler, is used to create an external optical reflection. The magnitude of the reflection is controlled using a variable attenuator.

In Setup I, the artificial reflection is created by a gold fiber mirror (model number). In this setup, due to the assumed coupling efficiency $\eta = 50\%$, the insertion loss of 2.8 dB in the variable attenuator, and the 95% tap fiber coupler, the maximum achievable external reflectivity R_{ext} becomes approximately -12 dB.

In Setup II, a booster optical amplifier (BOA) is placed in the loop. The BOA is used to overcome the coupling efficiency of the lensed fiber and the insertion losses in the fiber network. It will then increase the total magnitude of the external reflection. An amplifier is unidirectional, since it has a built-in isolator in the package. Therefore, a circulator has to be used to feed the light in the loop back into the laser. The amplifier creates another 10 dB of external reflection, enabling the maximum reflectivity R_{ext} to reach 0 dB. The ability to reach reflectivity near unity is necessary to measure the onset of coherence collapse of the expectantly feedback-insensitive Si/III-V lasers. In this setup, the optical fiber path length is approximately 10 m.

It is worth noting that the fiber network in the top path creating the external reflection is made using polarization maintaining (PM) fibers to ensure that the reflected light has the same polarization as the emitted light.

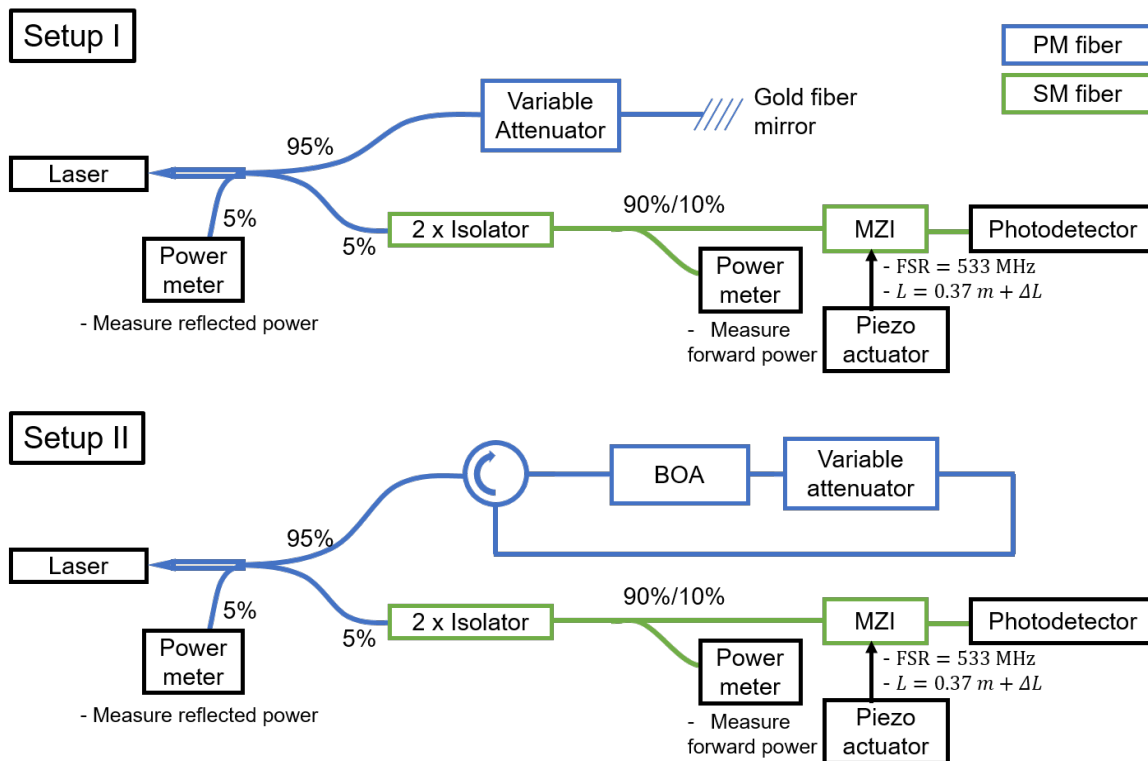


Figure 5.4 . The measurement setup used to quantify the MZI fringe visibility. The top path allows for the precise control of the magnitude of the external optical feedback. A variable attenuator is used to vary the amount of the external optical reflection going back into the laser. A booster optical amplifier (BOA) is used to enable the reflectivity to approach unity even in the presence of losses included in the fiber network. The bottom path measures the fringe visibility of the laser output as it passes through a MZI. Two isolators are used to prevent reflection from

the measurement loop from going back into the laser. A piezo-actuator is controlled by a function generator, and is used to provide a small length variation to display interference fringes.

The bottom path of both setups (i.e., Setup I and II) is used as a characterization path to monitor and quantify the fringe visibility. The light in the forward 5% tap is passed through two isolators to remove any external feedback from the bottom path, and an MZI, with a free spectral range (FSR) of 533 MHz. A piezo-actuator provides a few microns of a length variation to one arm of the MZI, at a rate of 1 kHz, to display the interference fringe pattern. The interfered light, passed through the MZI, is routed to a photodetector. The voltage generated from the photodetector is measured using an oscilloscope. For each attenuation of the variable attenuator, the fringe visibility is taken 10 times with a delay of a few seconds between each measurement.

The four-port 95%/5% fiber coupler also creates taps to measure the backward and forward power in the fiber loop. The external reflectivity R_{ext} is calculated by using the measured backward and forward power, the coupling efficiency, the insertion loss of the fiber coupler, the isolators, and the variable attenuator. The coupling efficiency and the insertion losses are characterized prior to conducting the experiment.

5.3.2 Experimental results

Figure 5.5 illustrates the change in the fringe visibility of a commercial high-end DFB laser (i.e., QPhotonics, model number: QDFBLD-1550-5AX), which has no packaged isolator, as a function of time at different external feedback levels, when the laser is pumped with 40 mA ($I_{\text{th}} = 5$ mA).

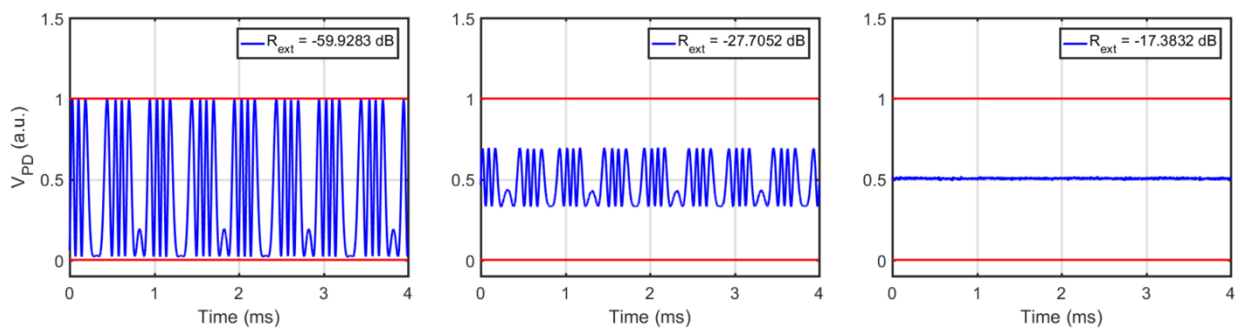


Figure 5.5 The MZI fringe visibility of the commercial HR/AR coated DFB laser ($I = 30$ mA, $I_{\text{th}} = 5$ mA), as a function of time. (Left) The fringe visibility of 1 is maintained under weak feedback condition ($R_{\text{ext}} = -60$ dB). (Middle) As the feedback increases to $R_{\text{ext}} = -27$ dB, the fringe visibility starts to drop as the laser goes into the coherence collapse. (Bottom) The fringe

visibility becomes 0, i.e., in our case $\tau_c \ll 1/\text{FSR}$, the laser completely loses coherence under strong feedback ($R_{\text{ext}} = -17$ dB).

Under a weak feedback condition of $R_{\text{ext}} = -60$ dB, the laser maintains a high fringe visibility. As the feedback level increases to -28 dB, the fringe visibility starts to drop. When the feedback level reaches -17 dB, the laser loses its coherence completely (i.e., $\tau_c \ll 1/\text{FSR}$) and the fringe visibility becomes 0.

Figure 5.6 presents the fringe visibility of the laser as a function of the external reflectivity R_{ext} . The laser starts to go into the coherence collapse regime (i.e., onset of coherence collapse) at approximately $R_{\text{ext}} = -44$ dB. It goes into the complete coherence collapse regime at $R_{\text{ext}} = -20$ dB. The fringe visibility plots measured using two different setups, one using a gold fiber mirror and the other using an amplifier and a circulator, show good agreement with each other. This demonstrates that the setup, using an amplifier and a circulator, can create the same external reflection as a mirror while boosting the maximum achievable external reflectivity. The results reveal that the maximum achievable external reflectivity is approximately -8 dB, whereas the setup using the amplifier creates the maximum external reflectivity of unity (0 dB). The right axis of Figure 5.6 illustrates the level of the power emitted out of the laser and the reflected power going back into the laser.

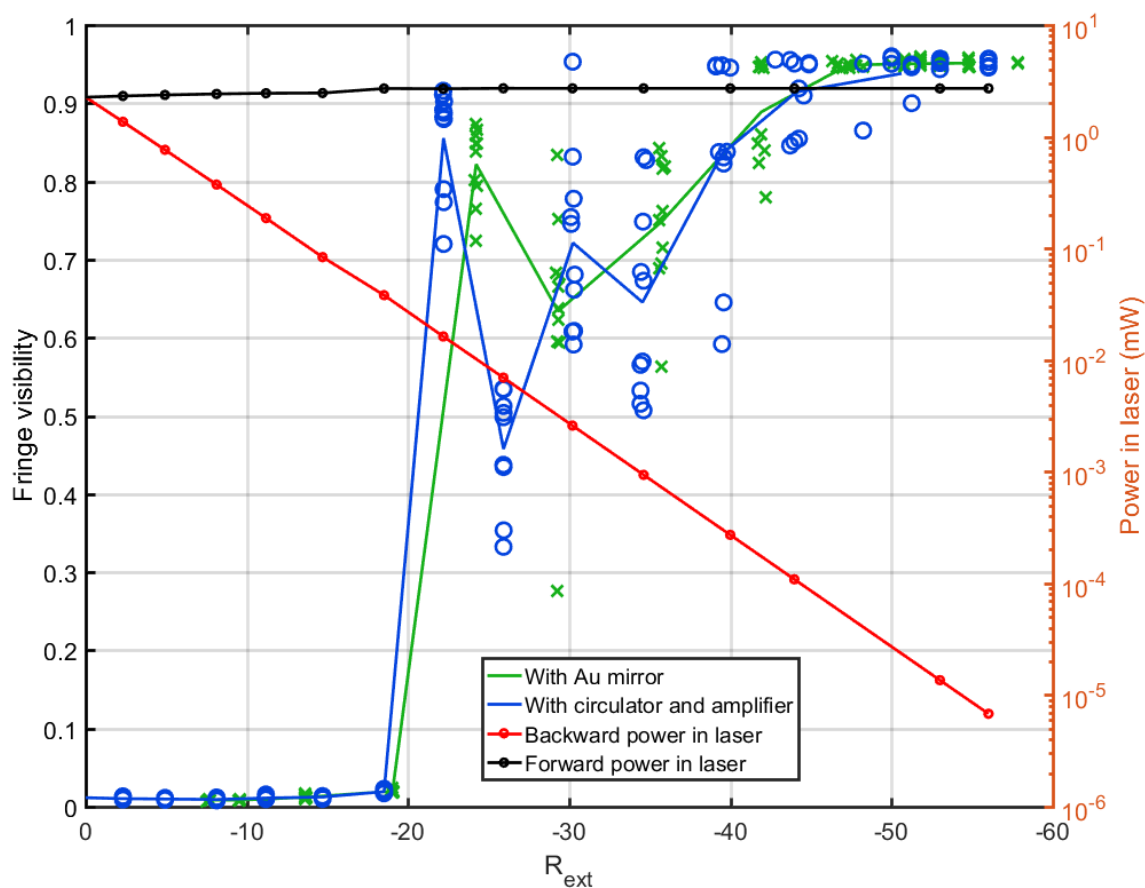


Figure 5.6 The MZI fringe visibility measurement of the commercial DFB laser (QPhotonics, $I = 30$ mA, $I_{th} = 5$ mA) using two different setups (Figure 5.4), as a function of the external reflectivity R_{ext} . The two different setups, one using a gold fiber mirror and the other using an amplifier and a circulator, yield nearly the same result. The setup using an amplifier can create a maximum external reflectivity up to approximately 0 dB. The emitted power and the reflected power going into the laser are shown on the right axis of the plot.

Figure 5.7 compares the fringe visibility of the same commercial DFB laser, which has no packaged isolator, to that of the laser when an isolator (FDK YD-460) is placed at the output of the laser. When the isolator is present, the laser maintains coherence, even when the power that goes back into the laser is the same as the power emitted from the laser (i.e., $R_{ext} = 0$ dB). This demonstrates the isolation effect of 42 dB of the isolator used in the experiment.

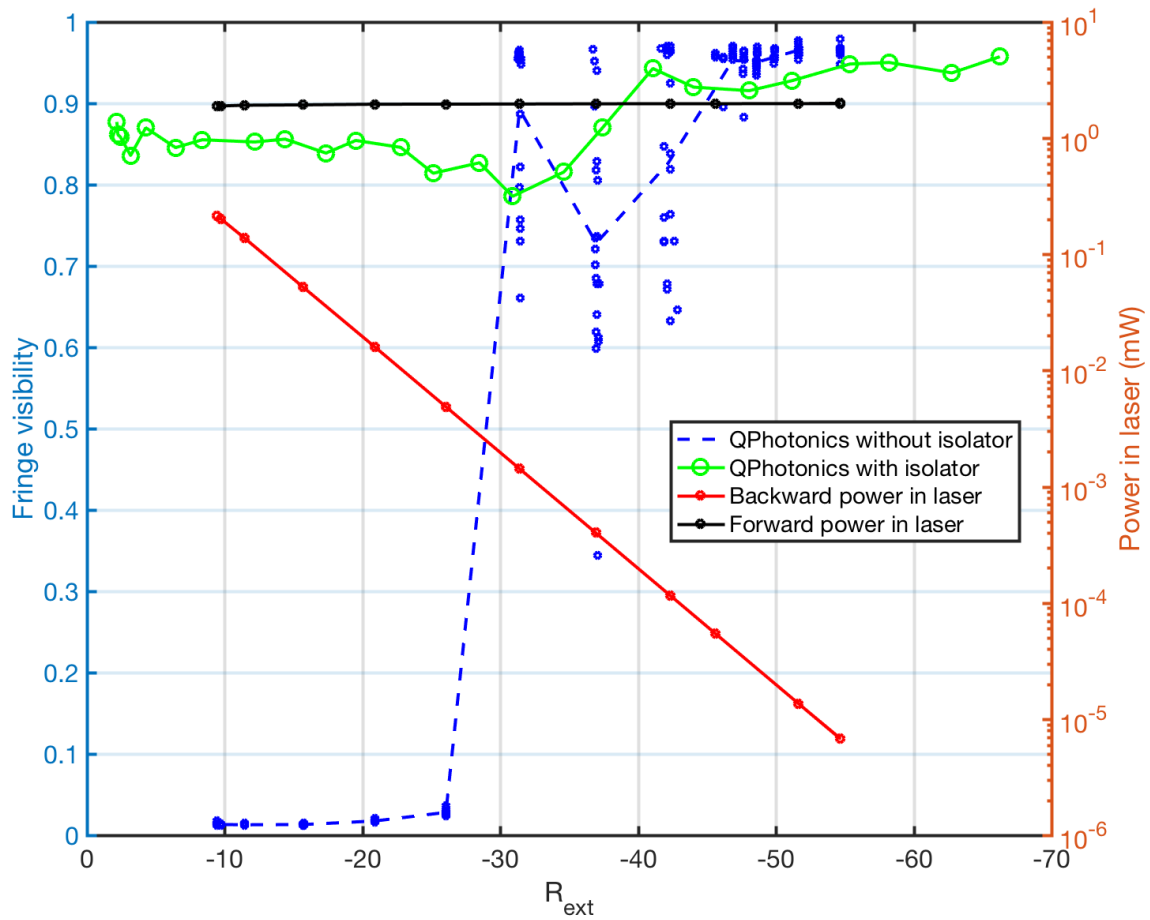


Figure 5.7 The MZI fringe visibility measurement of the commercial DFB laser (QPhotonics, $I = 15$ mA, $I_{\text{th}} = 5$ mA) as a function of the external reflectivity R_{ext} . As a control experiment, the fringe visibility measurement is performed on the same laser after placing an isolator at the output of the laser.

Finally, using the setup with a circulator and an amplifier in the loop, we measure the fringe visibility of the 50 and 90 nm QNCL high-coherence lasers. Figure 5.8 shows the fringe visibility of the commercial DFB laser, the 50 nm ($I_{\text{th}} = 100$ mA, $\lambda_0 = 1560$ nm) and 90 nm ($I_{\text{th}} = 80$ mA, $\lambda_0 = 1556$ nm) QNCL lasers all together.

The 50 nm QNCL laser, biased at 200 mA, experiences the onset of coherence collapse at a reflectivity of R_{ext} between -21 and -18 dB, and complete coherence collapse from $R_{\text{ext}} = -10$ dB. The onset of coherence collapse of the 90 nm QNCL laser, biased at 160 mA, is at the level between -19 and -14 dB. It goes into complete coherence collapse at $R_{\text{ext}} = -9$ dB.

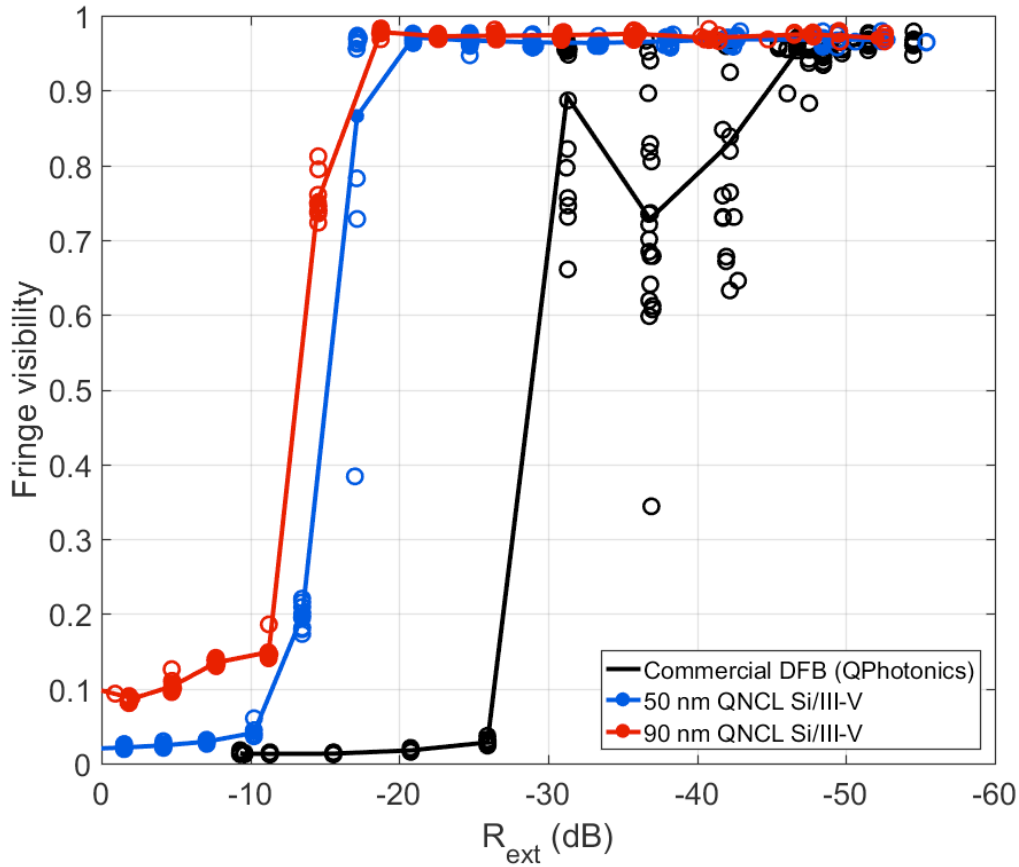


Figure 5.8 MZI fringe visibility of the commercial laser (QPhotonics, $I = 15$ mA, $I_{th} = 5$ mA), 50 nm (device ID: hQsp7 ch8 slot1 bar7 dev10, $I = 200$ mA, $I_{th} = 100$ mA), and 90 nm (device ID: hQsp7 ch09 slot1 bar4 dev05, $I = 160$ mA, $I_{th} = 80$ mA) QNCL lasers.

Considering that, on the system level, a single-mode operation is needed throughout, we compare the external reflectivity of each laser at which it starts to experience the onset of the coherence collapse. The 50 nm and 90 nm QNCL lasers possess an insensitivity to reflection feedback comparable to a commercial DFB laser, employing 25 dB and 30 dB isolation, respectively.

5.4 Relative intensity noise (RIN) measurement

5.4.1 Measurement setup

The onset of coherence collapse of the lasers can also be characterized by investigating the RF intensity noise spectrum, using the setup shown in Figure 5.9.

The top path creates an artificial external optical reflection, and uses the same setup as the fringe visibility measurement setup described in 5.3.1. In this setup, however, the light emitted from the laser under feedback is directly fed into a photodetector to measure the RF intensity noise without passing it through an MZI. The laser RIN is then measured using an RF spectrum analyzer.

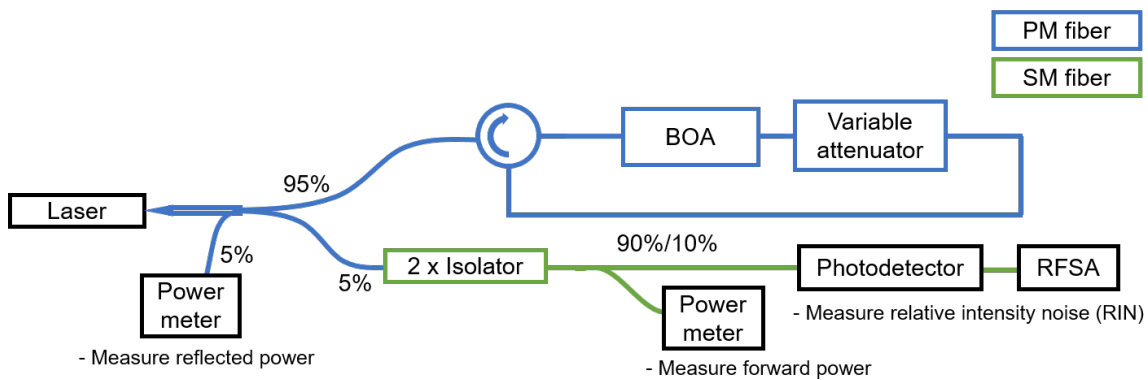


Figure 5.9 The setup to measure the relative intensity noise (RIN) of the laser in the presence of the external reflection. The laser light is directly fed into a photodetector; the RF spectral density of the intensity noise is measured using an RF spectrum analyzer.

5.4.2 Experimental results

Figure 5.10 shows the RF intensity noise spectrum of the commercial DFB laser (QPhotonics) at different level of external feedback.

When the feedback is very small ($R_{\text{ext}} \approx -45$ dB), the laser is below the coherence collapse regime and shows a stable trace of RIN. At the external feedback level of $R_{\text{ext}} = -40$ dB, the noise spectrum begins to rise at RF frequencies near the relaxation resonance frequency at approximately 10 GHz [89]. The intensity modulation characteristics of this laser, discussed in Section 4.4.2, are overlaid on top of the RF intensity noise for comparison purposes. The relaxation resonance frequency is observed to occur at the same location in both measurements. The inset in Figure 5.10 shows that the oscillations are at harmonics of $1/\tau_{\text{ext}}$. The feedback level of the onset

of coherence collapse of $R_{\text{ext}} = -40$ dB is approximately the same as that of the onset of coherence collapse in the fringe visibility measurement (Figure 5.8).

With a further increase of feedback to $R_{\text{ext}} = -30$ dB, the instabilities spread to the frequencies farther removed from that of the relaxation resonance. A resonance structure with peaks at harmonics of $1/\tau_{\text{ext}}$ is superimposed on the IM response of the laser, with a natural resonance peak at the relaxation resonance frequency.

Figure 5.11 presents the RF intensity noise spectrum of the 50 nm QNCL laser ($I_{\text{th}} = 100$ mA, $\lambda_0 = 1560$ nm) at different levels of external feedback. A stable RIN signal is measured at the small feedback level of $R_{\text{ext}} \approx -28$ dB. The laser shows the onset of coherence collapse at approximately $R_{\text{ext}} = -15$ dB, displaying instabilities near the relaxation resonance frequency of 10 GHz. The same relaxation resonance frequency is observed in the overlaid IM response of the laser. The complete coherence collapse occurs at $R_{\text{ext}} = -10$ dB. The onset of the coherence collapse and the complete coherence collapse levels, measured in the intensity noise, are in an agreement with those from the fringe visibility measurement.

Figure 5.12 shows the RF intensity noise spectrum of the 90 nm QNCL laser ($I_{\text{th}} = 80$ mA, $\lambda_0 = 1556$ nm) at different levels of external feedback. The onset of coherence collapse of the laser occurs at $R_{\text{ext}} = -12$ dB, and complete coherence collapse is observed at $R_{\text{ext}} = -9$ dB.

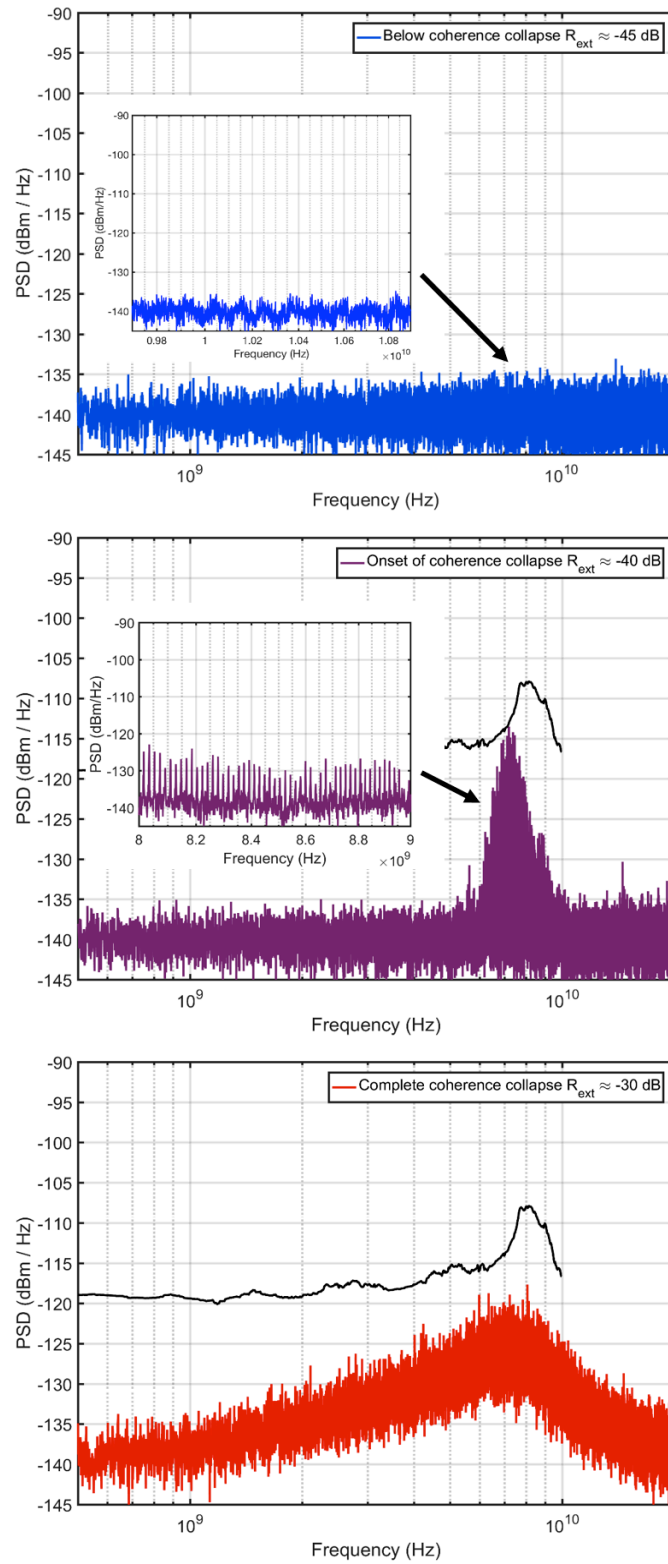


Figure 5.10 The RF RIN spectrum of the commercial AR/HR coated DFB laser (QPhotonics, $I = 20$ mA, $I_{\text{th}} = 5$ mA).

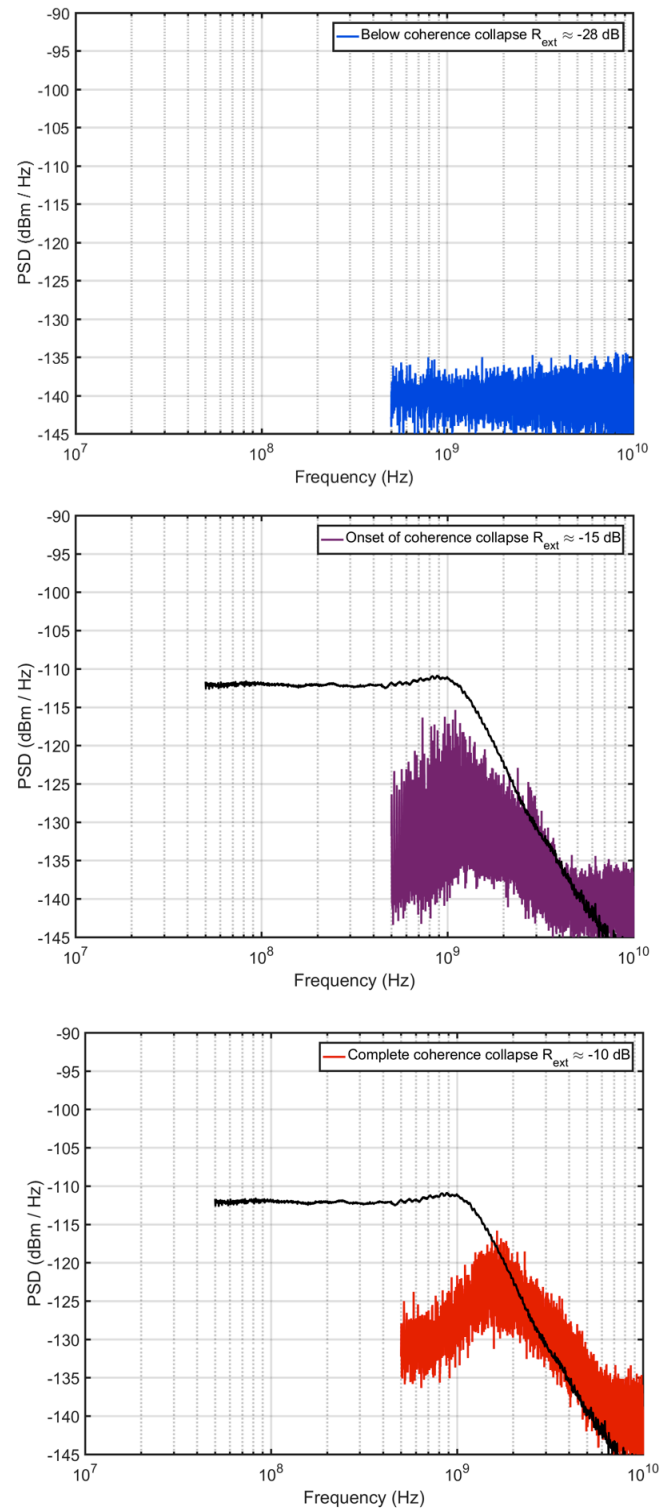


Figure 5.11 The RF RIN spectrum of the 50 nm QNCL Si/III-V laser (device ID: hQsp7 ch08 slot1 bar7 dev10, $I = 200$ mA, $I_{\text{th}} = 100$ mA).

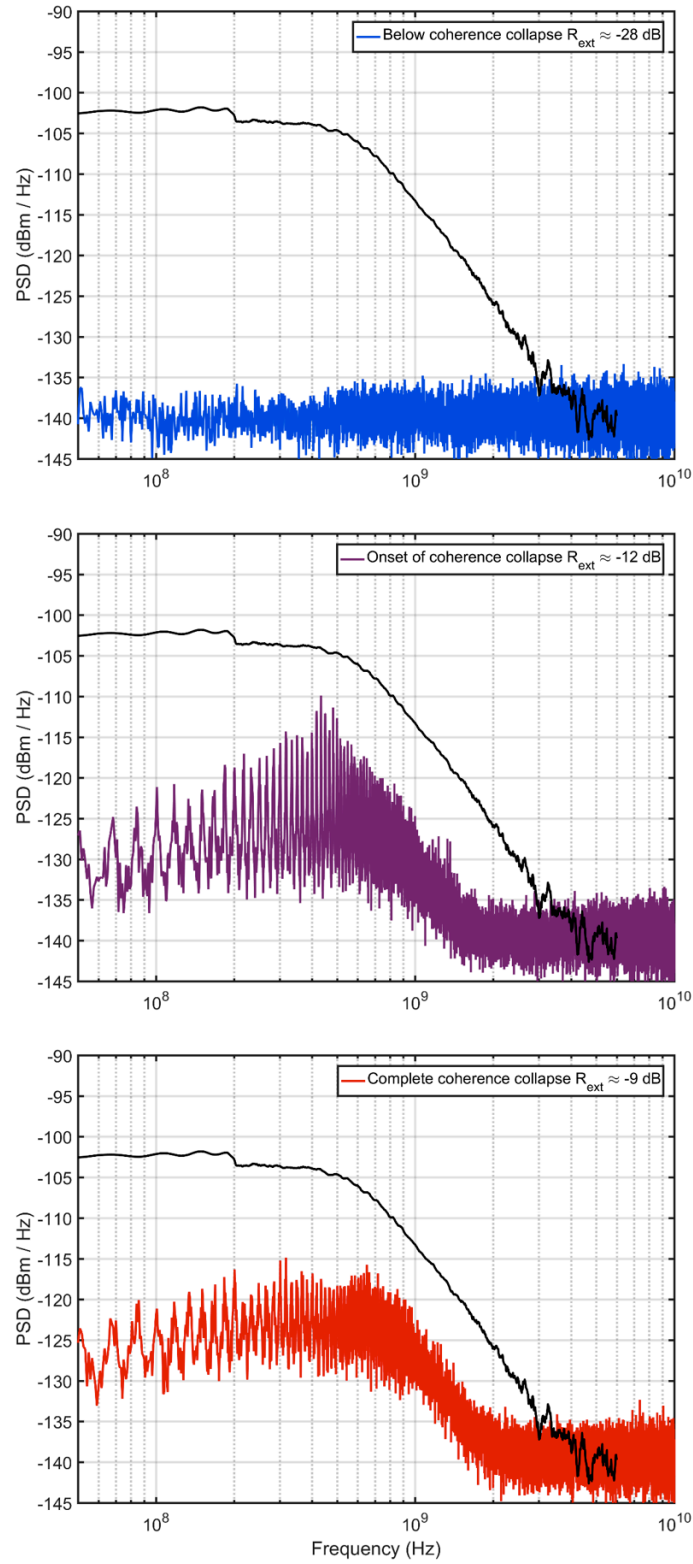


Figure 5.12 The RF RIN spectrum of the 90 nm QNCL Si/III-V (device ID: hQsp7 ch09 slot1 bar4 dev05, $I = 150$ mA, $I_{\text{th}} = 80$ mA).

5.5 Optical spectrum measurement

The optical spectrum of the lasers under feedback are monitored with an optical spectrum analyzer. The resolution bandwidth (RBW) is 0.08 nm (approximately 10 GHz at 1550 nm).

Figure 5.13 shows the optical spectrum of the commercial DFB laser (QPhotonics), as well as the 50 nm, and the 90 nm QNCL lasers under different levels of external feedback.

The commercial laser illustrates a linewidth broadening from the level of $R_{\text{ext}} = -22$ dB. The 50 nm and 90 nm QNCL lasers do not display a linewidth broadening under any feedback level.

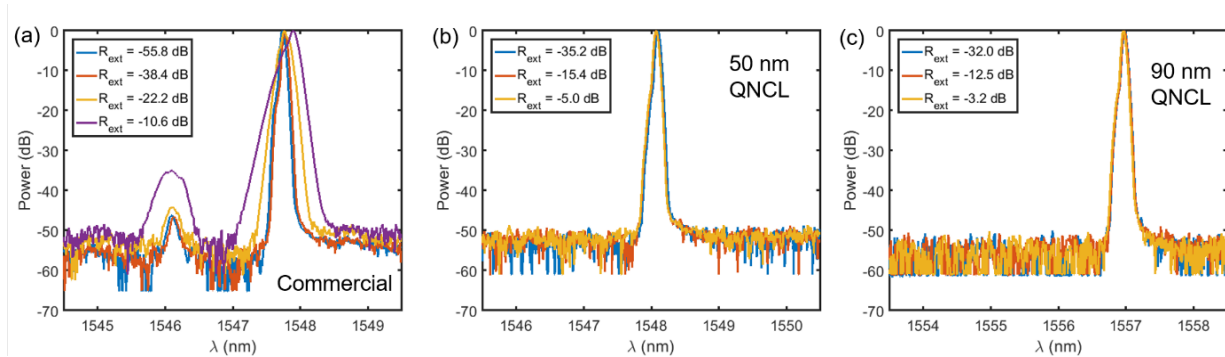


Figure 5.13 The optical spectrum under different levels of external feedback: (a) commercial laser (QPhotonics, $I = 40$ mA, $I_{\text{th}} = 5$ mA), (b) 50 nm QNCL laser (device ID: hQsp7 ch8 slot 1 bar7 dev10, $I = 180$ mA, $I_{\text{th}} = 100$ mA), and (c) 90 nm QNCL laser (device ID: hQsp7 ch09 slot1 bar4 dev05, $I = 200$ mA, $I_{\text{th}} = 80$ mA).

5.6 Discussions and conclusions

In Figure 5.10, Figure 5.11, and Figure 5.12, all lasers exhibit instabilities with maximum response near the relaxation resonance frequency. This is because of the natural resonance of the laser's carrier-photon coupling system against the external perturbations. An important consequence of the reduced relaxation resonance frequency of the high-coherence QNCL Si/III-V lasers, discussed in Section 4.4, is that the relaxation resonance frequency sets a limit to the bandwidth of the RIN spectrum, induced by the optical feedback. This means that noise at a frequency above the relaxation resonance frequency is highly suppressed. Thus, the Si/III-V lasers rarely exhibit the RF intensity noise at frequencies larger than the relaxation resonance frequency (Figure 5.11 and Figure 5.12). The commercial DFB laser (QPhotonics) had a relaxation resonance frequency at approximately 8 GHz (Figure 5.10), whereas the 50 nm and 90 nm QNCL lasers had relaxation resonance frequencies at 1 GHz and 600 MHz, respectively (Figure 5.11 and Figure

5.12). Accordingly, the subsequent linewidth broadening of the laser would not significantly exceed the bandwidth of the relaxation resonance frequency. This is evidenced by the optical spectrum measurement (Figure 5.13), in which the OSA cannot resolve the increased linewidth of the high-coherence lasers with a resolution bandwidth of 0.08 nm (10 GHz at 1550 nm).

As discussed in Section 5.1, the technological remedy that could be used to improve the laser's stability against external reflections included the use of an active material with a low linewidth enhancement factor. Quantum-dot-based semiconductor lasers should show high resistance against external reflections. For example, the InAs/GaAs quantum-dot system near the 1.3 μm showed high endurance against external feedback [90]. However, quantum-dots remain difficult to grow for certain materials and wavelengths. The demonstration of the improvement of the feedback sensitivity in our lasers illustrates that this approach of utilizing the high-reflectivity mirrors, enabled by the reduction of the intrinsic loss of the laser, can be applied to any lasers with a different material system to increase resistance against external feedback. Combined with the use of the low linewidth enhancement factor, this approach will create a laser which can further withstand external reflections.

In conclusion, we demonstrated the high immunity of the high-coherence Si/III-V lasers to external reflections by investigating the fringe visibility, the RF intensity noise, and the optical spectrum of the lasers in the presence of feedback. The lasers exhibited a feedback insensitivity which is larger by 25 dB compared to conventional III-V lasers. Furthermore, the lasers possess a low relaxation resonance frequency, as low as hundreds of MHz, thus suppressing high-frequency noise and amplitude/phase coupling at RF frequencies above $\sim 1\text{GHz}$. This was achieved through the use of the low-loss resonator and the reduction of the intrinsic loss in the laser cavity through transverse modal engineering. Consequently, the increased intrinsic Q-factor of the laser enabled the use of high-reflectivity mirrors, without sacrificing the laser output power.

The combination of this approach and the use of a material with a low linewidth enhancement factor α would yield a laser that is highly resistant against external reflections, eliminating the need to use costly optical isolators.

Appendix A

FABRICATION

This appendix presents the fabrication procedures for the heterogeneous Si/InP lasers.

A.1 Si resonator fabrication

The fabrication procedure for the Si resonator fabrication is shown in Figure A.14. The high-Q modegap grating Si resonators were fabricated using SOI wafers. Eight inch SOI wafers with a 700 nm Si layer (resistivity: p-doped Boron, 14-22 $\Omega \cdot \text{cm}$) and a 1 μm buried SiO₂ (BOX) layer were purchased from Soitec (Peabody, MA, USA). The Si layer on the SOI wafer used in this work was thinned down to 500 nm by thermal oxidation, yielding a 400 nm thermal oxide layer on top of the Si. Then, the wafers were diced into chips (9 cm \times 18 cm), and covered with the PMMA photoresist for surface protection.

The photoresist on the chip surface was removed by cleaning with a solvent (acetone/isopropyl alcohol). The organic compounds on the sample surface were cleaned using a piranha solution, a mixture of H₂SO₄/H₂O₂ with a volume ratio of 3:1. Then, the 400 nm thermal oxide layer on top of the Si was thinned down to 50–150 nm, depending on the laser design, using a HF solution (Buffer HF Improved). The etch rate was approximately 100 nm/min. The thickness of the remaining thermal oxide layer was measured using the spectral reflectance-based thickness measurement tool (Filmetrics model F40).

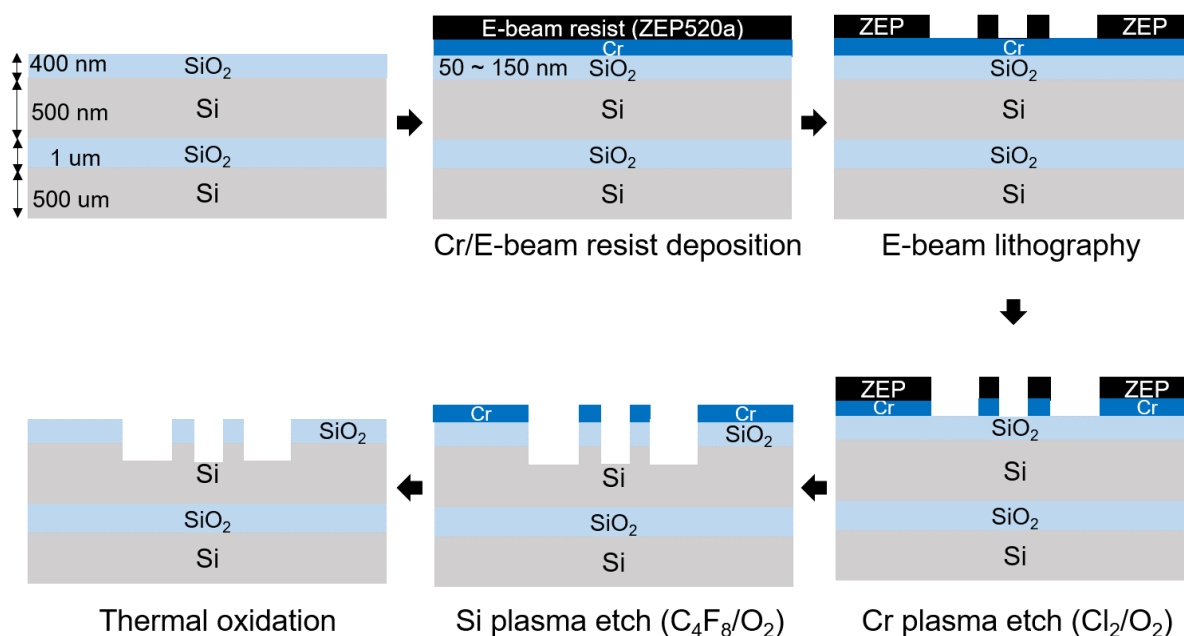


Figure A.14 A fabrication procedure for high-Q modegap grating Si resonator

To etch Si, we used two etch masks to minimize the etch rate difference between the waveguide trench and the grating region. As shown in Figure A.15, a thick electron-beam (e-beam) resist can cause a lag in the etch rate while forming the patterns into Si, especially for the regions that have a high aspect ratio, i.e., grating holes in this case. This effect, called aspect ratio dependent etching (ARDE), is attributed to the poor transport of the etchants into the trenches. The thicker the mask is, the more difficult for the etchants to reach the trench bottom and for the byproducts to escape [91, 92]. To overcome this ARDE effect, we used a thin chrome (Cr) hard mask, instead of the 450 nm e-beam resist, as a final mask to transfer the patterns into the SiO₂ and Si. The Cr hard mask provides a good etch selectivity to SiO₂ of about 32:1 [93], which imply that 10 nm of Cr is sufficient for etching 150 nm SiO₂ and 60 nm Si (the grating depth target, as described in Table 3.1. 2D Si waveguide design parameters) in our waveguides. We deposited a 20 nm Cr layer on our SOI chip using an e-beam evaporator (CHA Industries Mark 40).

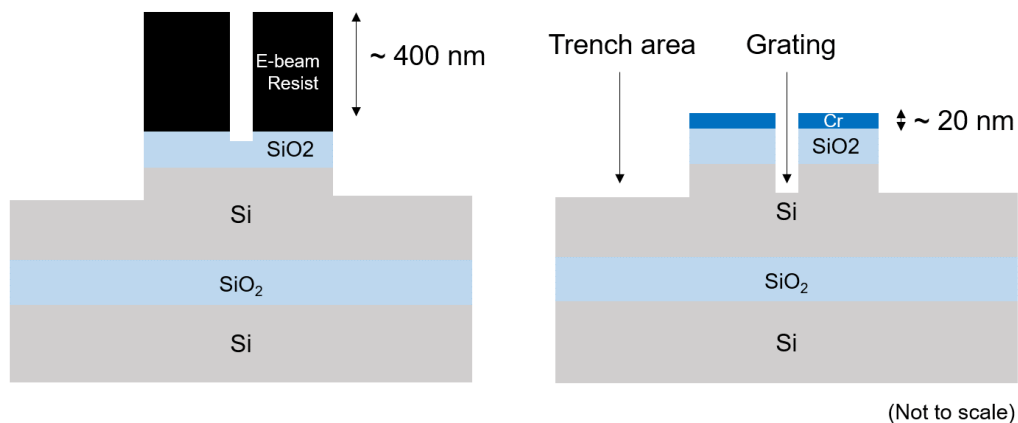
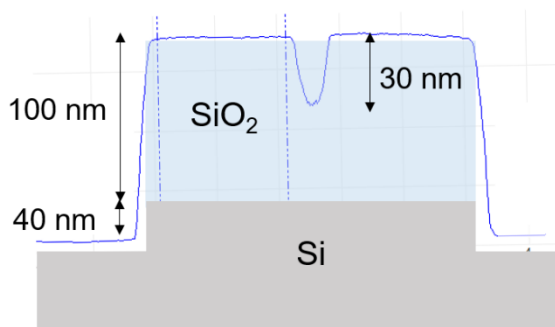
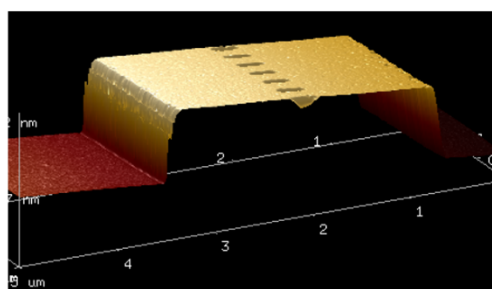


Figure A.15 Aspect ratio dependent etching causes etch lag in the grating region, when etched with the 400 nm e-beam resist. This etch lag in the high aspect ratio region can be avoided by using the thin 20 nm Cr hard mask.

Si etching with e-beam mask (450 nm)



Si etching with Cr mask (20 nm)

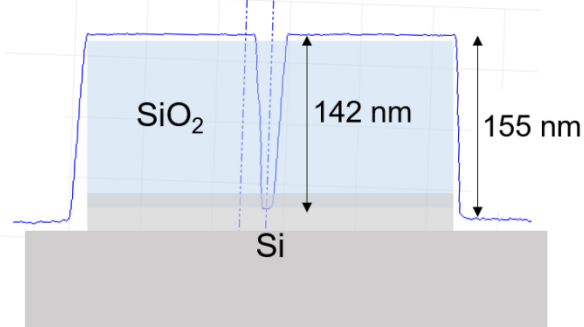
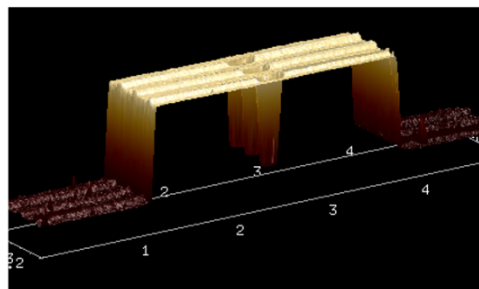


Figure A.3 Atomic force microscope measurement showing the etch depth in the waveguide trench and the grating region, when etched with the 450 nm e-beam mask and the 20 nm Cr hard mask. The right figure shows that using Cr hard mask yields small etch depth difference between the waveguide trench and the grating region.

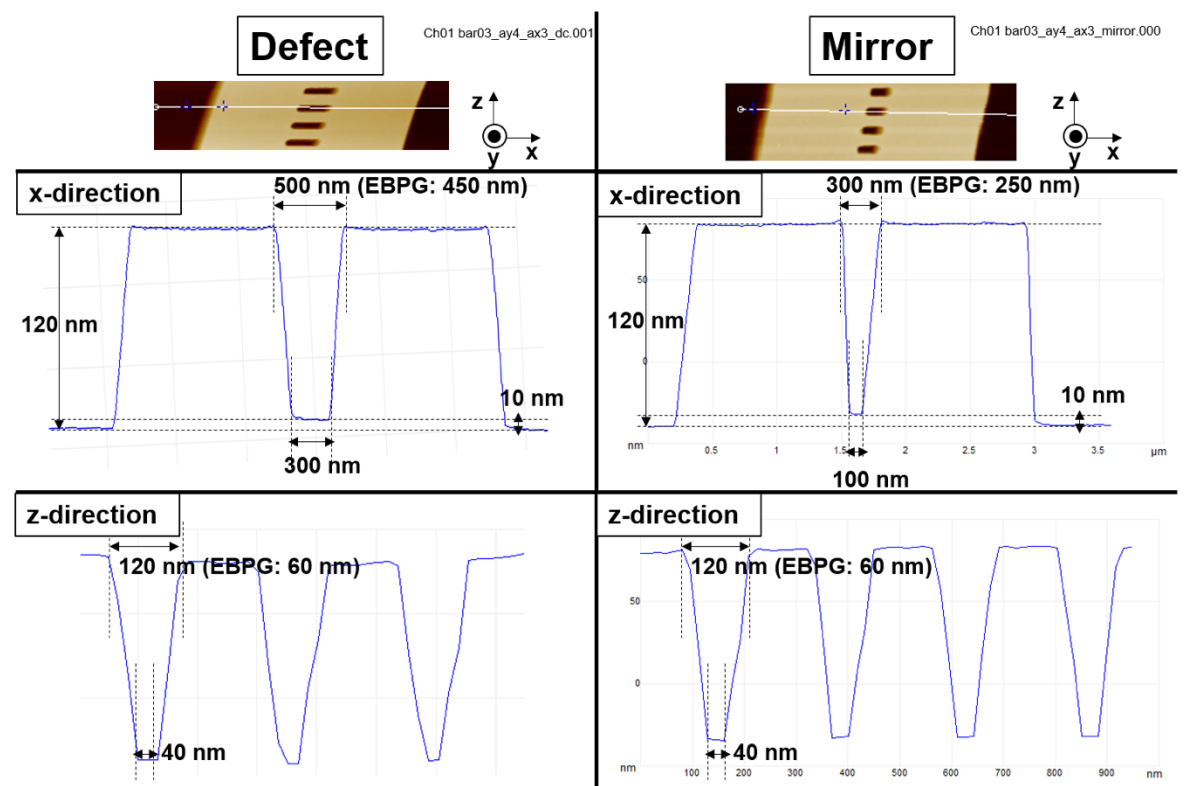


Figure A.4 Atomic force microscope measurement for the waveguides in the defect (left figure) and mirror section (right figure). The waveguide is etched with the Cr hard mask.

Figure A.3 Atomic force microscope measurement showing the etch depth in the waveguide trench and the grating region, when etched with the 450 nm e-beam mask and the 20 nm Cr hard mask. The right figure shows that using Cr hard mask yields small etch depth difference between the waveguide trench and the grating region. shows the atomic force microscopy (AFM) measurement for the waveguides in the mirror section after Si etching. The ARDE effect was severe when the etching was performed using the 450 nm e-beam mask, whereas the 20 nm Cr hard mask yielded a small etch depth difference of approximately 10 nm between the waveguide trench and the grating region.

Figure A.4 Atomic force microscope measurement for the waveguides in the defect (left figure) and mirror section shows the AFM measurements for the waveguides in the defect and mirror section. While etching 60 nm of SiO_2 and 60 nm of Si, the grating holes show 200 nm difference in diameter in the x-direction between the top and the bottom of the hole, and 80 nm difference between the top and the bottom in the wave-propagating z-direction. These differences are

identical in both the defect and mirror sections. After Cr deposition, approximately 450 nm of positive e-beam resist (ZEP520A [94]) was deposited on top of the Cr.

The waveguide trench and the grating patterns were written using e-beam lithography (Vistec/Leica EBPG 5000+). Patterns were divided into a ‘sleeve’ part, which were written with a beam current of 300 pA and a beam step size of 2.5 nm, and a ‘bulk’ part, which were written with a beam current of 10 nA and a beam step size of 10 nm. The sleeve part writes the gratings and the edge part of the waveguide trenches, and the bulk writes the remaining part of the waveguide trench area. The clearing dose of the spun-on e-beam resist was approximately $270 \mu\text{C}/\text{cm}^2$, but a slightly higher dose was used to reduce the roughness on the resist sidewalls with over-exposure [95, 96].

Then, patterns were transferred into Cr using an inductively coupled plasma reactive ion etching (ICP-RIE, Oxford III-V Etcher) with Cl_2/O_2 chemistry [93]. Cr etching took approximately 8 minutes, leaving ~ 80 nm of e-beam resist on top of the Cr. The remaining e-beam resist was removed by O_2 plasma using the same etcher. The patterns were then transferred into SiO_2 and Si with $\text{C}_4\text{F}_8/\text{O}_2$ gases [93]. A large etch rate variation was observed and careful calibration of the etch rate is required in this step. The Cr hard mask was removed using the wet Cr etchant (CR-7S) [97].

After cycles of thorough cleaning (Piranha/ O_2 plasma), the Si chip was oxidized using dry thermal oxidation for 15 min and annealed with N_2 for 30 minutes at 1000°C (Tystar Tytan) to further reduce the sidewall roughness [98, 99, 100].

Every step of the fabrication broadens the grating holes. The design patterns were calibrated using a careful SEM characterization to account for this effect, thus enabling the precise fabrication of holes with the target z-direction diameter of 120 nm.

Figure A.16 SEM image of the fabricated grating in-plane Si resonator. shows the scanning electron microscope (SEM) image of the fabricated 1D grating in-plane Si resonator. In Figure A.4 Atomic force microscope measurement for the waveguides in the defect (left figure) and mirror section (right figure). The waveguide is etched with the Cr hard mask., a grating hole with a 120 nm in diameter, which is our design target, was obtained when we write 60 nm in the e-beam lithography pattern. Therefore, we decide to e-beam write 60 nm to achieve the 120 nm diameter on the surface of the waveguide. The transmission spectrum of the fabricated resonator is given in Figure 3.5.

More detailed description for the process condition can be found in [101, 42, 102].

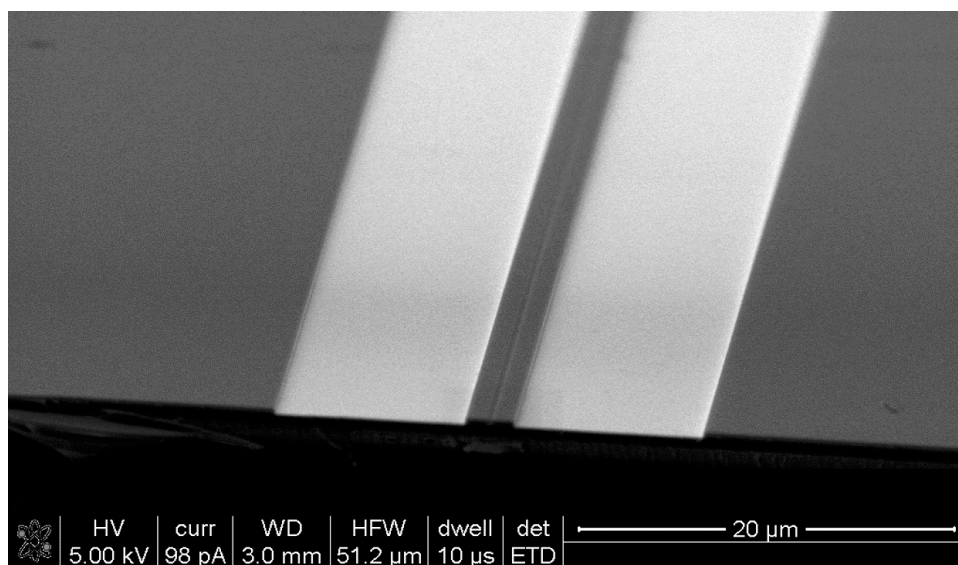
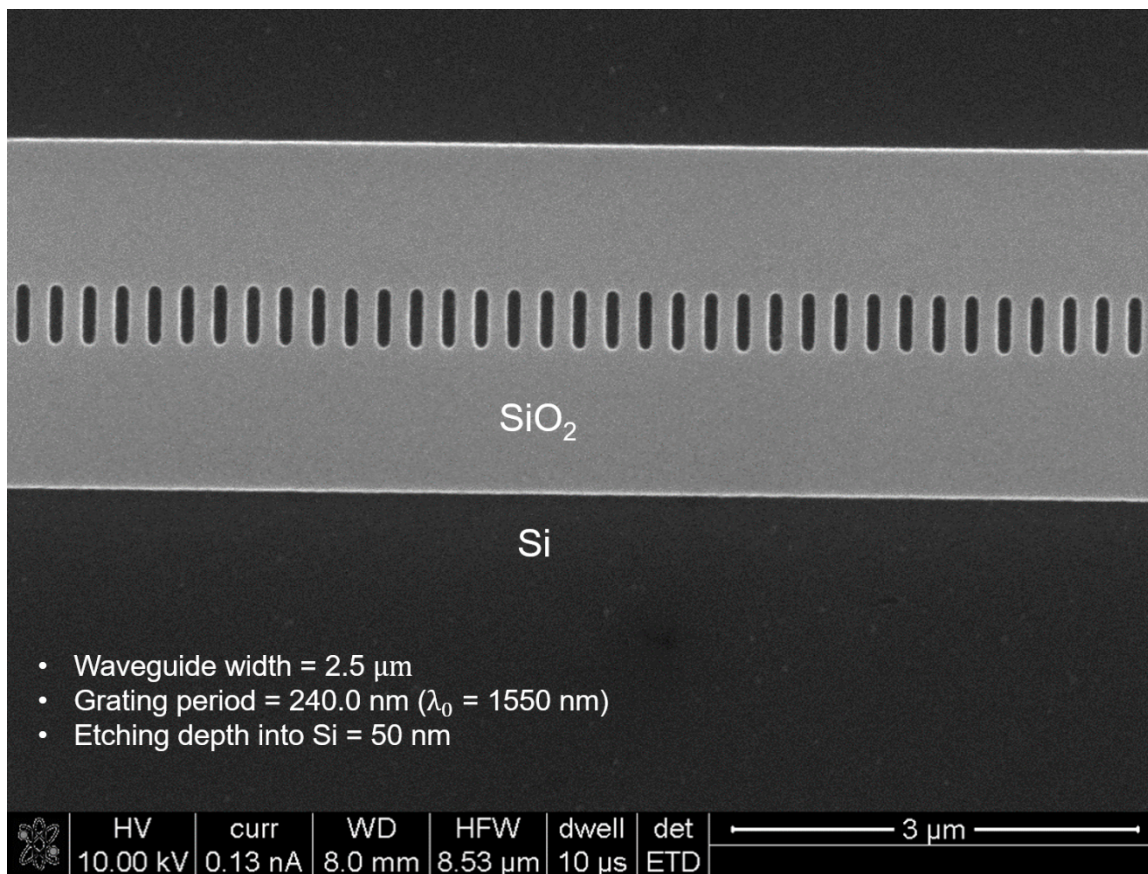


Figure A.16 SEM image of the fabricated grating in-plane Si resonator.

A.2 III-V fabrication

The structure of the III-V epi-wafer used for our laser is shown in Table A.1 The structure. The wafer was custom grown by Landmark (Tainan City, Taiwan).

Name	Material	Thickness (nm)	Doping (cm-3)	Strain	PL (nm)	Bandgap (eV)	Refractive index
Bonding layer	InP	10	n = 1E18			1.34	3.1
Superlattice	InP	7.5	n = 1E18			1.34	3.1
	In _{0.85} Ga _{0.15} As _{0.327} P _{0.673}	7.5	n = 1E18		1100	1.13	3.25
	InP	7.5	n = 1E18			1.34	3.1
	In _{0.85} Ga _{0.15} As _{0.327} P _{0.673}	7.5	n = 1E18			1.13	3.25
n-cladding /contact	InP	110	n = 1E18			1.34	3.1
SCL outer	InGaAsP	40	undoped		1150+/-10	1.08	3.33
SCL Inner	InGaAsP	40	undoped		1250+/-10	0.99	3.3755
QW	InGaAsP (x5)	7 per well	undoped	1% compressive strain	1550+/- 10	0.83	3.53
Barriers	InGaAsP (x4)	10 per barrier	undoped		1250+/- 10	0.99	3.3755
SCL Inner	1.25Q InGaAsP	40	undoped		1250+/-10	0.99	3.3755
SCL outer	1.15Q InGaAsP	40	undoped		1150+/-10	1.08	3.33
p-cladding	InP	1500	p = 5E17 -> 1E18			1.34	3.1
p-contact	In _{0.53} Ga _{0.47} As	200	Highest dopant (p ~> 1E19)			0.77	3.43
Buffer	InP	500	Highest dopant (p ~> 1.5E18)				3.1
Substrate	InP		n-doped (or intrinsic)				3.1

Table A.1 The structure of the III-V epi-wafer used in this thesis.

To bond the III-V InP wafer to Si/SiO₂, we used the plasma-assisted low temperature direct (molecular) bonding technique [103, 104, 105]. There are many other bonding methods, such as metal bonding [106, 107], and adhesive bonding [108, 109], but we used the direct bonding technique mostly for the precise control of the spacing between Si and III-V. Direct bonding between Si and InP was realized using high mechanically-applied pressure in vacuum at 285°C for 5 hours in a wafer bonder (Suss SB6L). For removal of the InP substrate, we introduced a physical lapping method to grind away most of the InP substrate. The final 50 μm InP substrate was removed using hydrochloric acid (HCl). Figure A.17 An image showing the laser chip after bonding step and subsequent substrate removal step. shows the image of the bonded Si/III-V chip after removal of the III-V substrate.

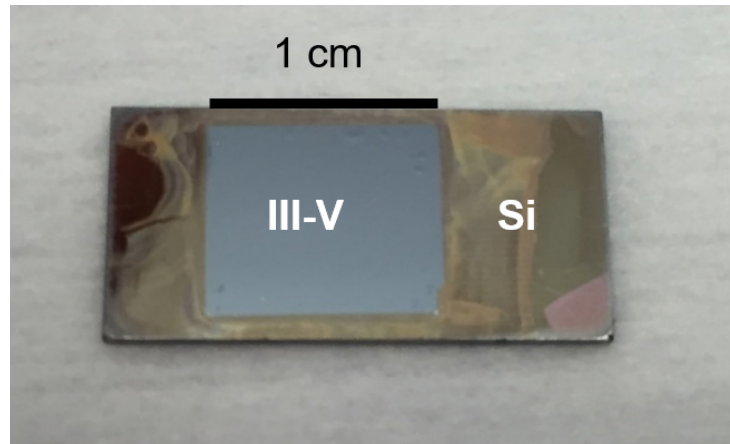


Figure A.17 An image showing the laser chip after bonding step and subsequent substrate removal step.

The III-V mesa and metal contacts are tens of micron wide, whereas the optical mode in our waveguide is a $\sim 2 \mu\text{m}$ wide. To obtain a high injection efficiency, the injection of carriers into the active region at the immediate vicinity of the lasing mode is necessary. In this thesis, an efficient current injection was achieved using two different methods: ion implantation and oxide-confinement.

A.2.1 Mesa formation using ion implantation

Figure A.7 A schematic of heterogeneous Si/III-V lasers where III-V mesa structure is made using ion-implantation. shows a schematic diagram of heterogeneous Si/III-V lasers in which the current injection is realized using ion implantation. The ion-implanted region becomes highly electrically resistant, making it possible to confine the injected current to the central region of the mesa.

The III-V mesa fabrication procedure using ion implantation is shown in Figure A.8 III-V mesa fabrication procedure using ion implantation.. Implantation was outsourced and performed by Kroko (Tustin, CA, USA). After ion implantation, the photoresist mask becomes sticky and hard to remove. Thorough solvent cleaning along with O_2 plasma was necessary to strip the resist. Ti/Pt/Au (30/50/300 nm) and Ni/Ge/Au/Ni/Au (5/20/20/20/225 nm) were used for the p- and n-metal contacts, respectively. A $65 \mu\text{m}$ wide photoresist mask was used to etch the InGaAs p-contact layer with Piranha ($\text{H}_2\text{SO}_4:\text{H}_2\text{O}_2:\text{H}_2\text{O} = 5 \text{ mL}:15 \text{ mL}:50 \text{ mL}$), while a single $80 \mu\text{m}$ wide

photoresist mask is used to etch both the p-InP cladding and InGaAsP QW layers with HCl and Piranha solution, respectively. The fabricated laser structure using ion implantation is shown in Figure A.18 SEM image of the fabricated laser using ion implantation.. A more detailed description of the mesa fabrication procedure using ion implantation can be found in [43, 105, 106].

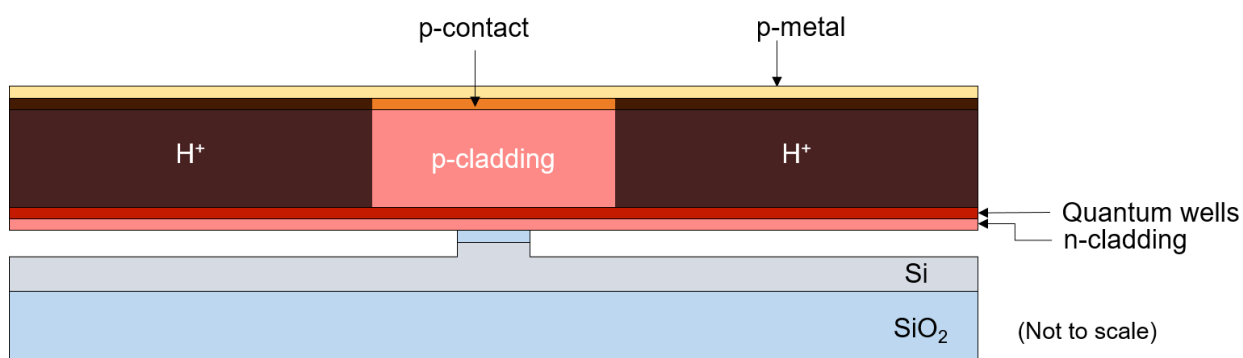


Figure A.7 A schematic of heterogeneous Si/III-V lasers where III-V mesa structure is made using ion-implantation.

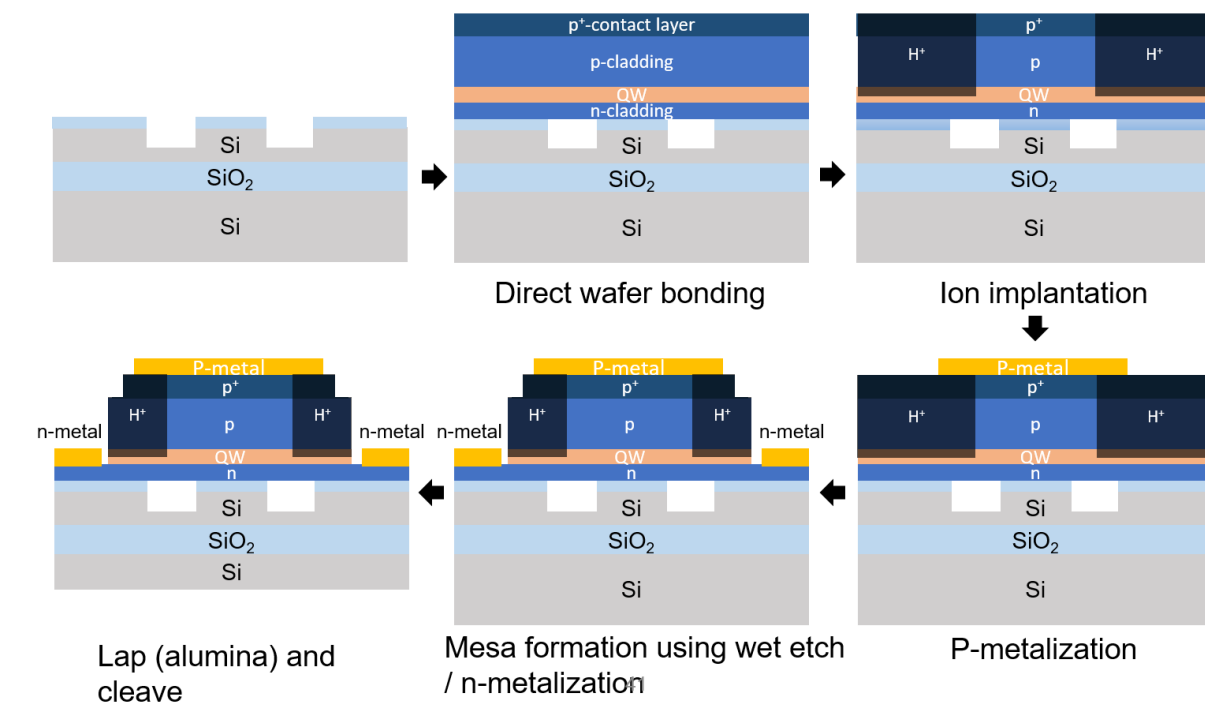


Figure A.8 III-V mesa fabrication procedure using ion implantation.



Figure A.18 SEM image of the fabricated laser using ion implantation.

A.2.2 Mesa formation using oxide-confinement

The III-V mesa structure was also formed using a different technique, which we call the oxide-confinement method, as shown in Figure A.19 Schematic diagram of heterogeneous Si/III-V lasers where III-V mesa structure is made using oxide-confinement method. In this method, the current injecting structure was directly etched using wet processes to define the electrical current path. Subsequently, SiO₂ was deposited over the mesa and a window was opened only over the central

pillar to provide the electrical connection between the III-V and the p-metal contact. The neighboring pillars provided the mechanical support when electrical probes were used to make contact with the laser.

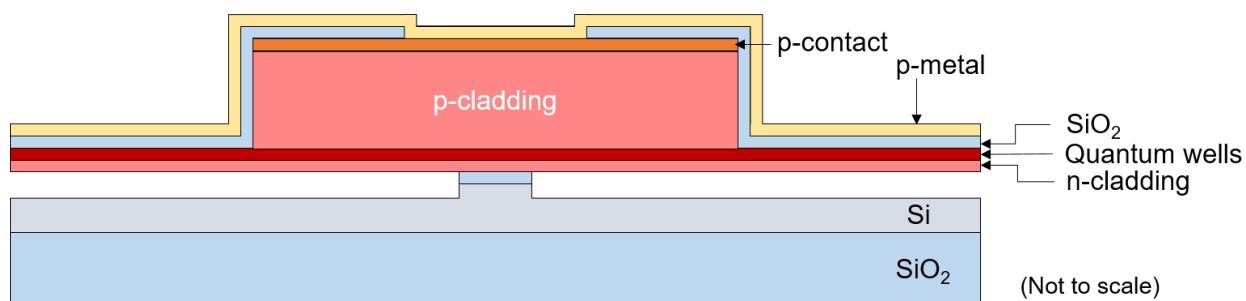


Figure A.19 Schematic diagram of heterogeneous Si/III-V lasers where III-V mesa structure is made using oxide-confinement method.

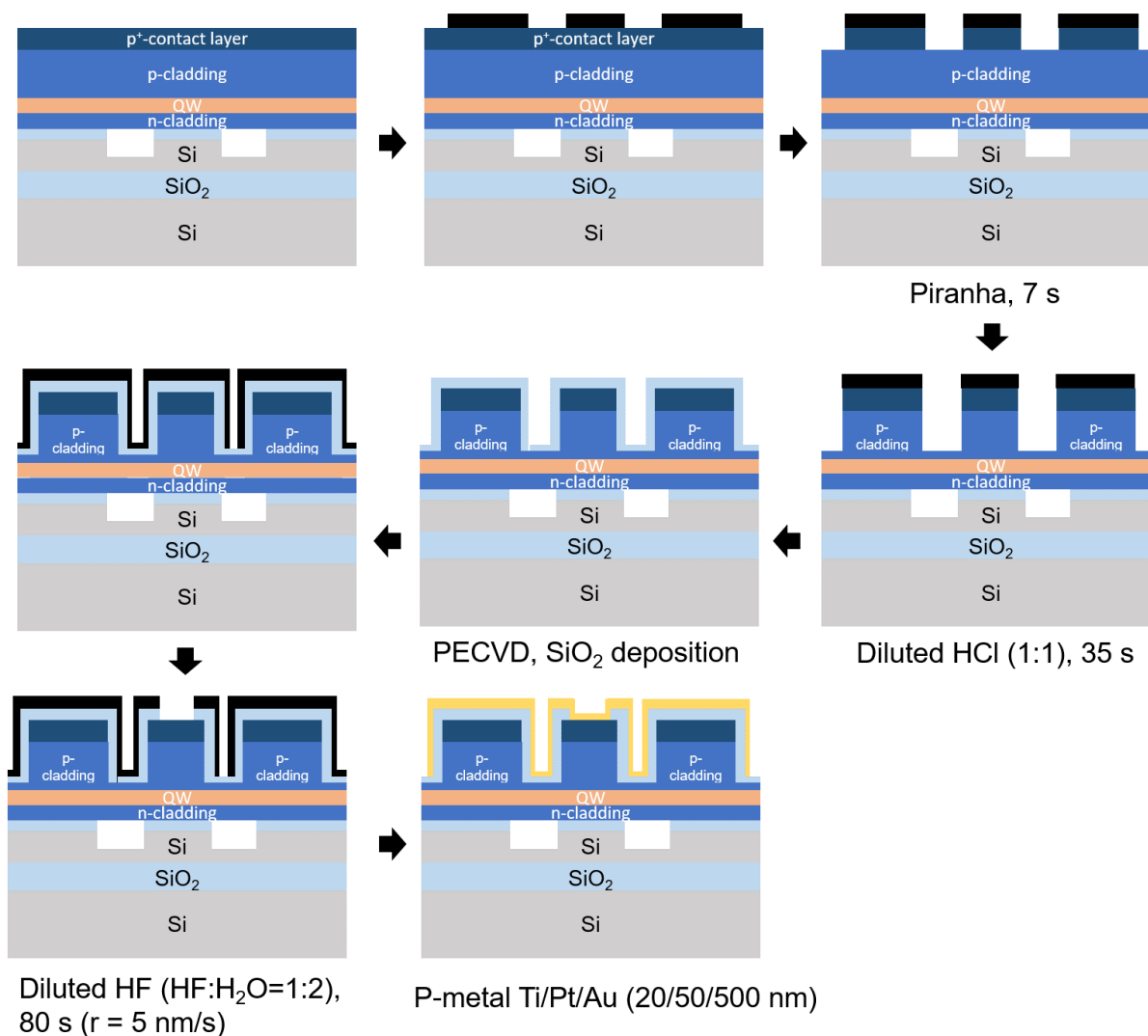


Figure A.20 III-V mesa fabrication procedure using oxide-confinement.

The oxide-confinement method was demonstrated on edge-emitting lasers [110], and vertical-cavity surface-emitting laser (VCSEL) [111, 112]. To our knowledge, this is the first demonstration of the oxide-confinement method in a heterogeneously integrated Si/III-V platform.

Figure A.20 III-V mesa fabrication procedure using oxide-confinement. shows the III-V mesa fabrication procedure using the oxide-confinement method. To create the oxide-confined mesa structure, the III-V mesa was defined by wet etching the mesa with three pillars with a depth of 1.4 μm ; the central pillar had a width of 6 μm and the two adjacent pillars had a width of 20 μm for mechanical support on either side. The central pillar was used to inject carriers into the QWs directly above the waveguide to provide the laser gain. The mesa etch was stopped above the QWs

so that defects introduced by etching are kept away from the active region [113]. An SiO_2 layer was deposited by plasma-enhanced chemical vapor deposition (PECVD) to provide electrical isolation between the different pillars of the mesa. A $4\ \mu\text{m}$ wide window was opened in the SiO_2 on the central pillar using photolithography and etched with HF to enable electrical contact between the metal and the III-V material. Then, the p- and n-metal contacts with the same structure described in were deposited. Figure A.21 shows a SEM image of the cross section of the mesa of the fabricated laser, in which the central mesa and the waveguide can be seen. The successful connection between the p-metal and the p-InGaAs contact layer through the opened window can be confirmed from the image.

The wet etching recipe for each layer of III-V and the metal contact structure was the same as that described in Section A.2.1. The detailed conditions for the processes can be found in [42, 101, 102].

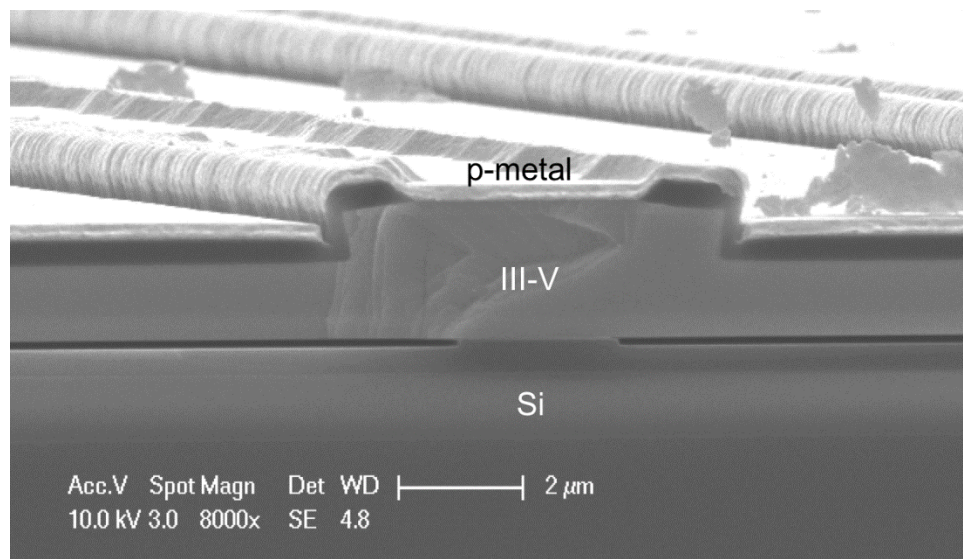


Figure A.21 SEM image of the fabricated laser using oxide-confinement method.

Appendix B

BIOSENSING

Here we describe proposals, fabrications and experimentation of employing an on-chip integrated differential optical microring refractive index sensing platform. This platform leverages laminar flow conditions, close spacing between a sensing and a reference resonator, and sharing the same microfluidic channel which allows the two resonators to experience similar environmental disturbances, such as temperature fluctuations and fluidic-induced transients, achieving reliable and sensitive sensing performance. We obtain a noise floor of 80.0 MHz (0.3 pm) and a bulk refractive index sensitivity of 17.0 THz per refractive index unit (RIU) (64.2 nm/RIU), achieving a limit of detection of 1.4×10^{-5} RIU in a 30 minute and an 8°C window.

B.1 Biosensing using optical microresonators

Optical microresonators, compatible with CMOS technologies and easily incorporated with microfluidics, are good candidates for integration into portable medical diagnostic devices and commercial bench-top systems for chemical/biological analysis [114, 115, 116]. Microring resonators are promising optical sensing devices, due to their high sensitivity to environmental refractive index changes and single-mode of operation. In these devices, the light propagates in the form of a traveling wave with resonance wavelengths, $\lambda = 2\pi R n_{\text{eff}}/m$ (R : the radius of the resonant cavity, n_{eff} : the effective refractive index experienced by the resonant mode, m : the azimuthal mode number). A change in the refractive index of the cladding, caused by analytes binding to the functionalized surface of the optical resonator, or by analytes in the whole region of a cladding layer, will induce a spectral shift in the resonance wavelength [117].

However, environmental disturbances, such as temperature drift, flow-induced drift, and laser drift, cause spurious changes in the resonance wavelength and must be accounted for to enhance the limit of detection of the sensing system. A differential measurement can reject common mode noise by including an additional reference resonator to track the undesired drift. An on-chip differential measurement requires the physical separation of the reference resonator from the sensing solution. Current methods include utilizing a reference resonator covered by a perfluoropolymer [114], a SU-8 polymer or a silicon oxide (SiO₂) cladding layer [118], or a

platform where the reference resonator resides in a separate microfluidic channel from the sensing resonators [119].

B.2 Differential sensing based on a laminar flow scheme

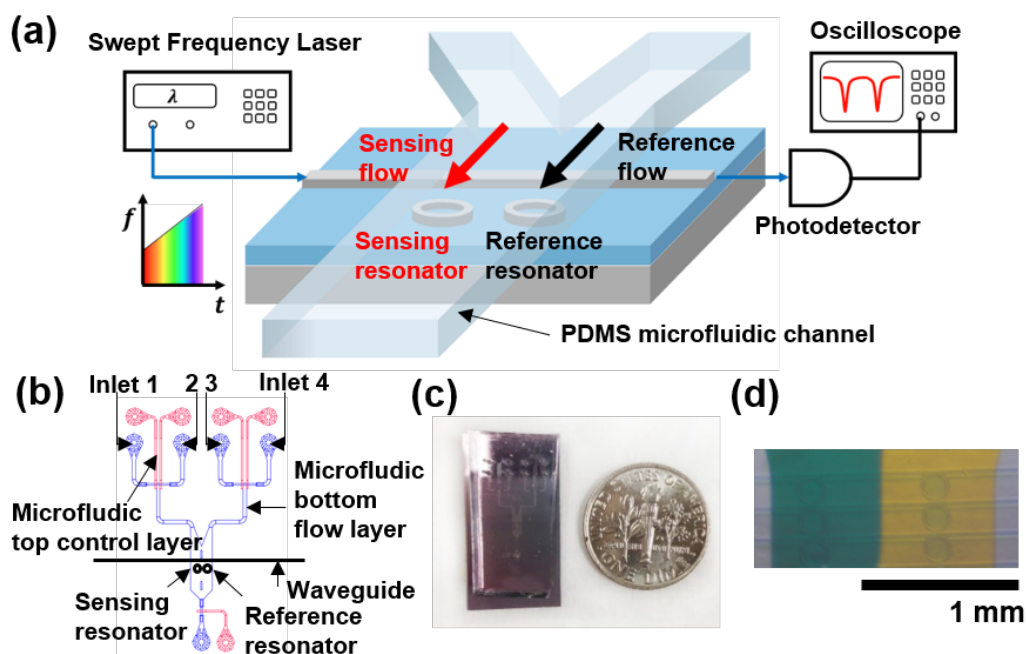


Figure B.22 (a) Schematic view of the proposed platform. (b) Layout of the waveguide-resonator chip shown together with two-layer microfluidic structures. (c) Photograph of (left) the fabricated device where the Si_3N_4 waveguide-integrated microring resonator chip is bonded to the PDMS microfluidic device, (right) a dime shown for scale. (d) Photograph showing the laminar flow of the two different dye solutions flowing onto three pairs of resonators, with no disruption between two fluid layers.

We present a new on-chip differential refractive index sensing platform that leverages laminar flow conditions between the non-mixing solutions. The two resonators, one used for sensing and the other for reference, are exposed to an aqueous environment in one common microfluidic channel. Two solutions, one containing the sample of interest and the other acting as a reference, flow in the common microfluidic channel, and the laminar flow maintains the composition of the two fluid streams as they pass by the sensing and the reference resonators separated by more than the diffusion length (~ 10 s of μm) of the analyte molecules within the laminar flow. The differential

measurement is then realized by tracking the difference between resonance wavelength of the sensing and reference resonators (Figure B.22 (a)).

In this platform, since the resonators are placed in close proximity to each other in the same microfluidic channel, environmental disturbances, such as temperature fluctuations, flow-induced transients, and drifts induced by interaction of the microfluidic channel with liquids (such as the slow drift caused by solvent permeation into microfluidic channel walls [120]), have similar, ideally identical, effects on both resonators. This results in stable and sensitive sensing without requiring external stabilization. The close spacing between the resonators leads to a compact device and also improves resonator-to-resonator fabrication variation tolerance in waveguide width, height, and coupling gap. This results in uniform resonator responsivity, and eliminates the need for time-consuming calibration of individual resonator responsivities.

The condition of each solution flowing over each resonator can also affect sensing performance since they are in direct contact. It is difficult to precisely control the temperature of each solution. As we see later in this Letter, a difference of 1°C corresponds to approximately 0.6 GHz in this platform, or equivalently 3.5×10^{-5} RIU in the sensing solution, which is 2.5 times larger than the reported limit of detection in this platform. To address this limitation, our proposed platform includes a 950 μm microfluidic equilibration region before the two fluids reach their respective resonators. This region, where the solutions are in contact with each other while still satisfying laminar flow conditions, helps reduce the temperature and pressure differences between the two fluids, and thus, between the two resonators.

Our platform eliminates the need to cover the reference resonator and, thus, removes associated fabrication complexities. While covering the reference resonator with a cladding layer and then opening sensing windows is achievable, several process issues arise that can complicate its development. First, hard claddings (oxide-based) impose fabrication challenges due to the poor dry etch selectivity between the cladding layer and sensing resonator [118].

Imperfect control of the etching depth over the sensing window would lead to sensing resonators with different optical properties.

Second, new materials added to the surface of the device limit the range of compatible chemicals and processes for surface treatment. For example, once a polymer cladding is deposited, it is difficult to clean, surface-activate, or recycle resonators with harsh cleaning solutions during the development of a surface functionalization protocol [121]. By overcoming these challenges

and also increasing the stability and sensitivity, we believe that our new platform offers a promising starting point for future development of laminar flow-based differential sensing measurements.

B.3 Implementation of the platform

Fabrication of the optical microring resonators

Figure B.22 (b) shows a schematic of the platform where a waveguide-integrated resonator chip is shown together with a two-layer microfluidic layout. Two 140 μm diameter, 1 μm width optical microring resonators are positioned with a center-to-center spacing of 800 μm . They are fabricated on a 250 nm thick silicon nitride (Si_3N_4) layer on top of 6 μm thick SiO_2 on a silicon handle. The 1 μm wide waveguides and the microrings with a 400 nm coupling gap are patterned using electron beam lithography on electron beam resist, ZEP520A. The patterns are transferred to the Si_3N_4 layer using low DC-bias, inductively-coupled plasma reactive-ion etch (ICP-RIE) with $\text{SF}_6/\text{C}_4\text{F}_8$ chemistry.

Implementation of microfluidics

For liquid delivery, a microfluidic polydimethylsiloxane (PDMS) device is bonded on top of the Si_3N_4 layer. The two-layer microfluidic structure consists of a bottom flow layer and a top control layer, and incorporates four inlets and one outlet, each with a corresponding control valve. The two inlets to the left are used to deliver solutions to the sensing resonator, while the two inlets to the right supply flow to the reference resonator. Figure B.22 (c) shows a photograph of the fabricated platform, in which the Si_3N_4 waveguide-resonator chip is bonded to the two-layer PDMS device. Continuous pumping of the solutions and switching of the valves between the different inlets is achieved by computer-controlled pressurized solenoid valves [122]. The pressure driving the liquid flow is set to 41 kPa, whereas that used to actuate the control valves is set to 151 kPa.

To illustrate the laminar flow achieved on this device, we introduce two different dye solutions from two inlets into one common flow channel, which is 1.3 mm wide and 22 μm tall. Figure B.22 (d) shows the established dual laminar flow, demonstrating successful delivery of the different solutions to the sensing and reference resonators.

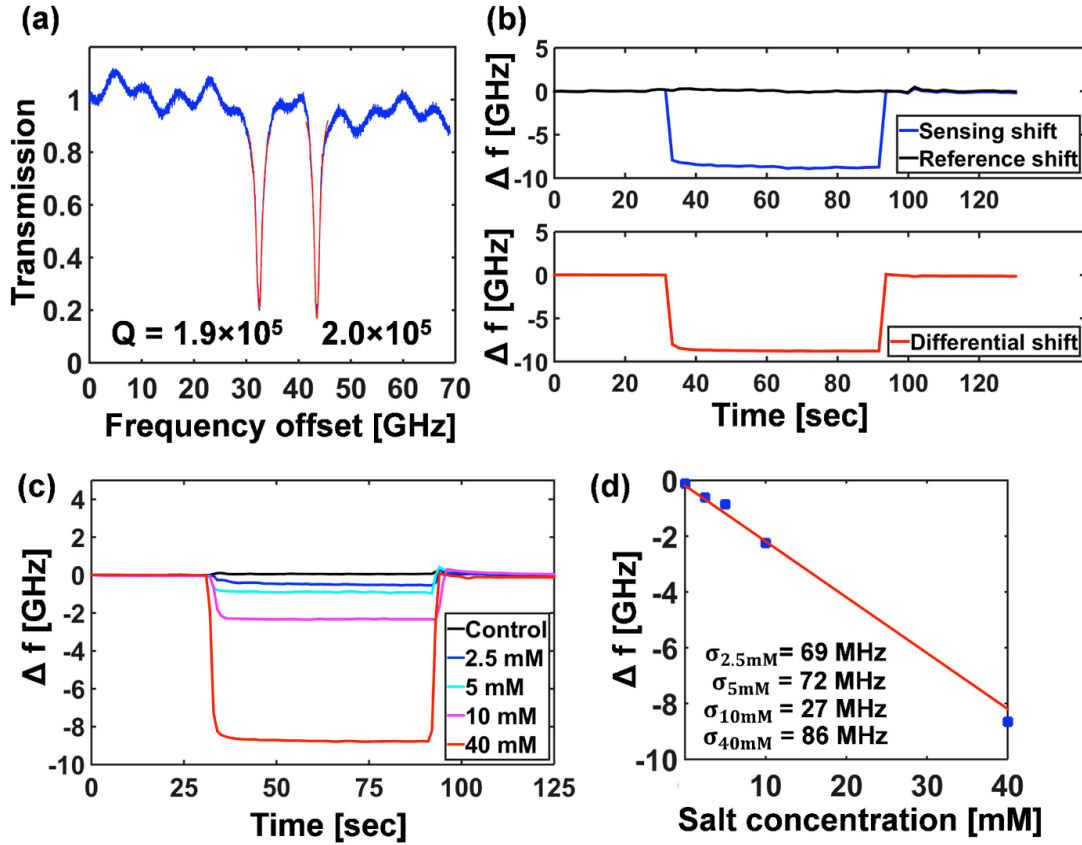


Figure B.23 (a) Transmission spectrum of two high-Q microring resonators in water measured at 1064 nm (blue), the Lorentzian fits are shown in red. (b) sensing, reference, and differential frequency shift versus time from a 40 mM NaCl solution at constant stage temperature of 26°C. (c) differential shift versus time at various NaCl concentrations. (d) Differential shift versus NaCl concentrations at 26°C.

Characterization of the optical resonators

The microring resonators are characterized using a 1064 nm vertical-cavity surface-emitting (VCSEL) based optoelectronic linearly swept frequency laser with an optical frequency excursion of 400 GHz in 2 ms, which is coupled into the waveguide from free space optics. The feedback scheme described in [47] ensures that the laser sweeps at a fixed linear chirp rate for the entire sensing experiment. We achieve high Q-factors of the microring resonators in aqueous environments due to the transparency of Si_3N_4 and low water absorption at 1064 nm [123], measured to be $Q = 1.9 \times 10^5$ and 2.0×10^5 for the sensing and reference resonator, respectively (Figure B.23 (a)). The relatively large diameter of 140 μm of the microring resonators not only enables high Q-factors but also give the resonators a free spectral range (FSR) small enough to be

spectrally scanned by a VCSEL through current injection. This removes the need for expensive, large-bandwidth, slow scanning mechanical tunable lasers.

B.4 NaCl bulk sensing experiments

To demonstrate the sensing ability of this platform, we flow sequentially diluted sodium chloride (NaCl) solutions. In this experiment, the temperature of the resonator chip is fixed at 26°C using a Peltier thermoelectric cooler (TEC). The resonator chip is attached to the copper block using thermally conductive adhesive transfer tape and the stage temperature is monitored using a thermistor attached to the copper block.

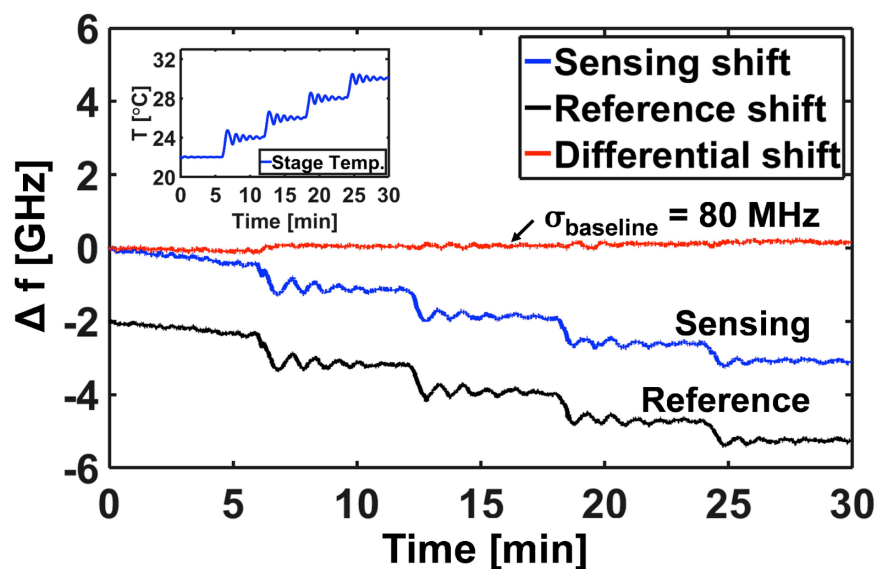


Figure B.24 Sensing, reference, and differential frequency shifts versus time while continuously flowing DI water from two inlets to the sensing and reference resonator as the temperature of stage is adjusted from 22 to 30°C, 2 GHz of offset is applied to the reference shift to distinguish it from the sensing shift. (inset) monitored stage temperature.

First, we establish the baseline by continuously flowing deionized (DI) water from inlet 1 and inlet 4 to the sensing and reference resonator, respectively. Next, we switch the sensing flow to inlet 2, which is connected to the NaCl solution, while maintaining the reference flow of DI water. For recovery, we switch back the sensing flow to inlet 1 (DI water). The resonance frequency of the sensing resonator, reference resonator, and their difference is monitored simultaneously by the swept VCSEL. The resonance frequency shifts from 40 mM NaCl solution are plotted in Figure

B.23 (b). The differential shifts at concentrations of 2.5, 5, 10, and 40 mM, are measured and plotted in Figure B.23 (c). We perform 5 to 10 cycles of the same experiment at each concentration and the frequency shifts from all cycles are plotted in Figure B.23 (d). Using a refractive index change of 0.0018 per 1% mass (172.8 mM) [124], a bulk sensitivity of -19.2 ± 0.1 THz/RIU (72.6 ± 0.3 nm/RIU) is extracted by linear regression. The standard deviations at each of the concentrations ($\sigma_{2.5\text{mM}} = 69$, $\sigma_{5\text{mM}} = 72$, $\sigma_{10\text{mM}} = 27$, and $\sigma_{40\text{mM}} = 86$ MHz) demonstrate excellent sensing repeatability from cycle to cycle. The two-layer microfluidic structure with on-chip valves allows the sensing signal to reach steady-state in less than 10 seconds after valve switching due to low dead volume in the microfluidic plumbing.

To study the total noise of the platform in a temperature-varying environment, we increase the temperature of the stage over an 8°C window, from 22 to 30°C , in steps of 2°C , while flowing DI water from inlet 1 and 4 to the sensing and reference resonator, respectively. To automate and monitor the change of the stage temperature, a computer-controlled temperature controller (LDC-3724) is used instead of the TEC.

The inset to Figure B.24 shows the monitored stage temperature. After applying 2 GHz of offset to the reference shift to distinguish it from the sensing shift, we plot their resonance frequency shifts as a function of time in an 8°C window in Figure B.24. It can be seen that, even though the single resonator response follows the stage temperature change, most of the thermal drift is removed in the differential shift. A standard deviation (σ_{baseline}) in the differential frequency shift of 80.0 MHz (0.3 pm) is achieved, as opposed to the ~ 3 GHz shift seen in the individual resonators, and taken to be the total system noise in an 8°C window in the absence of switching transients.

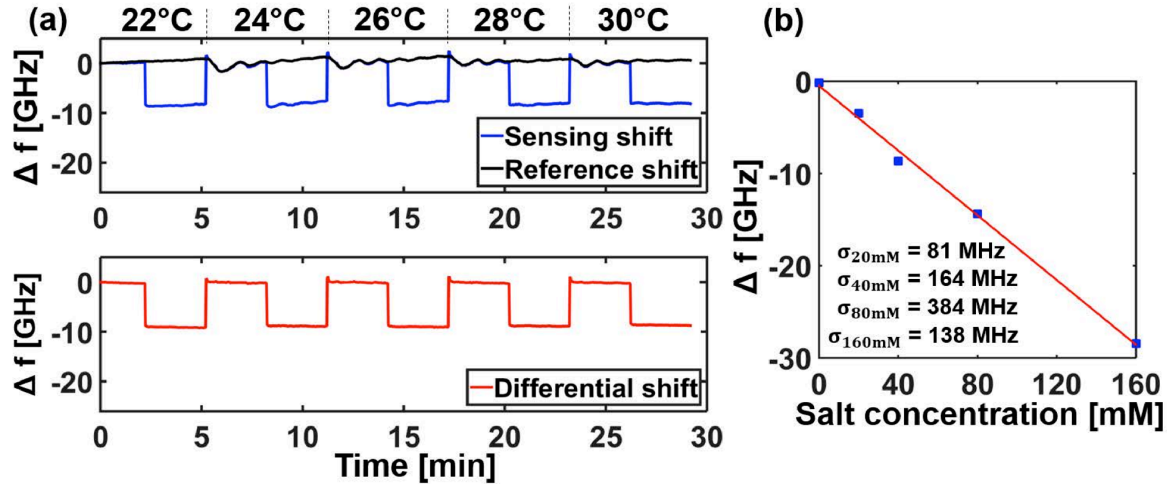


Figure B.25 (a) Sensing, reference, and differential frequency shift versus time from a 40 mM NaCl solution at stage temperature from 22 to 30°C; (b) differential shift from all temperatures at each concentration.

We finally demonstrate the NaCl bulk refractive index sensitivity in a temperature-varying environment. Sequentially diluted NaCl solutions of 20, 40, 80, and 160 mM are measured, as the temperature of the stage is increased from 22 to 30°C. Figure B.4 (a) shows the sensing, reference, and differential frequency shifts at 40 mM NaCl solution. The clean sensing signal in the differential shift is observed through the whole range of temperatures. The decrease of the resonance frequency shift in each of the single resonator response induced by the stage temperature perturbation is not immediately obvious in this specific experiment due to the superimposed slow drift induced by the laser starting frequency jitter and the interaction of the microfluidic channel with the fluids. The differential shifts from all temperatures at each concentration are plotted together with error bars in Figure B.4 (b). A bulk sensitivity of $S = -17.0 \pm 0.2$ THz/RIU (64.2 ± 0.9 nm/RIU) is extracted from the experiments.

The standard deviations of the measurements at each salt concentration ($\sigma_{20\text{mM}} = 81$, $\sigma_{40\text{mM}} = 164$, $\sigma_{80\text{mM}} = 384$, and $\sigma_{160\text{mM}} = 138$ MHz) show excellent sensing uniformity, even in the presence of the stage temperature fluctuations in an 8°C window and switching transients.

Based on the measured data, we compute a practical refractive index limit of detection [129] of $3\sigma_{\text{baseline}} / S = 3 \times 80.0$ [MHz] / 17.0 [THz/RIU] = 1.4×10^{-5} RIU in a 30 minute and an 8°C temperature operating window. This platform thus achieves reliable and sensitive sensing operation while eliminating the need of bulky external active temperature stabilization elements.

B.5 Conclusion

In summary, we have proposed and implemented a new on-chip differential refractive index sensing platform which employs a laminar flow scheme to isolate the reference resonator from the sensing flow. This platform shows excellent performance in removing external drifts, including thermal drift. A bulk sensing capability with refractive index limit of detection of 1.4×10^{-5} RIU was demonstrated in a 30 minute and an 8°C window. We also achieve a switching transient time less than 10 seconds by using a two-layer microfluidic structure with on-chip valves.

The stability and sensitivity of this on-chip, laminar flow, differential refractive index sensing platform make it promising for specific binding biosensing applications, by flowing analyte sample solutions once the optical resonators are functionalized with suitable conjugate reagents. Multiplexing can also be achieved on this platform by having multiple laminar flows containing different solutions of interest in one large microfluidic channel. Because the laminar flow condition between each pair of streams prevents the solutions from mixing, a single reference solution can be used as a global reference.

Furthermore, this laminar flow scheme can be extended to selectively functionalize different resonators. It can be achieved by flowing different binding reagents over different resonators with laminar flow conditions before a sensing step. This enables not only detection of multiple species, but also use of a single sample flow to achieve an even smaller limit of detection. Work toward this integrated, multi-sensing platform is underway.

Funding Information

This research was funded by National Science Foundation (NSF) (IDBR-1152623).

BIBLIOGRAPHY

- [1] W. Matusik and H. Pfister, "3D TV: a scalable system for real-time acquisition, transmission, and autostereoscopic display of dynamic scenes," in *Proceeding SIGGRAPH '04 ACM SIGGRAPH 2004 Papers*, Los Angeles, California, 2004.
- [2] J. Steuer, "Defining Virtual Reality: Dimensions Determining Telepresence," *Journal of Communication*, vol. 42, no. 4, pp. 73-93, 1992.
- [3] S. W. Corzine, P. Evans, M. Fisher, J. Gheorma, M. Kato, V. Dominic, P. Samra, A. Nilsson, J. Rahn, I. Lyubomirsky, A. Dentai, P. Studenkov, M. Missey, D. Lambert, A. Spannagel, R. Muthiah, R. Salvatore, S. Murthy, E. Strzelecka, J. L. Pleumeekers, A. Chen, R. Schneider, R. Nagarajan, M. Ziari, J. Stewart, C. H. Joyner, F. Kish and D. F. Welch, "Large-Scale InP Transmitter PICs for PM-DQPSK Fiber Transmission Systems," *IEEE Photonics Technology Letters*, vol. 22, no. 14, pp. 1015-1017, 2010.
- [4] K.-P. Ho, *Phase-modulated optical communication systems*, New York, USA: Springer, 2005.
- [5] F. Koyama and K. Iga, "Frequency chirping in external modulators," *Journal of Lightwave Technology*, vol. 6, no. 1, pp. 87-93, 1988.
- [6] T. Sakamoto, A. Chiba and T. Kawanishi, "50-Gb/s 16 QAM by a quad-parallel Mach-Zehnder modulator," in *Post-Deadline Papers (published 2008), 2007 33rd European Conference and Exhibition of Optical Communication*, Berlin, Germany, 2007.
- [7] C. A. Barrios, V. R. d. Almeida and M. Lipson, "Low-Power-Consumption Short-Length and High-Modulation-Depth Silicon Electrooptic Modulator," *Journal of Lightwave Technology*, vol. 21, no. 4, p. 1089, 2003.
- [8] E. Ip, A. P. T. Lau, D. J. F. Barros and J. M. Kahn, "Coherent detection in optical fiber systems," *Optics Express*, vol. 16, no. 2, pp. 753-791, 2008.
- [9] M. Seimetz, "Laser Linewidth Limitations for Optical Systems with High-Order Modulation Employing Feed Forward Digital Carrier Phase Estimation," in *Optical Fiber Communication Conference*, San Diego, CA, USA, 2008.

- [10] J. Labaziewicz, P. Richerme, K. R. Brown, I. L. Chuang and K. Hayasaka, "Compact, filtered diode laser system for precision spectroscopy," *Optics Letters*, vol. 32, no. 5, pp. 572-574, 2007.
- [11] H. Stoehr, F. Mensing, J. Helmcke and U. Sterr, "Diode laser with 1 Hz linewidth," *Optics Letters*, vol. 31, no. 6, pp. 736-738, 2006.
- [12] A. D. Ludlow, X. Huang, M. Notcutt, T. Zanon-Willette, S. M. Foreman, M. M. Boyd, S. Blatt and J. Ye, "Compact, thermal-noise-limited optical cavity for diode laser stabilization at 1×10^{-15} ," *Optics Letters*, vol. 32, no. 6, pp. 641-643, 2007.
- [13] J. Alnis, A. Matveev, N. Kolachevsky, T. Udem and T. W. Hänsch, "Subhertz linewidth diode lasers by stabilization to vibrationally and thermally compensated ultralow-expansion glass Fabry-Pérot cavities," *Physical Review A*, vol. 77, no. 5, 2008.
- [14] H. S. Margolis, G. P. Barwood, G. Huang, H. A. Klein, S. N. Lea, K. Szymaniec and P. Gill, "Hertz-Level Measurement of the Optical Clock Frequency in a Single 88Sr^+ Ion," *Science*, vol. 306, no. 5700, pp. 1355-1358, 2004.
- [15] Y. Y. Jiang, A. D. Ludlow, N. D. Lemke, R. W. Fox, J. A. Sherman, L. -S. Ma and C. W. Oates, "Making optical atomic clocks more stable with 10-16-level laser stabilization," *Nature Photonics*, vol. 5, pp. 158-161, 2011.
- [16] H. Rong, R. Jones, A. Liu, O. Cohen, D. Hak, A. Fang and M. Paniccia, "A continuous-wave Raman silicon laser," *Nature*, vol. 433, no. 725-728, 2005.
- [17] H. Rong, S. Xu, Y.-H. Kuo, V. Sih, O. Cohen, O. Raday and M. Paniccia, "Low-threshold continuous-wave Raman silicon laser," *Nature Photonics*, vol. 1, pp. 232-237, 2007.
- [18] J. Liu, X. Sun, R. Camacho-Aguilera, L. C. Kimerling and J. Michel, "Ge-on-Si laser operating at room temperature," *Optics Letters*, vol. 35, no. 5, pp. 679-681, 2010.
- [19] J. H. Lee, I. Shubin, J. Yao, J. Bickford, Y. Luo, S. Lin, S. S. Djordjevic, H. D. Thacker, J. E. Cunningham, K. Raj, X. Zheng and A. V. Krishnamoorthy, "High power and widely tunable Si hybrid external-cavity laser for power efficient Si photonics WDM links," *Optics Express*, vol. 22, no. 7, pp. 7678-7685, 2014.

- [20] J.-H. Lee, J. Bovington, I. Shubin, Y. Luo, J. Yao, S. Lin, J. E. Cunningham, K. Raj, A. V. Krishnamoorthy and X. Zheng, "Demonstration of 12.2% wall plug efficiency in uncooled single mode external-cavity tunable Si/III-V hybrid laser," *Optics Express*, vol. 23, no. 9, pp. 12079-12088, 2015.
- [21] S. Keyvaninia, G. Roelkens, D. V. Thourhout, C. Jany, M. Lamponi, A. L. Liepvre, F. Lelarge, D. Make, G.-H. Duan, D. Bordel and J.-M. Fedeli, "Demonstration of a heterogeneously integrated III-V/SOI single wavelength tunable laser," *Optics Express*, vol. 21, no. 3, pp. 3784-3792, 2013.
- [22] N. Tansu and L. J. Mawst, "Current injection efficiency of InGaAsN quantum-well lasers," *Journal of Applied Physics*, vol. 97, no. 054502, 2005.
- [23] A. Yariv, *Quantum Electronics*, 3rd Edition ed., New York: Wiley, 1989.
- [24] L. A. Coldren, S. W. Corzine and M. L. Masanovic, *Diode Lasers and Photonic Integrated Circuits*, 2nd ed., Wiley, 2012.
- [25] C. H. Henry, "Theory of the linewidth of Semiconductor Lasers," *IEEE Journal of Quantum Electronics*, Vols. QE-18, no. 2, pp. 259-264, 1982.
- [26] A. Yariv and P. Yeh, *Photonics: Optical Electronics in Modern Communications*, 6th ed., Oxford, 2007.
- [27] K. Vahala and A. Yariv, "Semiclassical Theory of Noise in Semiconductor Lasers - Part I," *IEEE Journal of Quantum Electronics*, Vols. QE-19, no. 6, p. 1096, 1983.
- [28] K. Vahala and A. Yariv, "Semiclassical Theory of Noise in Semiconductor Lasers - Part II," *IEEE Journal of Quantum Electronics*, Vols. QE-19, no. 6, pp. 1102-1109, 1983.
- [29] K. Petermann, *Laser Diode Modulation and Noise*, Kluwer Academic Publishers, 1988.
- [30] K. Vahala, L. C. Chiu, S. Margalit and A. Yariv, "On the linewidth enhancement factor α in semiconductor injection lasers," *Applied Physics Letters*, vol. 42, no. 8, pp. 631-633, 1983.

- [31] N. K. Dutta, H. Temkin, T. Tanbun-Ek and R. Logan, "Linewidth enhancement factor for InGaAsP/InP strained quantum well lasers," *Applied Physics Letters*, vol. 57, no. 14, pp. 1390-1391, 1990.
- [32] D. Bimberg, N. Kirstaedter, N. N. Ledentsov, Z. I. Alferov, P. S. Kop'ev and V. M. Ustinov, "InGaAs-GaAs Quantum-Dot Lasers," *IEEE Journal of Selected Topics in Quantum Electronics*, vol. 3, no. 2, pp. 196-205, 1997.
- [33] T. C. Newell, T. C. Newell, D. J. Bossert, A. Stintz, B. Fuchs, K. J. Malloy and L. F. Lester, "Gain and Linewidth Enhancement Factor in InAs Quantum-Dot Laser Diodes," *IEEE Photonics Technology Letters*, vol. 11, no. 12, pp. 1527-1529, 1999.
- [34] T. Fujita, J. Ohya, K. Matsuda, M. Ishino, H. Sato and H. Serizawa, "Narrow spectral linewidth characteristics of monolithic integrated-passive-cavity InGaAsP/InP semiconductor lasers," *Electronics Letters*, vol. 21, no. 9, pp. 374-376, 1985.
- [35] I. D. Henning, L. D. Westbrook, A. W. Nelson and P. J. Fiddymment, "Measurements of the linewidth of ridge-guide DFB lasers," *Electronics Letters*, vol. 20, no. 21, pp. 885-887, 1984.
- [36] B.-S. Song, S. Noda, T. Asano and Y. Akahane, "Ultra-high-Q photonic double-heterostructure nanocavity," *Nature Materials*, vol. 4, pp. 207-210, 2005.
- [37] Y. Akahane, T. Asano, B.-S. Song and S. Noda, "Fine-tuned high-Q photonic-crystal nanocavity," *Optics Express*, vol. 13, no. 4, pp. 1202-1214, 2005.
- [38] "Analysis of the experimental Q factors (~ 1 million) of photonic crystal nanocavities," *Optics Express*, vol. 14, no. 5, pp. 1996-2002, 2006.
- [39] H. Sekoguchi, Y. Takahashi, T. Asano and S. Noda, "Photonic crystal nanocavity with a Q-factor of ~ 9 million," *Optics Express*, vol. 22, no. 1, pp. 916-924, 2014.
- [40] J. D. Joannopoulos, S. G. Johnson, J. N. Winn and R. D. Meade, *Photonic Crystals: Molding the Flow of Light*, 2nd Ed. ed., Princeton, NJ, USA: Princeton University Press, 2008.
- [41] E. Yablonovitch and T. J. Gmitter, "Donor and Acceptor Modes in Photonic Band Structure," *Physics Review Letters*, vol. 67, no. 24, pp. 3380-3383, 1991.

- [42] C. T. Santis, High-Coherence Hybrid Si/III-V Semiconductor Lasers, PhD Thesis. California Institute of Technology, 2013.
- [43] S. Tanaka, S.-H. Jeong, S. Sekiguchi, T. Kurahashi, Y. Tanaka and K. Morito, "High-output-power, single-wavelength silicon hybrid laser using precise flip-chip bonding technology," *Optics Express*, vol. 20, no. 27, pp. 28057-28069, 2012.
- [44] M. N. Sysak, D. Liang, R. Jones, G. Kurczveil, M. Piels, M. Fiorentino, R. G. Beausoleil and J. E. Bowers, "Hybrid Silicon Laser Technology: A Thermal Perspective," *IEEE Journal of Selected Topics in Quantum Electronics*, vol. 17, no. 6, pp. 1490-1498, 2011.
- [45] C. Zhang, D. Liang, G. Kurczveil, J. E. Bowers and R. G. Beausoleil, "Thermal Management of Hybrid Silicon Ring Lasers for High Temperature Operation," *IEEE Journal of Selected Topics in Quantum Electronics*, vol. 21, no. 6, 2015.
- [46] W. V. Sorin, K. W. Chang, G. A. Conrad and P. R. Hernday, "Frequency domain analysis of an optical FM discriminator," *Journal of Lightwave Technology*, vol. 10, no. 6, pp. 787-793, 1992.
- [47] N. Satyan, A. Vasilyev, G. Rakuljic, V. Leyva and A. Yariv, "Precise control of broadband frequency chirps using optoelectronic feedback," *Optics Express*, vol. 17, no. 18, pp. 15991-15999, 2009.
- [48] B. Daino, P. Spano, M. Tamburrini and S. Piazzolla, "Phase Noise and Spectral Line Shape in Semiconductor Lasers," *IEEE Journal of Quantum Electronics*, Vols. QE-19, no. 3, p. 266, 1983.
- [49] T. Komljenovic, S. Srinivasan, E. Norberg, M. Davenport, G. Fish and J. E. Bowers, "Widely Tunable Narrow-Linewidth Monolithically Integrated External-Cavity Semiconductor Lasers," *IEEE Journal of Selected Topics in Quantum Electronics*, vol. 21, no. 6, 2015.
- [50] W. Liang, V. S. Ilchenko, D. Eliyahu, A. A. Savchenkov, A. B. Matsko, D. Seidel and L. Maleki, "Ultralow noise miniature external cavity semiconductor laser," *Nature Communications*, vol. 6, no. 7371, 2015.

- [51] D. Kuksenkov, S. Feld, C. Wilmsen, H. Temkin, S. Swirhun and R. Leibenguth, "Linewidth and α -factor in AlGaAs/GaAs vertical cavity surface emitting lasers," *Applied Physics Letters*, vol. 66, no. 3, pp. 277-279, 1995.
- [52] Z. Toffano, A. Destrez, C. Birocheau and L. Hassine, "New linewidth enhancement determination method in semiconductor lasers based on spectral analysis above and below threshold," *Electronics Letters*, vol. 28, no. 1, pp. 9-11, 1992.
- [53] D. Rodríguez, L. Borrueal, I. Esquivas, H. Wenzel, B. Sumpf and G. Erbert, "CW technique for measurement of linewidth enhancement factor: application to 735-nm tensile-strained GaAsP quantum-well laser," *IEEE Photonics Technology Letters*, vol. 16, no. 6, pp. 1432-1434, 2004.
- [54] C. Harder, K. Vahala and A. Yariv, "Measurement of the linewidth enhancement factor α of semiconductor lasers," *Applied Physics Letters*, vol. 42, no. 4, pp. 328-330, 1983.
- [55] K. Kikuchi and T. Okoshi, "Estimation of Linewidth Enhancement Factor of AlGaAs Lasers by Correlation Measurement Between FM and AM Noises," *IEEE Journal of Quantum Electronics*, Vols. QE-21, no. 6, pp. 669-673, 1985.
- [56] G. Liu, X. Jin and S. L. Chuang, "Measurement of Linewidth Enhancement Factor of Semiconductor Lasers Using an Injection-Locking Technique," *IEEE Photonics Technology Letters*, vol. 13, no. 5, pp. 430-432, 2001.
- [57] C. H. Shin, M. Teshima and M. Ohtsu, "Novel measurement method of linewidth enhancement factor in semiconductor lasers by optical self-locking," *Electronics Letters*, vol. 25, no. 1, pp. 27-28, 1989.
- [58] Y. Yu, G. Giuliani and S. Donati, "Measurement of the Linewidth Enhancement Factor of Semiconductor Lasers Based on the Optical Feedback Self-Mixing Effect," *IEEE Photonics Technology Letters*, vol. 16, no. 4, pp. 990-992, 2004.
- [59] Y. Yu, J. Xi and J. F. Chicharo, "Measuring the feedback parameter of a semiconductor laser with external optical feedback," *Optics Express*, vol. 19, no. 10, pp. 9582-9593, 2011.

- [60] Y. Fan, Y. Yu, J. Xi, G. Rajan, Q. Guo and J. Tong, "Simple method for measuring the linewidth enhancement factor of semiconductor lasers," *Applied Optics*, vol. 54, no. 34, pp. 10295-10298, 2015.
- [61] T. Fordell and Å. M. Lindberg, "Experiments on the Linewidth-Enhancement Factor of a Vertical-Cavity Surface-Emitting Laser," *IEEE Journal of Quantum Electronics*, vol. 43, no. 1, pp. 6-15, 2007.
- [62] R. Schimpe, J. E. Bowers and T. L. Koch, "Characterisation of frequency response of 1.5 μm InGaAsP DFB laser diode and InGaAs PIN photodiode by heterodyne measurement technique," *Electronics Letters*, vol. 22, no. 9, pp. 453-454, 1986.
- [63] P. Westbergh, R. Safaisini, E. Haglund, B. Kogel, J. S. Gustavsson, A. Larsson, M. Geen, R. Lawrence and A. Joel, "High-speed 850 nm VCSELs with 28 GHz modulation bandwidth operating error-free up to 44 Gbit/s," *Electronics Letters*, vol. 48, no. 18, pp. 1145-1147, 2012.
- [64] W. Kobayashi, T. Ito, T. Yamanaka, T. Fujisawa, Y. Shibata, T. Kurosaki, M. Kohtoku, T. Tadokoro and H. Sanjoh, "50-Gb/s Direct Modulation of a 1.3- μm InGaAlAs-Based DFB Laser With a Ridge Waveguide Structure," *IEEE Journal of Selected Topics in Quantum Electronics*, vol. 19, no. 4, 2013.
- [65] Y. Matsui, H. Murai, S. Arahira, S. Kutsuzawa and Y. Ogawa, "30-GHz Bandwidth 1.55- μm Strain-Compensated InGaAlAs-InGaAsP MQW Laser," *IEEE Photonics Technology Letters*, vol. 9, no. 1, p. 25, 1997.
- [66] K. Kjebon, O. Kjebon, R. Schatz, S. Lourdudoss, S. Nilsson, B. Stalnacke and L. Backbom, "30 GHz direct modulation bandwidth in detuned loaded InGaAsP DBR lasers at 1.55 μm wavelength," *Electronics Letters*, vol. 3, no. 6, pp. 488-489, 1997.
- [67] O. Kjebon, S. Richard, L. Sebastian, N. Stefan and S. Bjoern, "Modulation response measurements and evaluation of MQW InGaAsP lasers of various designs," *Proceedings of the SPIE*, vol. 2684, pp. 138-152, 1996.
- [68] K. Otsubo, M. Matsuda, K. Takada, S. Okumura, M. Ekawa, H. Tanaka, S. Ide, K. Mori and T. Yamamoto, "1.3- μm AlGaInAs Multiple-Quantum-Well Semi-insulating Buried-Heterostructure Distributed-Feedback Lasers for High-Speed Direct

- Modulation," *IEEE Journal of Selected Topics in Quantum Electronics*, vol. 15, no. 3, pp. 687-693, 2009.
- [69] B. Zhao, T. R. Chen, S. Wu, Y. H. Zhuang, Y. Yamada and A. Yariv, "Direct measurement of linewidth enhancement factors in quantum well lasers of different quantum well barrier heights," *Applied Physics Letters*, vol. 63, no. 14, pp. 1591-1593, 1993.
- [70] T. Komljenovic, S. Srinivasan, E. Norberg, M. Davenport, G. Fish and J. E. Bowers, "Widely Tunable Narrow-Linewidth Monolithically Integrated External-Cavity Semiconductor Lasers," *IEEE Journal of Selected Topics in Quantum Electronics*, vol. 21, no. 6, 2015.
- [71] J. P. V. D. Ziel and R. M. Mikulyak, "Single-Mode Operation 1.3 μm InGaAsP/InP Buried Crescent Lasers Using a Short External Optical Cavity," *IEEE Journal of Quantum Electronics*, Vols. QE-20, no. 3, pp. 223-229, 1984.
- [72] L. A. Coldren and T. L. Koch, "External-Cavity Laser Design," *Journal of Lightwave Technology*, Vols. LT-2, no. 6, p. 1045, 1984.
- [73] L. Chinlon, C. Burrus and L. Coldren, "Characteristics of single-longitudinal-mode selection in short-coupled-cavity (SCC) injection lasers," *Journal of Lightwave Technology*, vol. 2, no. 4, pp. 544-549, 1984.
- [74] R. Wyatt, "Spectral linewidth of external cavity semiconductor lasers with strong, frequency-selective feedback," *Electronics Letters*, vol. 21, no. 15, pp. 658-659, 1985.
- [75] E. Patzak, A. Sugimura, S. Saito, T. Mukai and H. Olesen, "Semiconductor laser linewidth in optical feedback configurations," *Electronics Letters*, vol. 19, no. 24, pp. 1026-1027, 1983.
- [76] K. B. MacAdam, A. Steinbach and C. Wieman, "A narrow-band tunable diode laser system with grating feedback, and a saturated absorption spectrometer for Cs and Rb," *American Journal of Physics*, vol. 60, no. 12, p. 1098, 1992.
- [77] S. Bennetts, G. D. McDonald, K. S. Hardman, J. E. Debs, C. C. Kuhn, J. Close and N. P. Robins, "External cavity diode lasers with 5kHz linewidth and 200nm tuning range

at 1.55 μm and methods for linewidth measurement," *Optics Express*, vol. 22, no. 9, pp. 10642-10654, 2014.

- [78] A. R. Chraplyvy, K. Y. Liou, R. W. Tkach, G. Einstein, Y. K. Jhee, T. L. Koch, P. J. Anthony and U. K. Chakrabarti, "Simple Narrow-Linewidth 1.5 μm InGaAsP DFB External-Cavity Laser," *Electronics Letters*, vol. 22, no. 2, p. 88, 1986.
- [79] K. Petermann, "External Optical Feedback Phenomena in Semiconductor Lasers," *IEEE Journal of Selected Topics in Quantum Electronics*, vol. 1, no. 2, pp. 480-489, 1995.
- [80] R. W. Tkach and A. R. Charaplyvy, "Regimes of Feedback Effects in 1.5-um Distributed Feedback Lasers," *Journal of Lightwave Technology*, Vols. LT-4, no. 11, p. 1655, 1986.
- [81] J. Helms, C. Kurtzke and K. Petermann, "External feedback requirements for coherent optical communication systems," *Journal of Lightwave Technology*, vol. 10, no. 8, pp. 1137-1141, 1992.
- [82] R. W. Tkach and A. R. Chraplyvy, "Linewidth broadening and mode splitting due to weak feedback in single-frequency 1.5 μm lasers," *Electronics Letters*, vol. 21, no. 23, pp. 1081-1083, 1985.
- [83] D. Lenstra, B. H. Verbeek and A. J. Den Boef, "Coherence Collapse in Single-Mode Semiconductor Lasers Due to Optical Feedback," *IEEE Journal of Quantum Electronics*, Vols. QE-21, no. 6, p. 674, 1985.
- [84] J. Helms and K. Petermann, "Microwave modulation of laser diodes with optical feedback," *Journal of Lightwave Technology*, vol. 9, no. 4, pp. 468-476, 1991.
- [85] H. Temkin, N. A. Olsson, J. H. Abeles, R. A. Logan and M. B. Panish, "Reflection noise in index-guided InGaAsP lasers," *IEEE Journal of Quantum Electronics*, Vols. QE-22, no. 2, pp. 286-293, 1986.
- [86] N. Schunk and K. Petermann, "Measured feedback-induced intensity noise for 1.3 μm DFB laser diodes," *Electronics Letters*, vol. 25, no. 1, pp. 63-64, 1989.

- [87] B. R. Clarke, "The effect of reflections on the system performance of intensity modulated laser diodes," *Journal of Lightwave Technology*, vol. 9, no. 6, pp. 741-749, 1991.
- [88] F. Grillot, B. Thedrez, J. Py, O. Gauthier-Lafaye, V. Voiriot and J. L. Lafrayette, "2.5-Gb/s Transmission Characteristics of 1.3- μm DFB Lasers with External Optical Feedback," *IEEE Photonics Technology Letters*, vol. 14, pp. 101-103, 2002.
- [89] J. Helms and K. Petermann, "A Simple Analytic Expression for the Stable Operation Range of Laser Diodes with Optical Feedback," *IEEE Journal of Quantum Electronics*, vol. 26, no. 5, p. 833, 1990.
- [90] D. O'Brien, S. P. Hegarty, G. Huyet, J. G. McInerney, T. Kettler, M. Laemmlin, D. Bimberg, V. M. Ustinov, A. E. Zhukov, S. S. Mikhlin and A. R. Kovsh, "Feedback sensitivity of 1.3 μm InAs/GaAs quantum dot lasers," *Electronics Letters*, vol. 39, no. 24, 2003.
- [91] W. Banqiu, A. Kumar and S. Pamarthy, "High aspect ratio silicon etch: A review," *Journal of Applied Physics*, vol. 108, no. 051101, 2010.
- [92] S. L. Lai, D. Johnson and R. Westerman, "Aspect ratio dependent etching lag reduction in deep silicon etch processes," *Journal of Vacuum Science & Technology A: Vacuum, Surfaces, and Films*, vol. 24, no. 4, pp. 1283-1288, 2006.
- [93] M. D. Henry, ICP Etching of Silicon for Micro and Nanoscale Devices, PhD thesis. California Institute of Technology, 2010.
- [94] "Zeon Chemicals," [Online]. Available: <http://www.zeonchemicals.com/ElectronicMaterials/>.
- [95] H. Namatsu, M. Nagase, T. Yamaguchi, K. Yamazaki and K. Kurihara, "Influence of edge roughness in resist patterns on etched patterns," *Journal of Vacuum Science & Technology B, Nanotechnology and Microelectronics: Materials, Processing, Measurement, and Phenomena*, vol. 16, no. 6, p. 3315, 1998.
- [96] G. Crosnier, D. Sanchez, A. Bazin, P. Monnier, S. Bouchoule, R. Braive, G. Beaudoin, I. Sagnes, R. Raj and F. Raineri, "High Q factor InP photonic crystal

- nanobeam cavities on silicon wire waveguides," *Optics Letters*, vol. 41, no. 3, pp. 579-582, 2016.
- [97] K. R. Williams, K. Gupta and M. Wasilik, "Etch Rates for Micromachining Processing—Part II," *Journal of Microelectromechanical Systems*, vol. 12, no. 6, pp. 761-778, 2003.
- [98] K. K. Lee, D. R. Lim and L. C. Kimerling, "Fabrication of ultralow-loss Si/SiO₂ waveguides by roughness reduction," *Optics Letters*, vol. 26, no. 23, pp. 1888-1890, 2001.
- [99] J.-i. Takahashi, T. Tsuchizawa, T. Watanabe and S.-i. Itabashi, "Oxidation-induced improvement in the sidewall morphology and cross-sectional profile of silicon wire waveguides," *Journal of Vacuum Science & Technology B: Microelectronics and Nanometer Structures*, vol. 22, no. 5, p. 2522, 2004.
- [100] W. Bogaerts, R. Baets, P. Dumon, V. Wiaux, D. Taillaert, B. Luysaert, J. V. Campenhout, P. Bienstman and D. V. Thourhout, "Nanophotonic Waveguides in Silicon-on-Insulator Fabricated With CMOS Technology," *Journal of Lightwave Technology*, vol. 23, no. 1, pp. 401-412, 2005.
- [101] S. T. Steger, A fundamental approach to phase noise reduction in hybrid Si/III-V lasers, PhD Thesis. California Institute of Technology, 2014.
- [102] Y. Vilenchik, Narrow-linewidth Si/III-V lasers: A study of laser dynamics and nonlinear effects, PhD Thesis. California Institute of Technology, 2015.
- [103] D. Pasquariello and K. Hjort, "Plasma-assisted InP-to-Si low temperature wafer bonding," *IEEE Journal of Selected Topics in Quantum Electronics*, vol. 8, no. 1, pp. 118-131, 2002.
- [104] D. Liang and J. E. Bowers, "Highly efficient vertical outgassing channels for low-temperature InP-to-silicon direct wafer bonding on the silicon-on-insulator substrate," *Journal of Vacuum Science & Technology B, Nanotechnology and Microelectronics: Materials, Processing, Measurement, and Phenomena*, vol. 26, no. 4, pp. 1560-1568, 2008.

- [105] D. Liang, A. W. Fang, H. Park, T. E. Reynolds, K. Warner, D. C. Oakley and J. E. Bowers, "Low-Temperature, Strong SiO₂-SiO₂ Covalent Wafer Bonding for III-V Compound Semiconductors-to-Silicon Photonic Integrated Circuits," *Journal of Electronic Materials*, vol. 37, no. 10, pp. 1552-1559, 2008.
- [106] T. Hong, G.-Z. Ran, T. Chen, J.-Q. Pan, W.-X. Chen, Y. Wang, Y.-B. Cheng, S. Liang, L.-J. Zhao, L.-Q. Yin, J.-H. Zhang, W. Wang and G.-G. Qin, "A Selective-Area Metal Bonding InGaAsP-Si Laser," *IEEE Photonics Technology Letters*, vol. 22, no. 15, p. 1141, 2010.
- [107] L. Yuan, H. Yu, W. Chen, D. Lu, Y. Li, G. Ran and J. Pan, "Hybrid InGaAsP-Si Evanescent Laser by Selective-Area Metal-Bonding Method," *IEEE Photonics Technology Letters*, vol. 25, no. 12, pp. 1180-1183, 2013.
- [108] S. Stankovic, R. Jones, M. N. Sysak, J. M. Heck, G. Roelkens and D. V. Thourhout, "1310-nm Hybrid III-V/Si Fabry-Pérot Laser Based on Adhesive Bonding," *IEEE Photonics Technology Letters*, vol. 23, no. 23, pp. 1781-1783, 2011.
- [109] S. Stankovic, R. Jones, M. N. Sysak, J. M. Heck, G. Roelkens and D. V. Thourhout, "Hybrid III-V/Si Distributed-Feedback Laser Based on Adhesive Bonding," *IEEE Photonics Technology Letters*, vol. 24, no. 23, pp. 2155-2158, 2012.
- [110] Y. Cheng, P. D. Dapkus, M. H. MacDougal and G. M. Yang, "Lasing characteristics of high-performance narrow-stripe InGaAs-GaAs quantum-well lasers confined by AlAs native oxide," *IEEE Photonics Technology Letters*, vol. 8, no. 2, pp. 176-178, 1996.
- [111] B. Weigl, M. Grabherr, C. Jung, R. Jager, G. Reiner, R. Michalzik, D. Sowada and K. J. Ebeling, "High-performance oxide-confined GaAs VCSELs," *IEEE Journal of Selected Topics in Quantum Electronics*, vol. 3, no. 2, pp. 409-415, 1997.
- [112] C. Jung, R. Jager, M. Grabherr, P. Schnitzer, R. Michalzik, B. Weigl, S. Muller and K. J. Ebeling, "4.8 mW singlemode oxide confined top-surface emitting vertical-cavity laser diodes," *Electronics Letters*, vol. 33, no. 21, pp. 1790-1791, 1997.
- [113] A. M. Armstrong, M. H. Crawford and D. D. Koleske, "Contribution of deep-level defects to decreasing radiative efficiency of InGaN/GaN quantum wells with increasing emission wavelength," *Applied Physics Express*, vol. 7, no. 032101, 2014.

- [114] M. Iqbal, M. A. Gleeson, B. Spaugh, F. Tybor, W. G. Gunn, M. Hochberg, T. Baehr-Jones, R. C. Bailey and L. C. Gunn, "Label-Free Biosensor Arrays Based on Silicon Ring Resonators and High-Speed Optical Scanning Instrumentation," *IEEE Journal of Selected Topics in Quantum Electronics*, vol. 16, no. 3, pp. 654-661, 2010.
- [115] S. M. Grist, S. A. Schmidt, J. Flueckiger, V. Donzella, W. Shi, S. T. Fard, J. T. Kirk, D. M. Ratner, K. C. Cheung and L. Chrostowski, "Silicon photonic micro-disk resonators for label-free biosensing," *Optics Express*, vol. 21, no. 7, pp. 7994-8006, 2013.
- [116] F. Ghasemi, A. A. Eftekhara, D. S. Gottfried, X. Song, R. D. Cummings and A. Adibi, "Self-referenced silicon nitride array microring biosensor for toxin detection using glycans at visible wavelength," in *Proc. SPIE*, San Francisco, California, USA, 2013.
- [117] F. Vollmer and L. Yang, "Review Label-free detection with high-Q microcavities: a review of biosensing mechanisms for integrated devices," *Nanophotonics*, vol. 1, no. 3-4, pp. 267-291, 2012.
- [118] D. -X. Xu, M. Vachon, A. Densmore, R. Ma, S. Janz, A. Delâge, J. Lapointe, P. Cheben, J. H. Schmid, E. Post, S. Messaoudène and J.-M. Fédéli, "Real-time cancellation of temperature induced resonance shifts in SOI wire waveguide ring resonator label-free biosensor arrays," *Optics Express*, vol. 18, no. 22, pp. 22867-22879, 2010.
- [119] K. B. Gylfason, C. F. Carlborg, A. Kaźmierczak, F. Dortu, H. Sohlström, L. Vivien, C. A. Barrios, W. v. d. Wijngaart and G. Stemme, "On-chip temperature compensation in an integrated slot-waveguide ring resonator refractive index sensor array," *Optics Express*, vol. 18, no. 4, pp. 3226-3237, 2010.
- [120] G. C. Randall and P. S. Doyle, "Permeation-driven flow in poly(dimethylsiloxane) microfluidic devices," *Proc. Natl. Acad. Sci. U.S.A.*, vol. 102, no. 31, pp. 10813-10818, 2005.
- [121] C. E. Soteropulos and H. K. Hunt, "Attaching biological probes to silica optical biosensors using silane coupling agents.," *J. Vis. Exp.*, vol. 63, no. e3866, 2012.

- [122] C. E. Gómez-Sjöberg. [Online]. Available: <https://sites.google.com/site/rafaelsmicrofluidicspage/valve-controllers/usb-based-controller>.
- [123] G. M. Hale and M. R. Querry, "Optical Constants of Water in the 200-nm to 200- μ m Wavelength Region," *Applied Optics*, vol. 12, no. 3, pp. 555-563, 1973.
- [124] D. R. Lide, CRC Handbook of Chemistry and Physics, 88th Edition ed., CRC Press, 2007.
- [125] I. M. White and X. Fan, "On the performance quantification of resonant refractive index sensors," *Optics Express*, vol. 16, no. 2, pp. 1020-1028, 2008.
- [126] S. Donati and R.-H. Horng, "The Diagram of Feedback Regimes Revisited," *IEEE Journal of Selected Topics in Quantum Electronics*, vol. 19, no. 4, 2013.
- [127] QPhotonics, [Online]. Available: <http://www.qphotonics.com/Wavelength-stabilized-single-mode-fiber-coupled-laser-diode-5mW-1550nm.html>.
- [129] N. Schunk and K. Petermann, "Numerical analysis of the feedback regimes for a single-mode semiconductor laser with external feedback," *IEEE Journal of Quantum Electronics*, vol. 24, no. 7, p. 1242, 1988.
- [130] D. Welford and S. Alexander, "Magnitude and phase characteristics of frequency modulation in directly modulated GaAlAs semiconductor diode lasers," *Journal of Lightwave Technology*, vol. 3, no. 5, pp. 1092-1099, 1985.
- [131] F. Favre, "Theoretical analysis of external optical feedback on DFB semiconductor lasers," *IEEE Journal of Quantum Electronics*, Vols. QE-23, no. 1, pp. 81-88, 1987.
- [132] D. O'Brien, S. P. Hegarty, G. Huyet, J. G. McInerney, T. Kettler, M. Laemmlin, D. Bimberg, V. M. Ustinov, A. E. Zhukov, S. S. Mikhlin and A. R. Kovsh, "Feedback sensitivity of 1.3 μ m InAs/GaAs quantum dot lasers," *Electronics Letters*, vol. 39, no. 25, 2003.
- [133] Soitec, [Online]. Available: <https://www.soitec.com/en>.
- [134] Filmetrics, [Online]. Available: <https://www.filmetrics.com/thickness-measurement/f40>.
- [135] CHA Industries, [Online]. Available: http://www.chaindustries.com/mark_40.html.

- [136] K. Iiyama, K.-i. Hayashi and Y. Ida, "Simple method for measuring the linewidth enhancement factor of semiconductor lasers by optical injection locking," *Optics Letters*, vol. 17, no. 16, pp. 1128-1130, 1992.
- [137] J. Geng, C. Spiegelberg and S. Jiang, "Narrow linewidth fiber laser for 100-km optical frequency domain reflectometry," *IEEE Photonics Technology Letters*, vol. 17, no. 9, pp. 1827-1829, 2005.
- [138] H. Ishio, J. Minowa and K. Nosu, "Review and status of wavelength-division-multiplexing technology and its application," *Journal of Lightwave Technology*, vol. 2, no. 4, pp. 448-463, 1984.
- [139] C. A. Brackett, "Dense wavelength division multiplexing networks: principles and applications," *IEEE Journal on Selected Areas in Communications*, vol. 8, no. 6, pp. 948-964, 1990.
- [140] M. I. Hayee and A. E. Willner, "NRZ versus RZ in 10-40-Gb/s dispersion-managed WDM transmission systems," *IEEE Photonics Technology Letters*, vol. 11, no. 8, pp. 991-993, 1999.
- [141] R. Nagarajan, T. Fukushima, S. W. Corzine and J. E. Bowers, "Effects of carrier transport on high-speed quantum well lasers," *Applied Physics Letters*, vol. 59, no. 15, pp. 1835-1837, 1991.
- [142] R. Nagarajan, M. Ishikawa, T. Fukushima, R. S. Geels and J. E. Bowers, "High Speed Quantum-Well Lasers and Carrier Transport Effects," *IEEE Journal of Quantum Electronics*, vol. 28, no. 10, pp. 1990-2008, 1992.
- [143] C. T. Santis, Y. Vilenchik, N. Satyan, G. Rakuljic and A. Yariv, "Purcell-type Control of Quantum Noise in High-Q Semiconductor Laser Resonators," *Submitted*, 2017.